UNIVERSITY
of
GLASGOW

Pull-Out Behaviour of Steel Reinforced Cement Composites

by

Xiaoya Tao

Thesis submitted to the University of Glasgow
in candidature for the Degree of
Doctor of Philosophy

Department of Civil Engineering
The University of Glasgow

March , 2000

Abstract

This thesis is concerned with developing an effective and comprehensive method to simulate pull-out response of fibres in fibre reinforced cement composites. In particular, it addresses cases involving randomly oriented fibre, large relative sliding and interfacial separation between fibre and matrix, and cyclic loading. This work is also extended to study the pull-out behaviour of curved bars in reinforced concrete, because this has many similar features and mechanisms to fibre reinforced concrete. The main strategy and contributions are outlined in the following.

A novel pull-out modelling method is proposed. This consists of a contact algorithm with friction for the interface and damage models for the matrix. It is the first known attempt to merge various pull-out mechanisms of a fibre reinforced cement composite into one two dimensional finite element model. These mechanisms include bonding, debonding, fibre sliding, friction, fibre bending, snubbing, matrix spalling and substantial separation of the fibre at its exit from the matrix. The use of a contact algorithm with friction simplifies the simulation of the interface and only requires an experimental pull-out load-slip relationship from a single perpendicular fibre, having no requirement for additional strength or fracture criteria. Interfacial separations are dealt with by means of different normal constraints on the interface. Matrix spalling is automatically simulated using a concrete damage model.

Accompanying the development of the pull-out model, four increasingly complex concrete damage models and corresponding computational algorithms are developed. These models are a pure damage model (model I), an inelastic-damage model (model II), and reverse cyclic and biaxial loading damage models (model III and model IV). Although the first two models are only suitable for monodirectional cyclic loading, they can describe concrete responses un-

der uniaxial monotonic loading (for both models) and monodirectional cyclic loading (for model II) very well. Models III and IV are based on different damage mechanisms. In the former, the positive and negative parts of the principal strains control the tensile and compressive damage respectively. Since the model is described in strain space, the complexity due to a stress space description in existing models is avoided. In model IV, the introduction of a weighted average damage parameter overcomes the shortcoming of separating stress/strain into positive and negative parts, and greatly simplifies implementation in the finite element method. Additionally, the design of a damage multiplier distinguishes the different contributions of hydrostatic and deviatoric components of the stress/strain tensor to damage and produces the modelling under biaxial loading. The implementation of model IV under biaxial tension and biaxial compression reproduces completely the biaxial experimental results of Kupfer et al.

The validation of the developed models are proved by comparing against experiments. Application are made to fibre reinforced cement composite with single and multiple inclined fibres, and to curved bar reinforced concrete. These studies provide some useful conclusions and point to several recommendations for further researches.

Acknowledgements

I wish to take this opportunity to express formally my sincere gratitude to following people and organisations for their help throughout my study. I truly treasure them all.

My deepest and sincerest thanks go to my principal supervisor Dr. David V. Phillips for his invaluable supervision, endless encouragement, advice, his providing me the opportunity of this study, his recommending me to the CVCP for ORS award and his kindness.

I would like to thank Regius Professor Nenad Bićanić, the Head of the Department, for his valuable guidance and help.

I would also like to thank my second supervisor, the Head of Mechanical Engineering Department, Professor J. W. Hancock for his supervision.

I gratefully acknowledge the financial support of the Committee of Vice-Chancellors and Principals of the Universities of the United Kingdom under the Overseas Research Student Award, and the University of Glasgow under a scholarship.

I am also grateful to my friends and the academic staff for helpful discussions and help, particularly to Dr. B. S. Zhang, Dr. X. W. Gao, Dr. C. J. Pearce and Dr. A. Vatsala.

The help and assistance of the Computer Manager of the Department, Mr. K. McColl, with the computing facilities is greatly appreciated.

Also thanks go to my friends Mr. D. Gallipoli, Dr. K. Babaeyan-Koopaei, Mr. A. Shvidchenko, Mr. L. Cunningham, and Mr. A. Cuthbertson, Ms Z. H. Liao, Mr. K. McGinty and Mr. W. Algaard for their friendship and support.

Finally, my special and heartfelt thanks go to my dear husband Lei for his giving all-out and constant support, genuine understanding, great help and never ending encouragement; to my parents for their understanding and sup-

port; and to my lovely son Xu for giving me a lot of fun. Their understanding and contribution have been the great driving force of my study.

Contents

Notation

In this thesis, each symbol is defined as it is introduced. Some of the more commonly used symbols are described below:

Upper Case Letters

A	Helmholtz free energy
D	damage variable
E	Young's modulus
G	Gibbs free energy
G_0	shear modulus of material
$\mathbf{I}$	2^{nd} or 4^{th} identity tensors
I_1	the first invariant of stress tensor
J_2	the second invariant of deviator stress tensor
$J_2^{'}, J_3^{'}$	deviatoric strain invariants
K	stiffness matrix
K_0	bulk modulus of material
L	element or fibre lengths
P_t	total pull-out load
P_{bd}	pull-out load in bonded zone
P_{dd}	pull-out load in debonded zone
Q	heat energy
U^e, U^p	the elastic and plastic parts of energy respectively
Y	damage energy release rate

Lower Case Letters

$\mathbf{d}$	nodal displacement vector in contact problem
e_{ij}	deviatoric strain components of strain tensor
e_p	principal value of deviatoric strain tensor
f	yield or damage surfaces
g_N	gap, clearance or separation in normal direction of interface
g_T	slip or deformation in tangential direction of interface
l	substantial separation length at fibre exit
$\mathbf{p}$	global displacement vector in contact problem
p	contact pressure
$\mathbf{q}_i$	internal force vector of contact element
s_{ij}	deviator stress tensor
t_N	contact force in normal direction of interface
t_T	contact force in tangential direction of interface

Greek Letters

β	internal variable or damage multiplier
δ	variation of
δ_{ij}	Kronecker delta
$\boldsymbol{\epsilon}$	strain tensor
$\varepsilon_N, \varepsilon_T$	penalty parameters in normal and tangential directions respectively
η	entropy
θ	angle
κ	inelastic material parameter

λ_N, λ_T	Lagrangian multipliers corresponding to normal and tangent directions respectively
$\dot{\lambda}$	damage rate or plastic multipliers
μ	the coefficient of friction
ν	Poisson's ratio
σ	stress
σ_χ	crack closure stress
τ	shear stress
ϕ	fibre diameter
Δ	increment in
Θ	temperature
Ψ	potential energy

Special Sub- or Superscripts

0	of virgin material
c	compression or composite
con	contact
$crit$	critical
e	elasticity
f	fibre
$i, ij, ijkl$	indices in principal, components of stress
in	inelastic
m	mean value or matrix
p	plasticity
pr	predictor
$snub$	snubbing

t	tension
B	trial quantity
N	direction normal to contact surface
T	direction tangential to contact surface
Z	hardening/softening control variable

List of Tables

List of Figures

Chapter 1

Introduction

Cementitious materials, such as mortar and concrete, have an inherent weakness in resisting tensile stress. To overcome this deficiency, fibres can be mixed into them in order to prevent premature cracking and brittle failure. The resulting material is a cost effective engineering material exhibiting improved performance. These materials have a similar features, that is, the matrix deforms by microcracking, and the microcracks are stabilized by the fibres (or reinforcement).

Fibre reinforced concrete (*FRC*) can be classed into four categories based on the fibre material type. There are steel FRC (*SFRC*); glass FRC (*GFRC*); synthetic FRC (*SNFRC*) including carbon fibres; and natural FRC (*NFRC*).

In the last decade or two, FRC has been applied widely in civil engineering. For instance, the most common applications of SFRC are found in industrial floors, tunnel linings and pavements. Polypropylene fibre reinforced concrete (*PPFRC*), a SNFRC, is used to fabricate various types of container from an economical point of view, while polyolefin fibre reinforced concrete is adopted as overlay for roads and bridge decks [2]. Among all the applications, steel fibre reinforced concrete is perhaps the most widely applied FRC material, and has been comprehensively investigated.

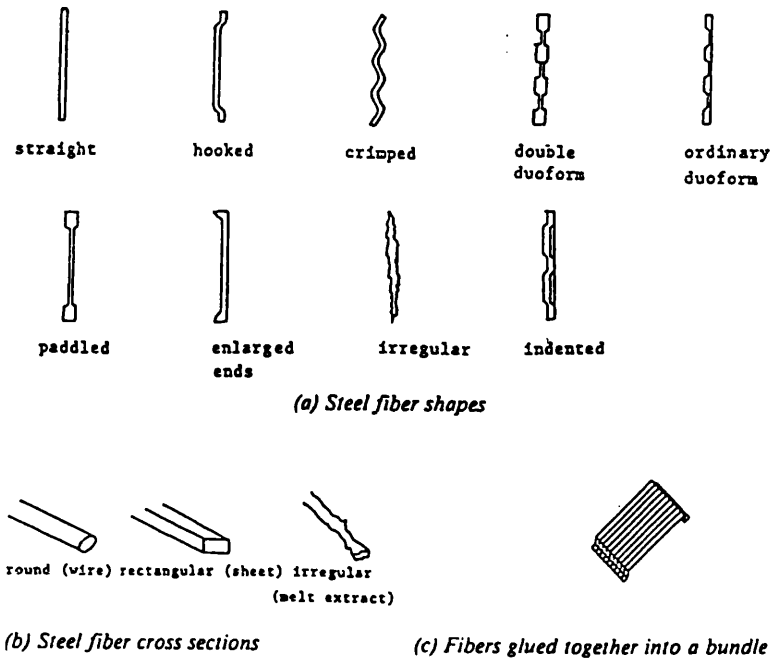

Figure 1.1: Different Steel Fibre Types [1]

Various types of fibre have been developed for SRFC in order to improve workability, and increase ductility and toughness. Their shapes include straight, hooked, crimped, deformed, paddled, enlarged ends, irregular and indented (Fig.1.1 (a)). Different cross sections are used, such as round, rectangular and irregular (Fig.1.1 (b)). A bundle of fibres glued by water-soluble adhesive (Fig. 1.1 (c)) has also been developed to improve workability and eliminate fibre balling during mixing.

Generally, fibres are randomly distributed throughout the entire volume of a matrix, such as concrete, in relatively dilute concentrations.

The characteristics of a composite under tension can be exhibited through three stages: (1) before matrix cracking; (2) multiple cracking; (3) fibre pull-out. The three stages can be schematically interpreted by means of a typical stress-elongation response of high perpormance fibre reinforced cement com-

posite (*HPFRCC*) in Fig.1.2, where "high performance" implies an optimized combination of strength and toughness.

Before matrix cracking, the material behaves elastically. The inclusion of fibre can enhance the pre-cracking behaviour of the composite by increasing its cracking strength. However, the increase in strength, to a great extent, depends on the fibre volume fraction.

For very low fibre volume fraction (< about 0.1%), failure occurs on the first through crack forming. The response of the composite is similar to that of its matrix (see the curve "matrix" in Fig.1.2).

For relatively moderate fibre volume fraction (about 0.1% – 1%), the increase in strength is also indistinct (see the curve "FRC" in Fig.1.2). However, after first cracking, the fibres transfer the load that can no longer be taken by the cracked part of the matrix across the crack through bond between the matrix and the fibres. With the crack opening, the fibres are gradually pulled out of the matrix. In this case, although the addition of fibres does not raise obviously the strength of the composite, it provides improved ductile behaviour. The area under the stress-elongation curve "FRC" is an indication of the ductility or toughness of the composite.

When the fibre volume fraction is large enough (> about 1%), becomes a so-called HPFRCC, and a dramatic change appears (see the curve "HPFRCC" in Fig. 1.2). After the matrix first cracks, fibres will start to carry further load. The slope of the stress-elongation curve will reduce because of the loss of the matrix contribution, and the composite exhibits pseudo strain hardening behaviour. As the load increases further, multiple cracks are formed, and the fibres debond partially until the ultimate tensile strength of the composite is reached. After the peak load, most of the fibres bridging the main crack are debonded and are gradually pulled out from the matrix,

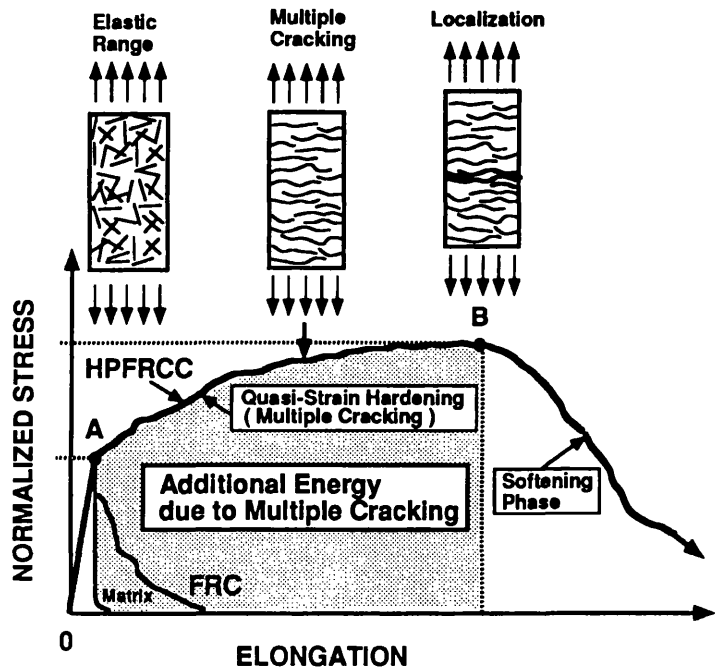

Figure 1.2: Typical Stress-Elongation Response of High Performance Fibre Reinforced Cement Concrete [2].

resulting in a drop of the load-carrying capacity.

The total fracture energy, i.e. the area under the tensile curve, is a measure of the toughness of the composite. The energy is the sum of elastic energy, debonding energy (i.e. the additional energy due to multiple cracking) and pullout energy. Obviously, the strength and toughness of a composite with moderate fibre volume fraction and above are significantly increased.

1.1 Why Pull-Out?

The above description of the failure process of a composite shows that no matter how complex the behaviour of a composite is, crucial to its integrity is the bond between the matrix and fibres/reinforcement. The properties of a FRCC under tension, such as strength and toughness, is dominated by this bond and its breakdown. The fibre's contribution to increasing the toughness of a composite is primarily dictated by its pull-out mechanisms. Its indicator, the relationship of crack bridging force versus crack opening, is a fundamental property that contains information regarding the composite postcracking strength and fracture energy. Hence, the study of pull-out behaviour is an important aspect of research into composite performance.

In summary, the interfacial properties between the matrix and a fibre are of primary importance in understanding the overall behaviour and performance of a composite. Only when the pull-out mechanisms are well understood, can the comprehensive analysis of a composite structure using stochastic or probabilistic methods become feasible.

1.2 A Review of Existing Pull-Out Modelling Methods

Pull-out response involves a great deal of microstructural mechanisms, such as bonding, debonding, friction, sliding, snubbing (a localised friction effect), fibre bending, and local matrix spalling etc. For the composites with randomly distributed fibres and special shape fibres, the mechanisms become even more complicated. Various methods have been developed to study these mechanisms. Existing pull-out modelling approaches can be classified into two categories: analytical methods and numerical methods. A review of these two methods is given in the following sections.

1.2.1 Analytical Methods

In the past decades numerous theoretical models have been postulated, normally based on continuum mechanics and fracture mechanics. In the strength-based models, interfacial stresses control the development of interfacial debonding, while in the fracture-based models, interfacial debonding is governed by energy equilibrium. According to the characteristics of fibre debonding and pull-out processes, two material parameters are usually adopted to describe the interfacial properties of a FRC, namely the interfacial shear strength and frictional stress for a strength-based approach; the critical energy release rate and frictional stress for a fracture-based approach.

Strength-Based Models

The studies using strength-based models focus mainly on understanding the basic mechanisms that control the behaviour of composites, such as predicting the elastic modulus of the composite [15], the bond stress-slip relationship and bond stress distribution [16]~[17], the effect of fibre inclination

angle [18, 19], the effect of fibre rupture [20], the effect of lateral compression history on interface behaviour [21], as well as multiple cracking and pseudo strain hardening processes of HPFRCC [2][22]~[24]. Studying on parameters includes fibre embedded length [20] [25]~[28], critical length of fibre [29], fibre diameter [30], fibre aspect ratio [31], fibre volume fraction [2], fibre modulus [19], matrix properties [19], bond strength [19], fibre inclined angle [18, 19, 26, 32] and snubbing coefficient [31, 33].

In general, the basis of the theoretical models is to establish load equilibrium on an infinitesimal segment of fibre or a single fibre embedded in a half-infinite matrix. Based on the equilibrium relationship, the stress distributions in the reinforcement and matrix, and the shear stress distribution along the interface can be derived for a fully bonded problem.

An essential distinction among early models lies in the assumption of the bond stress distribution along the reinforcement, such as uniform [34], linear [35, 36] and exponential [37].

The development of pull-out experiments permited further understanding of the pull-out mechanisms. Using the experimental observations, and considering whether the maximum shear stress has exceeded the shear strength of interface, partial debonding has been taken into account [3]~[40]. Gopalaratnam and Shah [3] proposed a model which considered the fibre pull-out process in two stages: elastic stress transfer and elastic-frictional stress transfer. The corresponding bond property is shown in Fig. 1.3, where τ_s is the interfacial shear strength and τ_i the frictional shear strength. Two limiting cases exist. When $\tau_s/\tau_i = 1$, the entire debonding process is stable, while for $\tau_s/\tau_i = \infty$, the debonding process is catastrophic immediately after it begins.

Wang et al [41] and Gopalaratnam and Cheng [42] realised that an important feature of bond behaviour was that interfacial bond strength at any

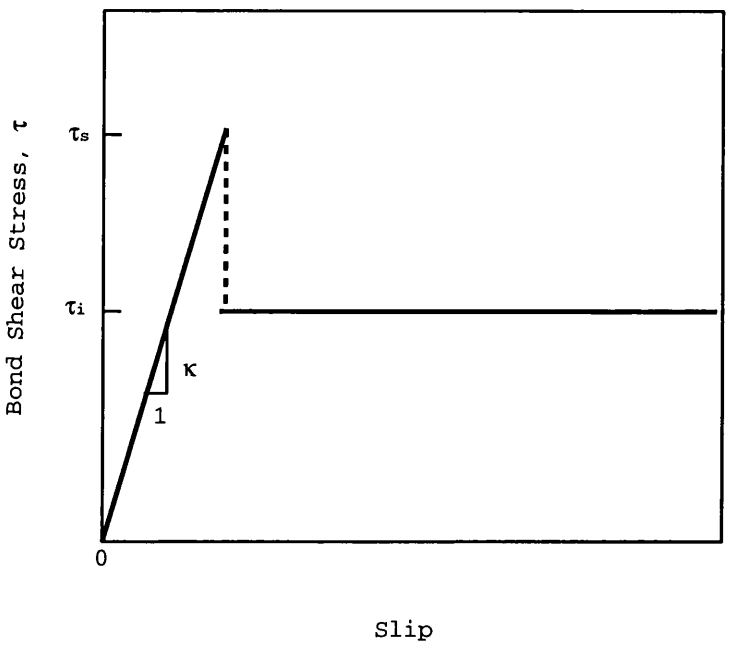

Figure 1.3: Idealized Interface Property Assumed in ref.[3]

point along a fibre is a function of fibre slippage, and this was incorporated into their models. Gopalaratnam and Cheng assumed a local bond stress-slip relationship with linear softening. Although this assumption was not substantiated by any physical evidence, it greatly simplified the implicit governing differential equation of the model. Nammur and Naaman [4] introduced an elastic-frictional bond relationship (see Fig. 1.4). In appearance, it is a special case of [3], when $\tau_s/\tau_i = 1$. However, the essential difference lies in the fact that the former adopted the concept of a local bond stress-slip relationship. Instead of assuming a bond stress-slip curve, Stang et al [43] assumed the matrix as a shear lag with shear stiffness k on a rigid support. The bond stress-slip relation depended on the stiffness of the shear lag.

Full debonding was also considered by Naaman et al. [16, 44]. To simulate the postpeak softening phenomenon in a bond stress-slip curve they simulated the interaction in the normal direction between fibre and matrix

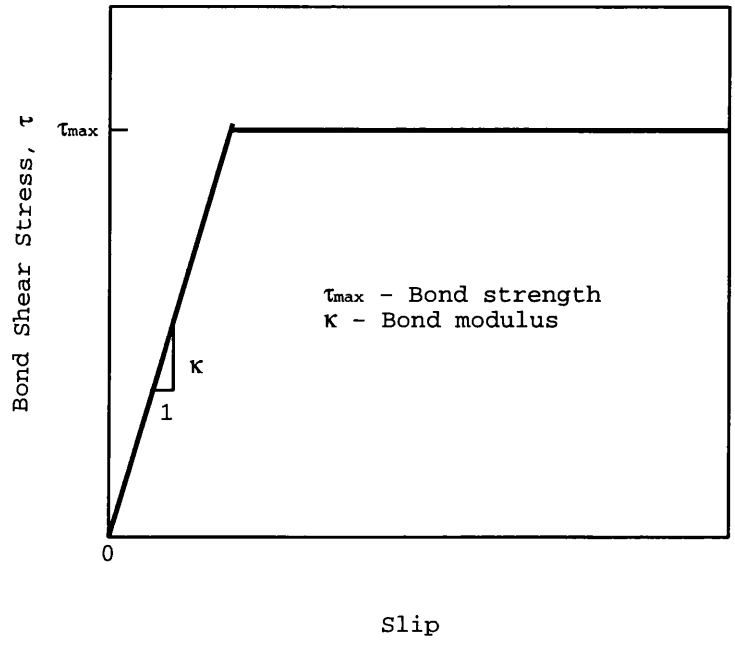

Figure 1.4: Assumed Bond Shear Stress-Slip Relationship in [4]

as two dissimilar components. Due to the effect of Poisson's ratio the contact pressure caused by the misfit will decay as the fibre is loaded longitudinally. To describe the decay the bond stress was assumed to reduce exponentially (Fig. 1.5) . Their model was the first attempt to predict theoretically the entire pull-out process of a smooth straight fibre. Further research on friction decay is found in reference [21].

With the development of pull-out experiments for various FRCC, it was found that the force and energy used to pull a fibre out of matrix increases with the inclined angle of the fibre, but is limited by the strength of cement matrix at high angles due to matrix spalling. A question on the effective use of fibres was raised and promoted the investigation of the pull-out mechanisms of inclined fibres [18]~[20], [45]~[47]. The emphasis was then placed on the analysis of the crack bridging force associated with special mechanisms such as fibre bending, matrix spalling, snubbing and fibre rupture etc.

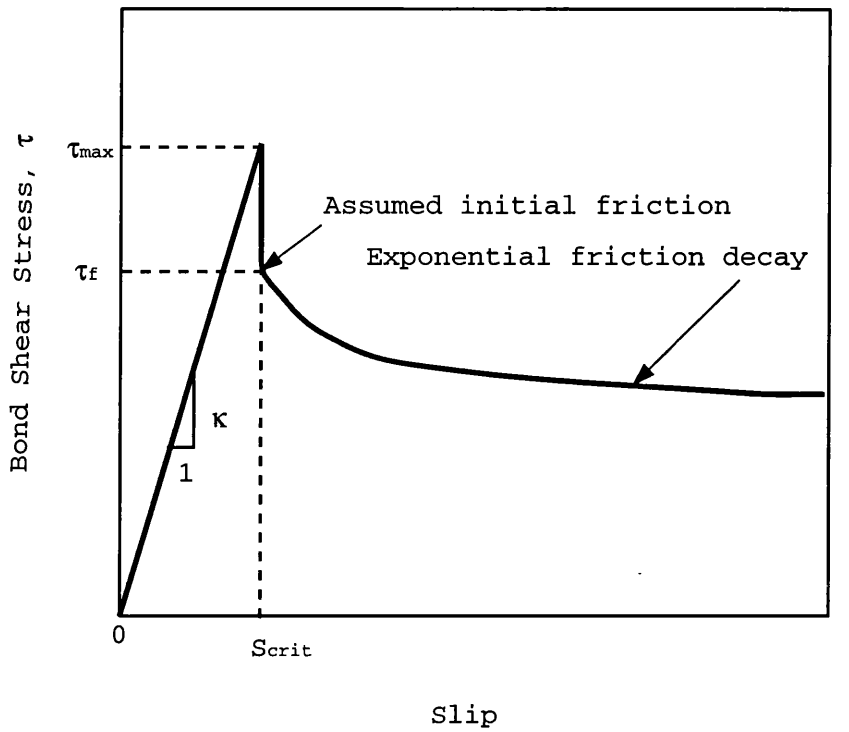

Figure 1.5: Bond Shear Stress-Slip Relationship with Frictional Decay

Fibre bending causes friction concentration (i.e. snubbing) at the fibre exit point from the matrix and increases the pull-out resistance and the tensile stress on the fibre, leading to a more efficient use of the fibre. To describe the effect Li et al [18] suggested a pulley model which simulated the fibre as a flexible rope pulled over a friction pulley. A snubbing coefficient was introduced to consider its effect on the crack bridging force. However, the snubbing model is invalid for stiff and brittle fibres due to their high stiffness and the possible brittle rupture under bending [19, 48].

Another strategy treated an inclined fibre as a cantilever beam on an elastic foundation [19, 49]. Matrix spalling was assumed to occur when the pressure on the matrix exceeds its ultimate compressive strength. The friction concentration was considered in terms of a friction law [19]. When the bridging stress reaches the fibre tensile strength, rupture occurs for those

fibres whose embedded length is longer than a critical embedded length [20].

When pseudo strain-hardening occurred during the pull-out of a HP-FRCC due to multiple cracking, the matrix was assumed to be divided into several segments with similar lengths [50]~[53]. In this case, the matrix was stress-free at the edges of the cracks, and the load was totally carried by the fibres bridging the cracks. Based on the work of Naaman et al [16], a two-fibre equilibrium system was suggested by Kullaa [22]~[24] instead of the original single fibre equilibrium.

Fracture-Based Models

Fracture-based methods [26, 43, 12, 47][54]~[64] have been developed in parallel with strength-based methods. They are based on the concept of energy release rate and treat a debonded zone as an interfacial crack. It is known that the formation of new surface caused by debonding requires energy, whilst, as the crack grows, the structure undergoes elastic recovery, resulting in a decrease in elastic strain energy. Based on the Griffith energy-balance concept, the interfacial crack will propagate when the energy release rate reaches a critical value G_{IC}, an instability condition is reached and crack propagation occurs. Therefore, from the point of view of fracture mechanics, the determination of energy release rate is a basis for the study of debonding and pull-out processes.

Using fracture mechanics, the effect of various parameters on the energy release rate or pull-out load have been studied. These include fibre type [65], fibre length [65], fibre stiffness [66], fibre spacing [66], crack length [43, 12, 62], fibre inclination angles [45, 12], and interface properties [65] etc.

One of the methods of calculating energy release rate is by means of the compliance of a body. Based on this approach, a simple closed-form

equation to predict the ultimate strength of FRC was derived by Stang and Shah [57]. To obtain the total energy release rate of an interfacial crack, a detailed analytical solution of compliance was proposed by Hamoush and Salami[66]. In order to seek a fracture material parameter to characterise the debonding process of an interface Morrison et al [62] studied the influence of relative crack length on the energy release rate. Their results indicated that the energy release rate is a constant value after the ratio of the crack length to the radius of the fibre reaches a certain value.

An alternative approach for calculating the energy release rate is to evaluate energy per unit area crack growth in conjunction with fracture energy criteria [43, 63, 67, 68]. Its application to composites reinforced by hooked and anchored fibres can be found in ref. [68].

To describe a stable debonding process before peak load, a fracture resistance curve (R-curve) was used by Ouyang et al [12]. In their work, a relationship of pull-out load (up to the peak) versus debonding length was derived. To apply this to the case with inclined fibres, an additional strain energy release rate due to fibre bending was taken into account. However, a shortcoming of this model is that the maximum pull-out load in the derived formulation has to be obtained from a special test.

To obtain a closed-form solution for theoretical models, various levels of approximation and assumption have to be made, especially for the matrix and bond behaviour. Generally, it has been assumed that the matrix behaves either stiffly with friction (e.g. a shear lag) or elastically (up to its tensile strength if matrix spalling is considered). The bond between fibre and matrix is assumed to be either uniform friction along the fibre length or a simplified linear function of slippage. The validity of these assumptions have to be assessed by a considerable number of experiments. With the variation of a

large number of parameters and various optimal combinations between them, cost and time can be very high.

An alternative approach is to use a numerical method, such as finite element analysis. This will be discussed in the next section.

1.2.2 Numerical Methods

Finite element analysis has been proved to be a powerful, accurate and effective tool to determine stress distribution, structural response and structural strength, and has been widely used in research and industry. The advantage of the FEA over experiment is that once a FEA model has been validated by several tests, it can easily be used for other similar situations.

The interest of early numerical studies of bond and pull-out was placed in developing special elements, such as bond-link elements with two orthogonal springs [69], contact elements [70], bond-slip elements with finite thickness [71] and one-dimensional bar elements [72] etc. The comparison of some interface elements was given by Keuser and Mehlhorn [73].

Numerical modelling of pull-out for brittle matrix composites reinforced by perpendicular straight fibres/bar is relatively simple and has been studied by several researchers [74]~[78]. For a bar pull-out in reinforced concrete, attention has focused on the simulation of the stress distribution on the interface or in the steel bar. Groot et al [71] modelled the bond stress-slip relation through developing a bond-slip element which was incorporated into the finite element package DIANA. In their model, the concrete was modelled by axisymmetric eight-node elements with elasto-plastic properties in conjunction with a combined criterion, i.e. a Mohr-Coulomb criterion and two tension cut-off criteria. For the steel bar, axisymmetric six-node bond-slip elements were adopted. The slip resistance, mechanical interlocking as

well as bond layer thickness were considered by means of various parameters. Distributions of stress and strain along the steel bar were obtained. In fact, the model can be regarded as a generalisation of the frequently adopted models based on spring elements.

Ezeldin and Balaguru [74] analysed the pull-out mechanism of bar reinforced concrete using the finite element package ANSYS. Instead of regarding the bond between concrete and bar, they assumed the pull-out force varied linearly along the embedded length of the bar and was lumped at specific nodes of the concrete elements. Three-dimensional eight-node isoparametric solid elements were employed for concrete with the properties of linear elasticity in tension and bilinear elasticity in compression. Obviously, this simulation can hardly reflect real bond behaviour and the distribution of interface stresses cannot be attained.

Allwood and Bajarwan [76] used an alternative method which simulated separately the concrete and steel bar. To ensure shear stresses coincided on the corresponding points of the bar and the concrete, a converging iterative process was carried out by means of a formulated bond stress-slip relation, which combined the two solutions together.

Numerical research on steel fibre reinforced brittle-matrix composites, especially that involving randomly distributed fibres, is quite limited. Tsubaki and Sumitro [77] suggested a so-called microstructural unit element which consists of two orthogonal springs installed between two rigid blocks. The matrix, fibre and bond were all simulated with the same elements, but with different stiffness. Debonding was represented by the shear failure of springs. The failure mode of the structure can be directly perceived. However, the pull-out response seems discontinuous and unstable, and far from actual observations.

Perhaps one of the better attempts at modelling a randomly distributed fibre reinforced composite using a numerical method was done by Leung and Li [32] and Leung and Chi [46]. In their work, fibre bending and matrix spalling mechanisms were analysed by treating the fibre as a beam bent on an elastic foundation. The elastic foundation, i.e. the matrix, was modelled through a series of springs with different stiffness along the beam. The spring stiffness was determined using another plane strain model in a plane perpendicular to the fibre in conjunction with the finite element analysis package ADINA. When the matrix material in the vicinity of the fibre reached its failure strain, spalling was assumed to occur and the corresponding springs were moved. The total pull-out response was obtained by coupling the result of the theoretical analysis [53] for debonding with that of the finite element analysis for bending.

Meanwhile, Leung and Chi [46] attempted to simulate all the pull-out mechanisms into one model through the combinations of spring elements, beam elements, plane elements, and contact elements using the finite element package ADINA, but they concluded that with this simulation convergence could not be achieved for most cases.

1.3 Objectives and Significance

Although much progress has been made in the theoretical and numerical aspects of pull-out problem , there are many important issues still to be investigated. In particular, the complex pull-out behaviour of random fibre/curved bar reinforced cement composites requires more investigation. This includes interaction between fibres, special pull-out mechanisms (e.g. bending, spalling, snubbing etc.), the influence of bar curvature and the cyclic response of pull-out. The literature review shows that a practical, effective and comprehensive

FE method is still absent for modelling complex pull-out behaviour. Any such method should be able to embrace as many mechanisms as possible, such as debonding, bending, fibre sliding against matrix, snubbing, matrix spalling and fibre rupture, and to simulate experimental pull-out results well. Despite Leung and Chi's reservations, in my opinion, a comprehensive modelling method is realisable through choosing/developing a proper matrix material model and interface modelling approach.

The main objective of this study is to develop a simple and effective numerical modelling method that is able to predict the comprehensive response of pullout of steel fibre in reinforced cement composites. This, incidentally, could be extended further to the situation of steel bar reinforced concrete, since many of the mechanisms are similar.

Such a powerful interfacial modelling approach should be different from the commonly used method which simulated the interface and its behaviour by means of interface elements and the element stiffness, because this approach has shown many limitations. In order to modelling matrix spalling and cyclic response of pull-out, a concrete damage model also has to be developed, which, at the same time, prepares the ground for the development of interface damage model.

The significance of this work lies in that the model proposed will provide an insight into the various pullout mechanisms, including fibre sliding, friction, bending, spalling and snubbing. It requires only an experimental pull-out load-slip relationship of a single perpendicular fibre, which is easily obtained. The study of the pull-out behaviours of inclined single fibre and multiple fibres will provide information needed for design and further stochastic analysis of a composite. The modelling of curved bars and the response of a straight bar under cyclic load lays a foundation for the application of this

model to deformed bar reinforced concrete in the future.

1.4 Scope of the Thesis

To model fibre pull-out, the modelling of the interface is fundamental. Based on the interface characteristics between steel and concrete, a special interface modelling approach is proposed based on the theory of contact with friction. Chapter 2 introduces and discusses its background and the basis of the theory.

In order to avoid the numerical problems often caused by existing concrete models in commercial finite element packages under large deformation, four damage mechanics models of concrete are developed in this thesis. These models automatically simulate local matrix spalling, avoiding additional spalling criteria required in other models [32, 46]. To provide a good understanding for the developed concrete damage models, Chapter 3 briefly describes basic damage mechanics theory.

Based on La Borderie et al's work [79], a pure damage model and an inelastic-damage model are developed in Chapter 4. The algorithms for the two models are described. The results of implementation and the comparison with experimental results are presented.

In Chapter 5, two new damage mechanics models for concrete subjected to reverse cyclic and biaxial loading are derived based on different damage criteria. One is governed by positive/negative principal stresses and the other distinguishes the different contributions of hydrostatic and deviatoric components of principal stress to damage. The detailed derivations are provided in Appendices A and B. The validity of the models is assessed by application to concrete under uniaxial, biaxial and cyclic loading, and comparison with experimental results and the work of other researchers.

Subsequently, in Chapter 6 a pull-out modelling method is proposed (also

published in ref. [80]), which treats the interface between steel fibre and matrix as a pair of contact surfaces. The interaction between them in normal and tangential directions are specifically considered. A local bond stress-slip relation derived from the experimental result of a perpendicular fibre determines the transmission of shear force on the interface and fibre sliding against the matrix. The influence of local snubbing on the shear force is estimated by a Coulomb friction law. In order to assess proposed method, a sensitivity analysis of various influence factors are conducted, including structural constraints, interface constraints, initial loading increment, mesh sensitivity, debonding length, frictional coefficient and substantial separation length etc.

Chapters 7 to 8 are on the applications of the proposed models to fibre or bar reinforced concrete. Three issues are discussed.

The pull-out responses of single inclined fibre and multiple fibres are investigated in Chapter 7. In the former, numerical analyses are conducted using specimens with initially bent and initially straight fibres respectively. To evaluate further the validity of the proposed modelling technique, the results are compared against experiments. The difference between the different specimens are distinguished. The different contributions of pure pull-out and bending mechanisms are discussed (also see [81]). In the latter, the different fibre layouts and the effect of fibre spacing on pull-out behaviour are analyzed. The interaction between multiple fibres are discussed.

As an extension of the proposed pull-out model, it is applied to curved bar reinforced concrete in Chapter 8. Due to large bar curvature, a large separation between the bar and the matrix is caused by pull-out load. Consequently a different normal constraint to that applied for inclined fibre is employed. The pull-out response of concrete reinforced with curved bar under

monotonic loading is investigated, and the results are compared with experimental data. For cyclic loading of curved bars, a more effective interfacial damage model is required. Since there was insufficient time to attempt this, the pull-out response under cyclic loading has been limited to straight bars only.

Finally, in Chapter 9 the study is summarised, general conclusions are made and suggestions for future work are proposed.

Chapter 2

Basic Theory of Contact with Friction

Various types of contact problem are encountered in structural analysis. The theory on contact has been continuously developed from early work focusing on frictionless contact of linearly elastic bodies under small deformation [82, 83] to large displacement contact problems including friction [84, 85]. Reviews on contact problems are given in refs. [86]~[88]. A detailed introduction and analysis on contact in mechanics and its mathematical aspects can be found in refs. [89, 90].

In finite element analysis of contact problems, interface elements are inserted between two interactive surfaces. Node-to-node contact (such as gap elements), node-on-segment and node-on-surface contact (such as line/surface slide elements etc.) are widely adopted. The last two are used in situations with large deformation. A contactor and a target are defined in a contact pair. Usually the penetration of points on the contactor into the target is limited. When penetration occurs, constraints force the penetrating contactor point to return to the boundary surface of the target element. With different constraints, different contact conditions (frictionless, sticking, sliding, as well as their combination) are realised.

The implementation of the contact and sliding conditions can be considered as a problem of constrained minimisation. The penalty approaches [91]~ [96], Lagrangian multipliers [90, 91][97]~[99] as well as the augmented Lagrangian technique [93][100]~[103], a combined Lagrangian multiplier/penalty function method, are widely used to solve the problem. The contact forces are computed so as to ensure the penetrated points remain on contact interface.

Based on this simple description of the contact problem, some corresponding issues will be discussed in this chapter. As a starting point, the contact monitoring and constraint conditions are first outlined in sections 2.1 and 2.2. Section 2.3 focuses on the implementation of constraint conditions. Finally, contact forces are given.

2.1 Detection of Penetration

When contact happens between a contactor and a target, four contact states for the contact points can be defined, i.e. separating, sticking, sliding and penetrating. Penetration of points on a contactor surface into the target must be prevented. Penetrating points must be found and then returned, and contact forces modified. Two methods have been proposed to search for the penetrating points. One is the triangle area approach used by Guerra and Browning [104], see Fig. 2.1 in which 1 and 2 are two points of a segment on a target and s is a point on a contactor. Clearly penetration occurs if points $(s, 1, 2)$ are found to be anticlockwise, and no penetration if $(s, 1, 2)$ are found to be clockwise. When the penetrating point is found, point s is required to be returned to the closest point on the segment along the direction of normal vector $\mathbf{N}$.

The other contact monitoring method, named the element method, was

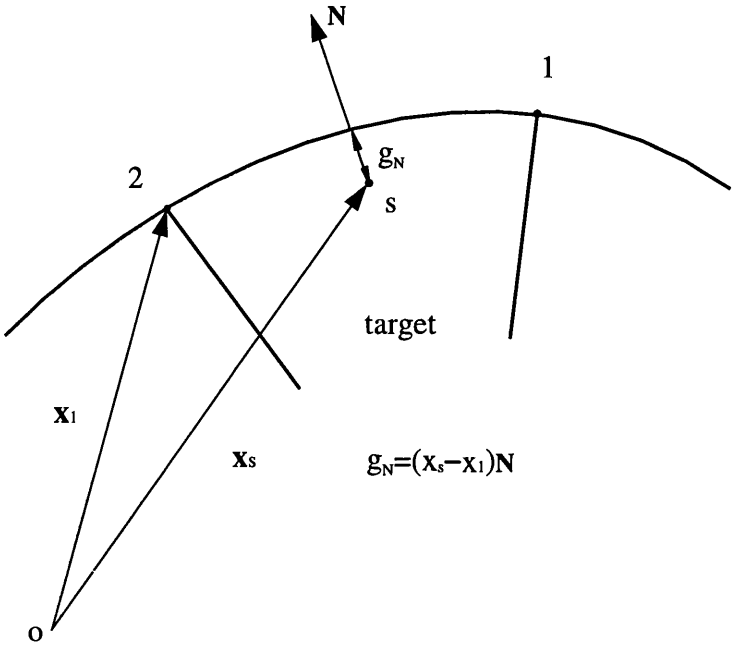

Figure 2.1: Triangle Area Method

described by Mottershead, Pascoe and English [90] (Fig. 2.2). When a contactor point, s_i, lies within the domain of a target element at the ith iteration, its location within the target can be defined by

$$-1 < \xi_s, \eta_s < 1 \tag{2.1}$$

where ξ_s, η_s are the local co-ordinate of s_i on a target surface element. The returned vector $\mathbf{g}$ is linearly determined by the intersection h_i of the element surface with the path of s point at successive iterations $i-1$ and i. At the next iteration h_{i+1} and s_{i+1} are constrained so that they coincide. It should be noted that the direction of $\mathbf{g}$ is generally dissimilar to that of $\mathbf{N}$.

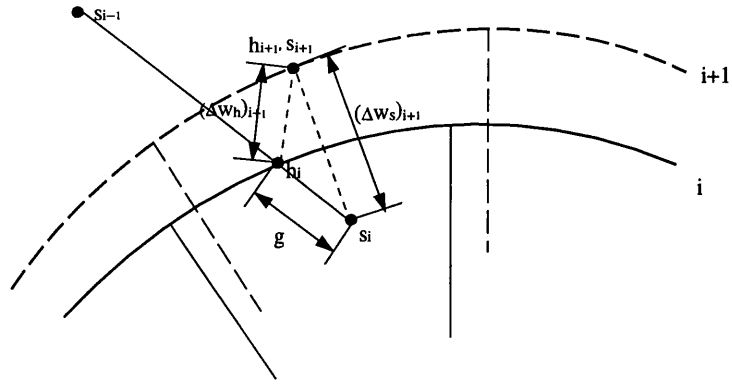

Figure 2.2: Element Method

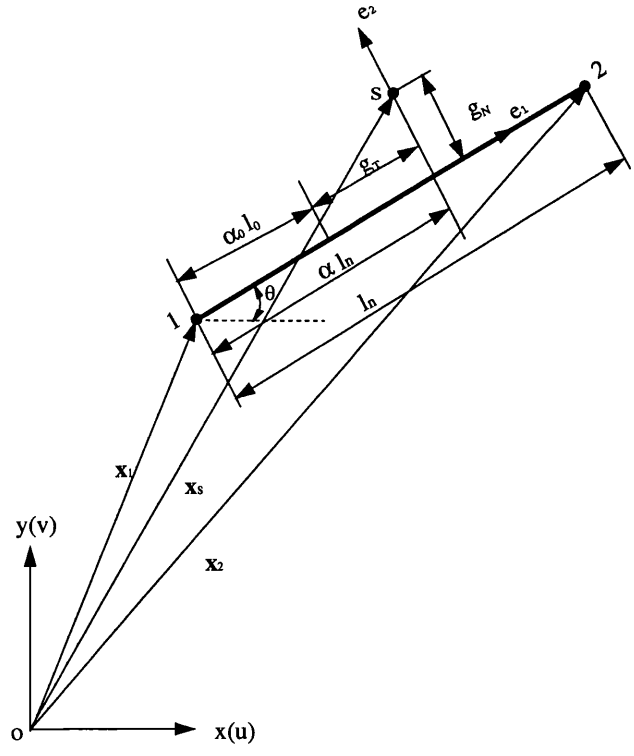

Figure 2.3: Two-Dimensional Contact Element

2.2 Constraint Conditions

When contact occurs, suppose a contact element involves a target segment (with nodes 1 and 2) and a contactor node (node s) as shown in Fig. 2.3. $\mathbf{e}_1$ and $\mathbf{e}_2$ are unit vectors, lying in the tangential direction and in the normal direction of the contact element, respectively, so that:

$$\mathbf{e}_1 = (\cos\theta, \sin\theta); \qquad \mathbf{e}_2 = (-\sin\theta, \cos\theta). \tag{2.2}$$

l_0 and l_n in Fig. 2.3 are the initial and current lengths between node 1 and 2. The normal gap is defined as g_N and the tangential slip as g_T, and they are expressed as

$$\mathbf{g}_N = (\mathbf{X}_s - \mathbf{X}_1)^T \mathbf{e}_2 = \mathbf{X}_{s1}^T \mathbf{e}_2 \tag{2.3}$$

$$\mathbf{g}_T = \alpha l_0 - \alpha_0 l_0 = \frac{l_0}{l_n} \mathbf{X}_{s1}^T \mathbf{e}_1 - \alpha_0 l_0 \tag{2.4}$$

with

$$\alpha = \frac{1}{l_n} \mathbf{X}_{s1}^T \mathbf{e}_1 \tag{2.5}$$

and where α can be interpreted as the non-dimensional tangential distance between node 1 and the projection of the contact node s on to e_1, while α_0 is the value of α when the current phase of contact was first activated. Note that replacing l_n with l_0 in the first term of the middle part of Eq. 2.4 is to avoid the non-symmetry in the resulting tangent stiffness matrix [89]. To derive contact forces through a virtual work approach in the following description, the relationships between the changes in the local variables (here g_N, g_T) and the changes in global variables are required. The global variables of the displacement are written as

$$\mathbf{p}^T = (\mathbf{d}_s^T, \mathbf{d}_1^T, \mathbf{d}_2^T) \tag{2.6}$$

where the subscripts denote the nodes. Then the changes in the local variables can be given by the global variables

$$\begin{aligned} \delta g_N &= \delta \mathbf{d}_{s1}^T \mathbf{e}_2 + \mathbf{X}_{s1}^T \delta \mathbf{e}_2 \\ &= \mathbf{a}^T \delta \mathbf{p} \end{aligned} \tag{2.7}$$

$$\begin{aligned} \delta g_T &= \frac{l_0}{l_n}(\mathbf{e}_1^T \delta \mathbf{d}_{s1} - \alpha \mathbf{e}_1^T \delta \mathbf{d}_{21}) + \frac{l_0}{l_n}\mathbf{X}_{s1}^T \delta \mathbf{e}_1 \\ &= \frac{l_0}{l_n}\mathbf{c}^T \delta \mathbf{p} - g_N \frac{l_0}{l_n^2}\mathbf{b}^T \delta \mathbf{p} \\ &= \mathbf{f}^T \delta \mathbf{p} \end{aligned} \tag{2.8}$$

with

$$\mathbf{a}^T = (\mathbf{e}_2^T, -(1-\alpha)\mathbf{e}_2^T, -\alpha \mathbf{e}_2^T) \tag{2.9}$$

$$\mathbf{b}^T = (\mathbf{0}^T, \mathbf{e}_2^T, -\mathbf{e}_2^T) \tag{2.10}$$

$$\mathbf{c}^T = (\mathbf{e}_1^T, -(1-\alpha)\mathbf{e}_1^T, -\alpha \mathbf{e}_1^T) \tag{2.11}$$

Using virtual work, the contribution to the internal force vector $\mathbf{q}$ for the contact element is

$$\mathbf{q} = t_N \mathbf{a} + t_T \mathbf{f} = \begin{pmatrix} \mathbf{f}^T \\ \mathbf{a}^T \end{pmatrix} \begin{pmatrix} t_T \\ t_N \end{pmatrix} = \bar{\mathbf{B}}^T \mathbf{t} \tag{2.12}$$

where t_N and t_T are the contact forces in the normal and tangential directions respectively. Thus contact states can be defined by using so-called Kuhn-Tucker conditions as follows:

for normal and sticking contact:

$$(g_T, g_N)^T \geq 0$$
$$(t_T, t_N)^T \leq 0$$
$$(g_T, g_N)^T (t_T, t_N) = 0 \tag{2.13}$$

for sliding contact:

$$f = |t_T| + \mu t_N = \omega t_T + \mu t_N \leq 0$$
$$\dot{g}_p = (\dot{g}_T, \dot{g}_N)_p^T \geq 0$$
$$f \dot{g}_p = 0 \tag{2.14}$$

where f is a yield function, i.e. the limitation of sticking frictional capacity for the tangential component of the contact force, and $\dot{g}_p$ is the absolute value of the relative sliding velocity between the contacting nodes. μ is the coefficient of friction and $\omega = t_T/|t_T| = \pm 1$.

2.3 Implementation of Constraints

A variety of techniques may be applied for the implementation of the contact and sliding conditions, but the most common ones are the penalty function method, Lagrangian multipliers approach and a combination of both, the augmented Lagrangian technique.

2.3.1 Penalty Function Method

In a conventional penalty approach, the contact forces are defined for sticking friction by

$$t_N = \varepsilon_N g_N \tag{2.15}$$

$$t_T = \varepsilon_T g_T \tag{2.16}$$

where ε_N and ε_T can be interpreted as the penalty parameter or as the elastic stiffness of the contact element in normal and tangential directions respectively.

From the variation of Eq. 2.12 in conjunction with Eqs. 2.7 and 2.8, their contribution to the tangent stiffness can be obtained. The variation is given by

$$\begin{aligned} \delta\mathbf{q} &= \mathbf{K}\delta\mathbf{p} \\ &= \delta t_N \mathbf{a} + t_N \delta\mathbf{a} + \delta t_T \mathbf{f} + t_T \delta\mathbf{f} \\ &= (\varepsilon_N \mathbf{a}\mathbf{a}^T + \varepsilon_T \mathbf{f}\mathbf{f}^T)\delta\mathbf{p} + \mathbf{K}_\sigma(t_N)\delta\mathbf{p} + \mathbf{K}_\sigma(t_T)\delta\mathbf{p} \end{aligned} \tag{2.17}$$

in which the matrix $\mathbf{K}$ is a combined tangent stiffness, the first bracketed term is the conventional linear rank-one contact stiffness, and $\mathbf{K}_\sigma(t_N)$ and $\mathbf{K}_\sigma(t_T)$ can be interpreted as the initial stress matrices for the contact element corresponding to the normal and tangential directions, respectively. These can be derived via $\delta\mathbf{a}$ and $\delta\mathbf{f}$ (a detailed derivation can be found in ref. [89]) as

$$\mathbf{K}_\sigma(t_N) = \frac{t_N}{l_n}[\mathbf{b}\mathbf{c}^T + \mathbf{c}\mathbf{b}^T - \frac{g_N}{l_n}\mathbf{b}\mathbf{b}^T] \tag{2.18}$$

$$\mathbf{K}_\sigma(t_T) = t_T\Big[\frac{l_0}{l_n}(-\mathbf{a}\mathbf{b}^T - \mathbf{b}\mathbf{a}^T + \mathbf{b}_1\mathbf{c}^T + \mathbf{c}\mathbf{b}_1^T) - 2g_N\frac{l_0}{l_n^3}(\mathbf{b}\mathbf{b}_1^T + \mathbf{b}_1\mathbf{b}^T)\Big] \tag{2.19}$$

with

$$\mathbf{b}_1^T = (\mathbf{0}^T, \mathbf{e}_1^T, -\mathbf{e}_1^T) \tag{2.20}$$

Finally, the combined tangent stiffness matrix is given by

$$\begin{aligned} \mathbf{K} &= \bar{\mathbf{B}}^{\mathbf{T}}\mathbf{C}\bar{\mathbf{B}} + \mathbf{K}_\sigma(t_T) + \mathbf{K}_\sigma(t_N) \\ &= \bar{\mathbf{B}}^{\mathbf{T}} \begin{bmatrix} \varepsilon_T & 0 \\ 0 & \varepsilon_N \end{bmatrix} \bar{\mathbf{B}} + \mathbf{K}_\sigma(t_T) + \mathbf{K}_\sigma(t_N) \end{aligned} \tag{2.21}$$

Thus a symmetric initial stiffness matrix is formed.

When sliding appears, sliding friction is taken into account with the aid of a 'plasticity algorithm' so that the yield function is written as

$$f = \begin{pmatrix} \omega \\ \mu \end{pmatrix}^T \begin{pmatrix} t_T \\ t_N \end{pmatrix} = \bar{\mathbf{a}}^T \mathbf{t} = 0 \tag{2.22}$$

where ω has previously been defined in section 2.2, μ is the coefficient of friction, and t_T now has a different form from Eq.2.16, i.e.

$$t_T = t_{TA} + \varepsilon_T(\Delta g_T - \Delta\eta\,\omega) \tag{2.23}$$

where the term t_{TA} is the value of t_T at the end of the last increment, Δg_T is the incremental tangential gap from the end of last increment to the current iteration, while the $\Delta\eta\omega$ is 'plastic tangential slip' related to a non-associative plasticity law. The non-associative flow rule is written as

$$\dot{\mathbf{g}}_p = \begin{pmatrix} \dot{g}_T \\ \dot{g}_N \end{pmatrix}_p = \dot{\eta} \begin{pmatrix} \frac{\partial f}{\partial t_T} \\ 0 \end{pmatrix} = \dot{\eta} \begin{pmatrix} \omega \\ 0 \end{pmatrix} = \dot{\eta}\bar{\mathbf{b}} \tag{2.24}$$

Adopting a backward-Euler return mapping technique used in plasticity, the contact forces in Eqs. 2.15 and 2.23 can be written using those computed at the elastic trial point, B, as

$$\mathbf{t} = \mathbf{t}_B - \Delta\eta\mathbf{C} \begin{pmatrix} \omega_B \\ 0 \end{pmatrix} = \mathbf{t}_B - \Delta\eta\mathbf{C}\bar{\mathbf{b}}_B \tag{2.25}$$

where $\mathbf{C}$ has been defined in Eq. 2.21. Substitution of Eq. 2.25 into the yield function of Eq. 2.22 leads to

$$\Delta\eta = \frac{(\omega_B t_{TB} + \mu t_{NB})}{\varepsilon_T} = \frac{f_B}{\varepsilon_T} \tag{2.26}$$

where f_B is the value of yield function computed at the trial point, B. So far, the tangent contact force t_T in Eq. 2.23 along with Eq. 2.26 can be completely determined.

In a conventional return mapping procedure the elastic trial force t_B is first computed and then checked if yield function $f_B \geq 0$. If not, the contact still belongs to a sticking friction contact and the final forces are set to t_B. However, if $f_B \geq 0$, sliding friction contact occurs. The 'returned forces' from Eq. 2.25 can be obtained in conjunction with Eq. 2.26.

In order to obtain the tangent stiffness, Eq. 2.12 is differentiated again

$$\begin{aligned} \delta\mathbf{q} &= \bar{\mathbf{B}}^T \delta\mathbf{t} + \delta\bar{\mathbf{B}}^{\mathbf{T}}\mathbf{t} \\ &= [\bar{\mathbf{B}}^{\mathbf{T}}\bar{\mathbf{C}}\bar{\mathbf{B}} + \mathbf{K}_\sigma(t_T) + \mathbf{K}_\sigma(t_N)]\delta\mathbf{p} \end{aligned} \tag{2.27}$$

where $\mathbf{K}_\sigma(t_T)$ and $\mathbf{K}_\sigma(t_N)$ have been defined in Eqs. (2.18) and (2.19) respectively. $\bar{\mathbf{C}}$ can be obtained through the differentiation of Eq. 2.25,

$$\begin{aligned} \dot{\mathbf{t}} &= \mathbf{C}\dot{\mathbf{g}} - \dot{\eta}\mathbf{C}\bar{\mathbf{b}}_B \\ &= \bar{\mathbf{C}}\,\dot{\mathbf{g}} \\ &= \varepsilon_N \begin{bmatrix} 0 & -\mu\omega \\ 0 & 1 \end{bmatrix} \dot{\mathbf{g}} \end{aligned} \tag{2.28}$$

Thus the combined stiffness matrix is completely determined as follows

$$\mathbf{K} = \bar{\mathbf{B}}^T \varepsilon_N \begin{bmatrix} 0 & -\mu\omega \\ 0 & 1 \end{bmatrix} \bar{\mathbf{B}} + \mathbf{K}_\sigma(t_T) + \mathbf{K}_\sigma(t_N) \tag{2.29}$$

Comparing Eqs. 2.21 and 2.29 it is found that to change from sticking to sliding, only C is changed to $\bar{C}$. However, a non-symmetric initial stiffness matrix is then introduced.

The advantage of the penalty method is that the technique is simple and no additional equations are introduced. Interpreted from a physical standpoint, the penalty parameters can be considered as the stiffness of a stiff spring inserted between the contacting points, and no other variables and manipulation are required. However, this method will not apply the constraints strictly unless a high penalty number is used and in that case the method is prone to instability and suffers from ill-conditioning that worsens as the penalty values are increased. [105, 100].

2.3.2 Lagrangian Multipliers Method

The Lagrangian multipliers approach is a classical optimisation approach. It uses Lagrangian multipliers to incorporate the equality or inequality constraints with the objective function, so that a constrained non-linear optimisation problem can be converted to an unconstrained problem.

Lagrangian multipliers were first used in contact analysis by Hughes et al [83] to solve elastic contact and elastic impact problems. Using this approach the contact problem is defined by the potential function.

$$\Pi = \psi + (\sum \lambda_N g_N + \sum \lambda_T g_T) \tag{2.30}$$

where ψ is the total potential energy, and λ_N and λ_T are a set of Lagrangian multipliers, corresponding to normal and tangent directions respectively, re-

lating to each of the contact elements . They may be interpreted as contributions to the contact forces and be treated as additional variables in the problem.

By minimising with respect to $\delta\mathbf{p}$ and $\delta\lambda$ and satisfying the first-order conditions, for the sticking friction over an 'active set', a, Eq. 2.30 becomes

$$\begin{aligned} \delta\Pi &= \bar{\mathbf{F}}^T\delta\mathbf{p} + \sum_a \lambda_N \delta g_N(\delta\mathbf{p}) + \sum_a \lambda_T \delta g_T(\delta\mathbf{p}) \\ &= \bar{\mathbf{F}}^T\delta\mathbf{p} + \mathbf{q}^T\delta\mathbf{p} \\ &= 0 \end{aligned} \tag{2.31}$$

with

$$\mathbf{g} = \begin{pmatrix} g_T \\ g_N \end{pmatrix} = 0 \qquad \text{over a} \tag{2.32}$$

and the Kuhn-Tucker conditions

$$\boxed{\begin{array}{c} g_N \geq 0 \\ \lambda_N \leq 0 \\ g_N\lambda_N = 0 \end{array}} \tag{2.33}$$

where $\bar{\mathbf{F}}$ contains the gradient of the total potential energy for 'non-contact elements'. The internal force vector $\mathbf{q}$ can be derived for a single contact element in the same manner as in section 2.2. Thus,

$$\mathbf{q} = \bar{\mathbf{B}}^T\lambda = \begin{pmatrix} \mathbf{f}^T \\ \mathbf{a}^T \end{pmatrix} \begin{pmatrix} \lambda_T \\ \lambda_N \end{pmatrix} \tag{2.34}$$

with the contact constraints of Eq. 2.32. Applying respectively a Taylor series expansion for the equilibrium equation of Eq. 2.34 and the constraints of Eq. 2.32, a Newton-Raphson iteration of the form below is obtained

$$\begin{pmatrix} \delta p_{i+1} \\ \delta \lambda_{i+1} \end{pmatrix} = - \begin{bmatrix} \mathbf{K}_i & \bar{\mathbf{B}}_i^T \\ \bar{\mathbf{B}}_i & 0 \end{bmatrix}^{-1} \begin{pmatrix} \bar{F}_i \\ g_i \end{pmatrix} \tag{2.35}$$

where

$$\mathbf{K} = \bar{\mathbf{K}} + \mathbf{K}_\sigma(\lambda_T) + \mathbf{K}_\sigma(\lambda_N) \tag{2.36}$$

in which $\bar{\mathbf{K}}$ has the tangent stiffness matrix from the non-contact elements.

The benefit of the Lagrangian multipliers method is its accuracy since constraints are exactly imposed. Its drawback is the appearance of additional variables — the Lagrangian multipliers, and special care must be taken with the ordering of the equations during the solution process [89]. An augmented Lagrangian technique as a new treatment has been developed, which can be viewed as a combined Lagrangian multipliers/penalty function method. It provides important advantages over the more traditional Lagrangian multipliers and penalty methods. The method will be briefly discussed in the next section.

2.3.3 Augmented Lagrangian Technique

The augmented Lagrangian method was originally proposed by Hestenes[106] and Powell[107] for coping with mathematical programming problems subjected to equality constraints. It can be regarded as an extension or combination of the two methods described previously.

For the augmented Lagrangian method, Eq. 2.30 is employed and appended with a penalty term, which results in

$$\Pi + \sum_a \frac{1}{2} \mathbf{g}^T \mathbf{C} \mathbf{g} = \psi_b + \sum_a \mathbf{g}^T \lambda + \sum_a \frac{1}{2} \mathbf{g}^T \mathbf{C} \mathbf{g} \tag{2.37}$$

Following the same approach as was done for the Lagrangian multipliers method, the equilibrium and constraint equations are expressed as follows

$$\begin{aligned} \mathbf{F} &= \bar{\mathbf{F}} + \mathbf{q} \\ &= \bar{\mathbf{F}} + \bar{\mathbf{B}}^T(\mathbf{C}\mathbf{g} + \lambda) \\ &= 0 \end{aligned} \tag{2.38}$$

$$\mathbf{g} = \begin{pmatrix} g_T \\ g_N \end{pmatrix}^T = 0 \tag{2.39}$$

where

$$\mathbf{q} = \begin{pmatrix} \mathbf{f}^T \\ \mathbf{a}^T \end{pmatrix} \begin{pmatrix} \lambda_T + \varepsilon_T g_T \\ \lambda_N + \varepsilon_N g_N \end{pmatrix} = \bar{\mathbf{B}}^T \begin{pmatrix} t_T \\ t_N \end{pmatrix} = \bar{\mathbf{B}}^T \mathbf{t} \tag{2.40}$$

If the contact is accompanied with Coulomb 'sliding friction', the internal force vector for the contact element is modified to

$$\mathbf{q} = \begin{pmatrix} \mathbf{f}^T \\ \mathbf{a}^T \end{pmatrix} \begin{pmatrix} \lambda_T + \varepsilon_T(\Delta g_T - \Delta\eta\omega_H) \\ \lambda_N + \varepsilon_N g_N \end{pmatrix} = \bar{\mathbf{B}}^T \begin{pmatrix} t_T \\ t_N \end{pmatrix} = \bar{\mathbf{B}}^T \mathbf{t} \tag{2.41}$$

where $\mathbf{f}$, $\mathbf{a}$, and scalar $\Delta\eta$ all have been defined in Eqs. 2.8, 2.9 and 2.26, respectively, and $\Delta\eta$ must satisfy the yield function Eq. 2.22. Using a Taylor series expansion as it was done for Eq.2.35 leads to

$$\begin{pmatrix} \delta p_{i+1} \\ \delta\lambda_{i+1} \end{pmatrix} = - \begin{bmatrix} \mathbf{K}_i & \bar{\mathbf{B}}_i^T \\ \bar{\mathbf{B}}_i & 0 \end{bmatrix}^{-1} \begin{pmatrix} F_i \\ g_i \end{pmatrix} \tag{2.42}$$

Thus has the same form as Eq. 2.35, but the tangential stiffness matrix contribution from the contact element is now

$$\begin{aligned} \mathbf{K} &= \bar{\mathbf{B}}^T \bar{\mathbf{C}}_T \bar{\mathbf{B}} + \mathbf{K}_\sigma(\lambda_T + \varepsilon_T(\Delta g_T - \Delta\eta\omega_H)) \\ &+ \mathbf{K}_\sigma(\lambda_N + \varepsilon_N g_N) \end{aligned} \tag{2.43}$$

The augmented Lagrangian approach has its advantages: no 'solution ordering' problem in the Lagrangian multipliers method since $\mathbf{K}$ on its own is now non-singular, no large penalty parameters are required because the Lagrangian multipliers can be more effective for satisfying the constraint conditions [89]. However, additional variables, i.e. Lagrangian multipliers, are still required.

The penalty method and augmented Lagrangian technique are adopted in this work to compute and cope with the interaction of the interface between the fibre/bar and matrix.

Chapter 3

Damage Mechanics Framework

The mechanical response of brittle materials, such as concrete weakened by a large number of micro cracks, can be studied by damage mechanics. The phenomenon of damage is exhibited by the strain softening of the material. The difference between the effect of plasticity (inelasticity) and damage on material non-linear response was interpreted by Chen [108]. Fig. 3.1 shows that the former reflects the existence of the plastic or inelastic strain, while the latter induces stiffness degradation. The non-linear response of a material is the combination of these two behaviours.

Continuum damage mechanics (CDM), pioneered by Kachanov [109], has been developed to describe progressive failure. It is based on the thermodynamics of irreversible processes, relevant assumptions such as the homogenization concept, the internal state variable theory and the kinetic law of damage growth. Damage or stiffness degradation is related to initiation, growth and interconnection of micro cracks.

A number of damage models of varying levels of complexity have been proposed to deal with this phenomenon. For example, Lubliner [110] established thermodynamic constitutive laws of solid based on internal variables. Krajcinovic et al. [111] and Ortiz [112] gave a mathematically rigorous de-

scription of damage growth in terms of vectors and tensors, respectively. Chow and Wang [113] developed the basic mathematical framework for the general case of anisotropic damage.

From the late 1970's, numerous damage models have been applied to simulate the inelastic response of brittle materials such as concrete. Typically these include Mazars' scalar damage model [114], Ladeveze's and Mazars' unilateral damage models[115, 116], Collumbet's damage model with permanent strains and induced anisotropy [117], Pijaudier-Cabot's damage model for high compressive loadings [118], La Borderie et al.'s damage model considering crack closure [79], Yazdani and Schreyer's and Fichant et al's anisotropic damage models with dilation [119, 120], as well as Baker et al.'s thermo-mechanical damage model [121, 122].

Considering that a free energy potential consists of both elastic and plastic parts and damage is linked to the elastic potential function, elastoplastic damage models and coupled plastic-damaged theory have also been suggested by, for example, Simo and Ju [123], Ju [124], Lubliner et al. [125], Oller et al.[126], Voyiadijs and Kattan [127], Luccioni et al. [128] and Lee and Fenves [8].

Other research using non local damage concepts has also been proposed by Pijaudier-Cobot et al. [129, 130] to avoid spurious mesh sensitivity in FE analysis.

All available methods on damage can be classified into three large categories: (1) micro mechanical models which provide the fundamental structure of a governing equation to model micro structural changes and individual micro crack growth; (2) phenomenological continuum damage models which model discontinuous micro cracks according to 'observable' state variables; (3) statistical methods which focus on universal trends in the statistics of

the micro structural disorder. All the damage models referred to above can be classified into the phenomenological approach. Based on this approach, some other damage models for concrete will be developed in this thesis.

First, in this chapter, phenomenological models are briefly introduced. This includes the basic forms of thermodynamic potential function, the description of damage parameters and the governing equations of damage evolution.

3.1 Thermodynamic Potential

Observing a typical response of reinforced concrete subjected to cyclic loading (see Fig. 3.2) it is found that the inelastic deformation and the stiffness degradation increase with strain, especially in the strain softening regime. The behaviour is caused by the propagation and coalescence of micro cracks inside concrete and at the interfaces between reinforcement and concrete. We know that thermodynamics is a science which deals with energy and its transformation and with certain relationships between the properties of substances. As viewed from thermodynamics, the foregoing behaviour is induced by irreversible damage and an increase in entropy (a property of matter) during the loading process.

Consider a deformable body under a static loading and subjected to progressive damage. The internal energy per unit volume U of the body is a function of strain ϵ, entropy η, an internal damage variable D and an internal plasticity variable β.

Based on the hypothesis of uncoupled elasticity [131], the elastic and plastic potential energy function can be written as

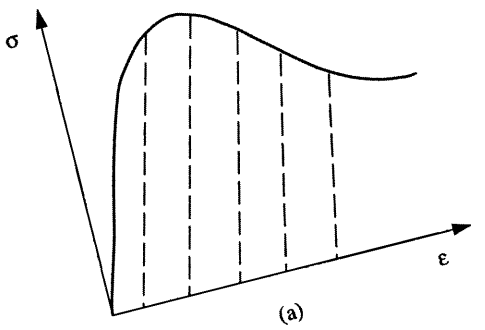

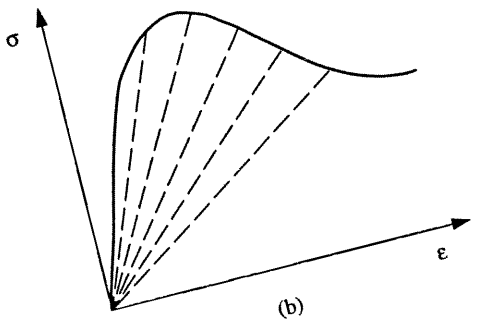

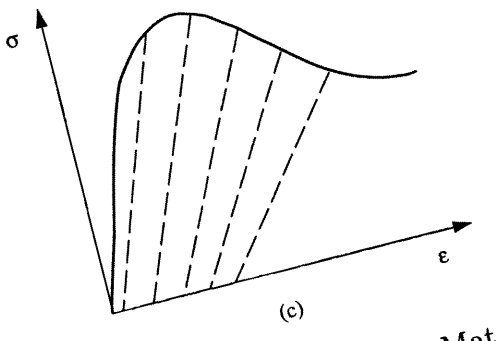

Figure 3.1: Effect of Plasticity and Damage on Material Non-linearity: (a) Elasto-Plastic Solid; (b) Progressively Damaged Solid; (c) Plastic-Damaged Solid

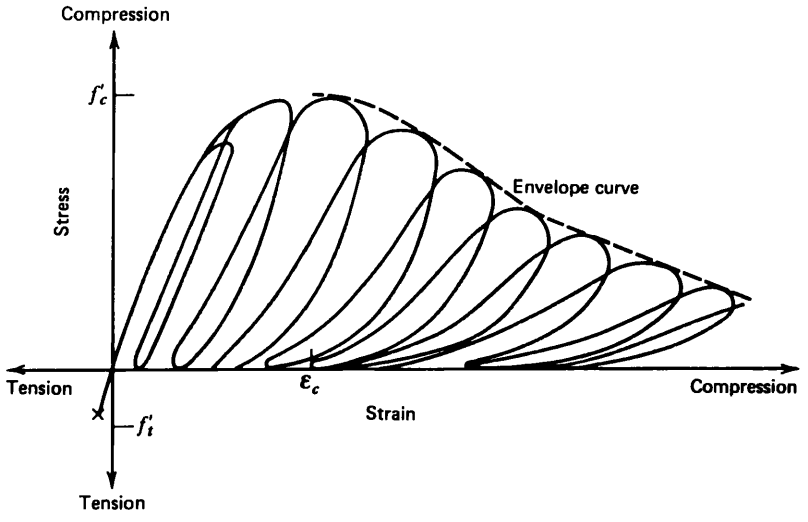

Figure 3.2: Typical Behaviour of Reinforced Concrete under Cyclic Loading [5]

$$U(\epsilon^e, \eta, D, \beta) = U^e(\epsilon^e, \eta, D) + U^p(\beta) \tag{3.1}$$

$$= (1 - D)U_0^e(\epsilon^e, \eta) + U^p(\beta) \tag{3.2}$$

where superscripts e and p denote elastic and plastic respectively. U_0^e is the elastic energy of a virgin material.

The damage variable D may be a scalar or a tensorial quantity. The scalar representation implies that the damage is isotropic and ignores the influence of the orientation of micro defects. Within the domain of D ($0 \leq D \leq 1$), the case $D = 0$ means that the material is undamaged, whilst the case $D = 1$ is at fracture.

Since this thesis only involves the damage relative to elastic potential energy, the plastic part of potential energy will be left out of consideration in the following.

To derive a family of thermodynamic constitutive relations, it is neces-

sary to start with the second law of thermodynamics. This states that the entropy of an isolated system increases in all real processes (spontaneous and irreversible). From this law, the Clausius-Duham Inequality for a irreversible process (not necessarily adiabatic) is given by

$$\dot{\eta} - \nabla(\frac{Q}{\Theta}) \geq 0 \tag{3.3}$$

where Q is heat energy, and Θ is temperature. ∇ is a gradient operator.

Furthermore, the change of internal energy in a body should be equal to the sum of the changes of mechanical and heat energies if no kinetic and potential energies exist, and is written mathematically as

$$\dot{U} = \boldsymbol{\sigma} : \dot{\boldsymbol{\epsilon}} + \dot{Q} \tag{3.4}$$

Substituting $\dot{Q}$ into Eq. 3.3, we have

$$\Theta\dot{\eta} + \boldsymbol{\sigma} : \dot{\boldsymbol{\epsilon}} - \dot{U} - Q\frac{\Delta\Theta}{\Theta} \geq 0 \tag{3.5}$$

Using the derivative of U with respect to η, $\boldsymbol{\epsilon}$ and D, Eq. 3.5 becomes

$$(\Theta - \frac{\partial U}{\partial \eta})\dot{\eta} + (\boldsymbol{\sigma} - \frac{\partial U}{\partial \boldsymbol{\epsilon}})\dot{\boldsymbol{\epsilon}} - \frac{\partial U}{\partial D}\dot{D} - Q\frac{\Delta\Theta}{\Theta} \geq 0 \tag{3.6}$$

For an isothermal (slow loading, slow crack growth) and elastic system, $\dot{D}$ is independent of $\dot{\eta}$ and $\dot{\varepsilon}$. In order that the inequality holds for arbitrary $\dot{\eta}$ and $\dot{\varepsilon}$ in a given thermodynamic state, it is required that

$$\Theta = \frac{\partial U}{\partial \eta} \tag{3.7}$$

$$\boldsymbol{\sigma} = \frac{\partial U}{\partial \boldsymbol{\epsilon}} = K : \boldsymbol{\epsilon} \tag{3.8}$$

where K is the stiffness matrix associated with the damage variable. Due to isothermal conditions, we have

$$-\frac{\partial U}{\partial D}\dot{D} = Y\dot{D} \geq 0 \tag{3.9}$$

where Y is a thermodynamic force (damage energy release rate), a measure of damage susceptibility. The physical interpretation of Eq. 3.9 is that the damage process reduces the internal energy of a system.

Eq. 3.7 to Eq. 3.9 are the general thermodynamic constitutive laws.

Two other forms of free energy are often applied in damage mechanics, i.e. Helmholtz free energy (per unit volume) A and Gibbs free energy (per unit volume) G. Generally, the Helmholtz free energy uses displacement as an independent variable, while the Gibbs free energy uses force as an independent variable. They are respectively defined as follows [119]:

$$A(\boldsymbol{\epsilon}, \Theta, D) = U(\boldsymbol{\epsilon}, \eta, D) - \Theta\eta \tag{3.10}$$

$$G(\boldsymbol{\sigma}, \Theta, D) = \boldsymbol{\sigma} : \boldsymbol{\epsilon} - A(\boldsymbol{\epsilon}, \Theta, D) \tag{3.11}$$

By the same token as before, for the Helmholtz free energy, we have

$$\eta = -\frac{\partial A}{\partial \Theta} \tag{3.12}$$

$$\boldsymbol{\sigma} = \frac{\partial A}{\partial \boldsymbol{\epsilon}} \tag{3.13}$$

$$-\frac{\partial A}{\partial D}\dot{D} \geq 0 \tag{3.14}$$

and for the Gibbs free energy

$$\eta = \frac{\partial G}{\partial \Theta} \tag{3.15}$$

$$\boldsymbol{\epsilon} = \frac{\partial G}{\partial \boldsymbol{\sigma}} \tag{3.16}$$

$$\frac{\partial G}{\partial D}\dot{D} \geq 0 \tag{3.17}$$

Clearly, the Helmholtz free energy reduces with damage, but the Gibbs free energy does the opposite. In a sense, the Helmholtz free energy is strain energy, whilst the Gibbs free energy is complementary of the Helmholtz free energy.

In addition, based on elastic damage theory, assuming all micro cracks will be closed and no residual strain will be induced by micro-defects upon complete unloading [124], the undamaged free internal energy function U_0 (also A_0 and G_0) can be expressed directly by the thermodynamic force (damage energy release rate) and conjugated to the damage variable D [124], viz.

$$Y = -\frac{\partial U(\boldsymbol{\epsilon}^e, \eta, D)}{\partial D} = U_0(\boldsymbol{\epsilon}^e, \eta) \tag{3.18}$$

The thermodynamic force may be used as an initial damage criterion.

3.2 Damage Surface and Damage Evolution Law

To determine the stress or strain states during a damage process, the evolution of damage has to be defined. This can be accomplished by a loading function (i.e. damage surface) and an evolution rule. The evolution rule can be defined in either an associated or a non-associated format. Recalling

the formulation of a yield function and plastic flow law in plasticity theory [108, 132], it is not difficult to define a corresponding damage function f, and a damage evolution law according to the normality rule. For example, for an isothermal process we can define [79, 133] the damage surface as

$$f(Y, D) = Y - Y_0 - Z = 0 \tag{3.19}$$

and the evolution rule as

$$\dot{D} = \dot{\lambda}\frac{\partial \Psi}{\partial Y} \tag{3.20}$$

where Y_0 denotes a non-negative scalar damage threshold (energy barrier) and Z is a hardening-softening control variable. $\dot{\lambda}$ is a scalar constant and $\partial\Psi/\partial Y$ is a potential gradient. The evolution rule is termed a nonassociated damage evolution law.

Eq.(3.19) states that damage in a material is initiated when the damage energy release rate exceeds the initial damage threshold Y_0.

A simple, yet important, case is when the potential function and the damage surface coincide, $\Psi = f$, i.e a so-called associated damage evolution rule (see Fig 3.3). Eq. 3.20 then becomes

$$\dot{D} = \dot{\lambda}\frac{\partial f}{\partial Y} \tag{3.21}$$

with the Kuhn-Tucker conditions

$$\boxed{\begin{aligned} \dot{\lambda} &\geq 0 \\ f &\leq 0 \\ \dot{\lambda} f &= 0 \end{aligned}} \tag{3.22}$$

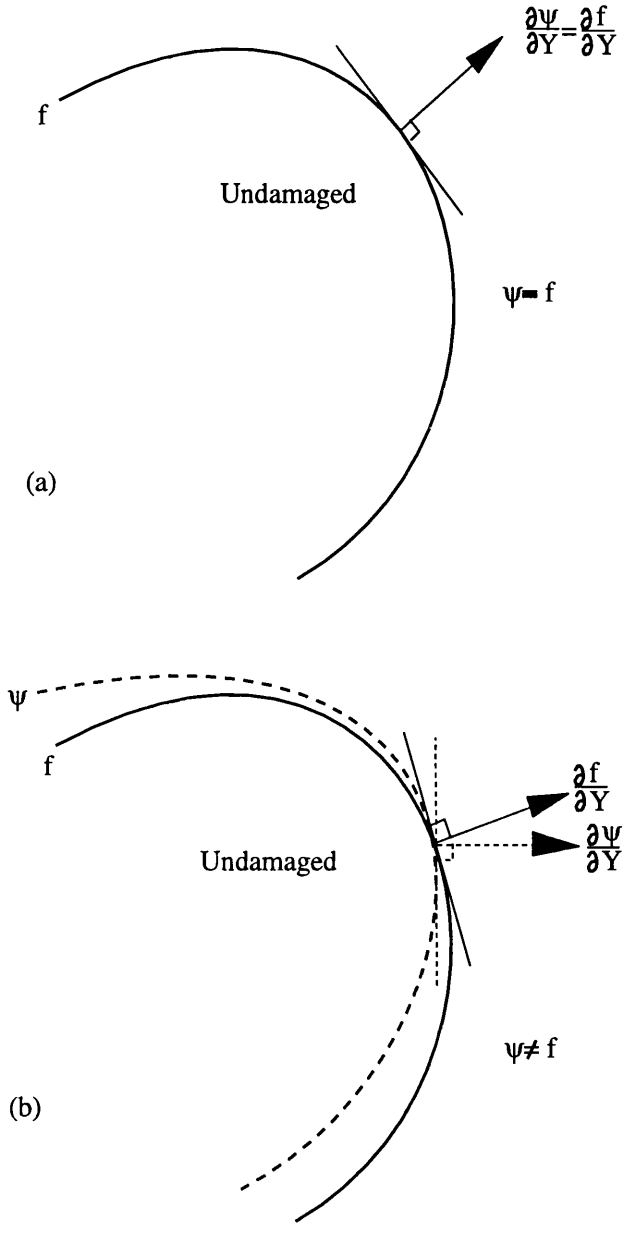

Figure 3.3: (a)Associative Evolution Rule and (b) Nonassociative Evolution Rule.

Based on the damage criterion Eq.(3.19), the loading condition can be established as follows:

$$\begin{aligned} &\text{If} \quad f < 0 && \text{then } \dot{D} = 0 \\ &\text{If} \quad f = 0 \quad \text{and} \quad \dot{f} < 0 && \text{then } \dot{D} = 0 \\ &\text{If} \quad f = 0 \quad \text{and} \quad \dot{f} = 0 && \text{then } \dot{D} = \dot{\lambda}\frac{\partial f}{\partial Y} \geq 0 \end{aligned} \tag{3.23}$$

3.3 Summary

In this chapter, the development of damage mechanics associated with brittle materials is briefly reviewed. The basic damage mechanics formulations are outlined, which include the potential energy function, thermodynamic constitutive relationships and thermodynamic force. In addition, the damage criterion, damage evolution law and loading condition are also described.

Obviously, the key steps in the analysis of damage mechanics are to determine a damage surface and damage evolution law after a proper free energy function is chosen. The development of damage models in this thesis will follow these steps.

Chapter 4

Damage Models for Concrete Subjected to Cyclic Loading

In order to develop a concrete damage model, this chapter begins with a comment and discussion on existing scalar damage models. Then a simple but basic damage model, a pure damage model, is presented. Based on this model, an inelastic-damage model is then proposed to include the inelastic strain during cyclic unloading. The emphasis will be put on the development of computational algorithms in FEM of both models. Finally, a comparison between the models and experiment is made.

4.1 Introduction

A number of damage models have been developed to describe the non-linear evolution of concrete structures under monotonic and cyclic loading. Some of these were discussed in Chapter 3. The sophistication of the models depends on the number and type of internal variables. Existing damage models can be categorized into two classes: isotropic models which use a scalar damage variable, or anisotropic models which a tensorial damage variable. Those of Mazars [114, 116], Ladeveze [115] and La Borderie et al [79] are typical of

the first class, whilst Fichant's model [120] is typical of the second.

Among the isotropic damage models, Mazars' single scalar damage model has a simple form, where damage is coupled with elasticity. The inelastic behaviour of material due to damage is piloted by changing the virgin Young's modulus E_0 to E, i.e. $E = E_0(1 - D)$.

A Helmholtz elastic state potential was adopted for concrete under isothermal condition, as follows:

$$A^e = \frac{1}{2}(1 - D)\epsilon^e : K^0 : \epsilon^e \tag{4.1}$$

where K^0 is the virgin elastic tensor.

An equivalent tensile strain $\tilde{\epsilon}$ controls the evolution of damage. This is defined as

$$\tilde{\epsilon} = \sqrt{\sum_{1}^{3}(< \epsilon_i >_+)^2} \qquad (< x >_+ = \frac{|x| + x}{2}) \tag{4.2}$$

with the damage criterion

$$\tilde{\epsilon} - Z(D) = 0 \tag{4.3}$$

where ϵ_i are the principal strains, and $Z(D)$ is a hardening-softening parameter.

Eqs. 4.2 and 4.3 imply that compressive strain will not induce damage, but the transverse strain caused by Poisson's ratio will. This is generally known to violate experimental observation.

This model can be used for the case of monotonic loading, but not for the certain cases of reverse loading [134]. Typical results are presented in Fig.4.1.

Regarding the fact that a different extent of damage exists for concrete under tension and compression, a unilateral damage model was proposed by

Ladeveze [115]. In this model, the stress tensor is decomposed into a positive part $\boldsymbol{\sigma}_+$ and a negative part $\boldsymbol{\sigma}_-$. Two damage variables, D_t and D_c, are used to describe damage related to positive and negative stresses respectively. The state potential is then given in a Gibbs free energy form as:

$$\begin{aligned} G^e &= G^e(\boldsymbol{\sigma}_+) + G^e(\boldsymbol{\sigma}_-) \\ &= \frac{1}{2}\Big\{\frac{1}{E_0(1-D_t)}[(1+\nu_0)(\boldsymbol{\sigma}_+ : \boldsymbol{\sigma}_+) - \nu_0 Tr^2\boldsymbol{\sigma}] \\ &\quad + \frac{1}{E_0(1-D_c)}[(1+\nu_0)(\boldsymbol{\sigma}_- : \boldsymbol{\sigma}_-) - \nu_0 Tr^2\boldsymbol{\sigma}]\Big\}. \end{aligned} \tag{4.4}$$

in which $Tr\boldsymbol{\sigma} = \sigma_{kk}$, and E_0 and ν_0 are Young's modulus and the Poisson's ratio of the virgin material. The evolution of damage is piloted by two damage energy release rates, Y_t and Y_c, corresponding to tensile and compressive damage respectively. Fig.4.2 shows typical results.

As pointed out by La Borderie [79], this treatment of stress in Eq. 4.4 results inevitably in non one-to-one stress-strain relationship in the constitutive law. From Fig. 4.2, it can be observed that the each loading follows the same initially loading path which is not acceptable.

La Borderie modified the above model by eliminating the influence of

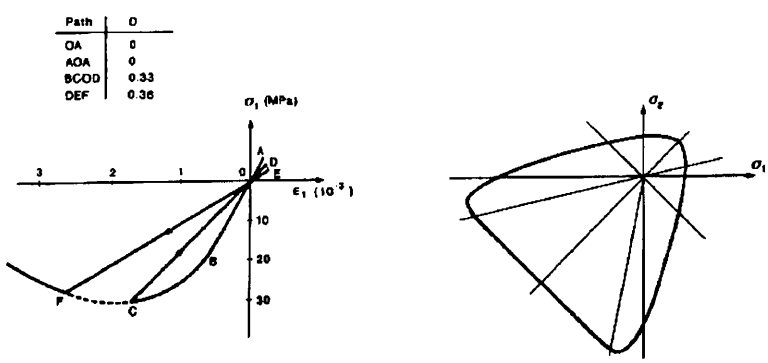

Figure 4.1: Response of Damage Model with One Scalar Damage Variable [6]

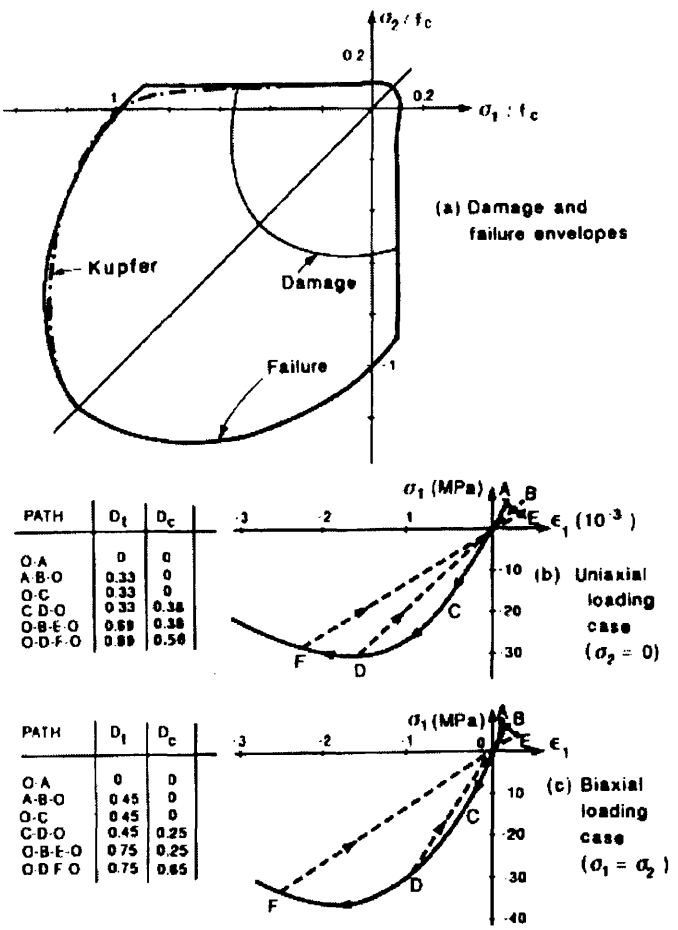

Figure 4.2: Response of Damage Model with Two Scalar Damage Variables [6]

damage on transverse deformation, and took inelastic strain and crack closure into account. To achieve this, a new form of the Gibbs free energy was chosen as a state potential as follows:

$$\begin{aligned} G^e &= \frac{\boldsymbol{\sigma}_+ : \boldsymbol{\sigma}_+}{2E_0(1-D_t)} + \frac{\boldsymbol{\sigma}_- : \boldsymbol{\sigma}_-}{2E_0(1-D_c)} + \frac{\nu_0}{2E_0}(\boldsymbol{\sigma} : \boldsymbol{\sigma} - Tr^2\boldsymbol{\sigma}) + \\ &+ \frac{\kappa_t D_t}{E_0(1-D_t)}\chi(\boldsymbol{\sigma}) + \frac{\kappa_c D_c}{E_0(1-D_c)}Tr(\boldsymbol{\sigma}) + \\ &+ H_t(z_t) + H_c(z_c) \end{aligned} \tag{4.5}$$

in which the two scalars damage variables D_t and D_c are associated with tension and compression respectively, and two parameters κ_t and κ_c are introduced to cover inelastic strain. $H_t(z_t)$ and $H_c(z_c)$ are hardening-softening functions. A crack closure function, $\chi(\boldsymbol{\sigma})$, was used to describe the degradation of tensile inelastic strain with crack closing, i.e.

$$\begin{aligned} \chi(\boldsymbol{\sigma}) &= Tr(\boldsymbol{\sigma}) && \text{when} \quad Tr(\boldsymbol{\sigma}) \in [0, \infty] \\ \chi(\boldsymbol{\sigma}) &= (1 + \frac{Tr(\boldsymbol{\sigma})}{2\sigma_\chi})Tr(\boldsymbol{\sigma}) && \text{when} \quad Tr(\boldsymbol{\sigma}) \in [-\sigma_\chi, 0] \\ \chi(\boldsymbol{\sigma}) &= -\frac{\sigma_\chi}{2} && \text{when} \quad Tr(\boldsymbol{\sigma}) \in [-\infty, -\sigma_\chi] \end{aligned}$$

where σ_χ is crack closure stress. For clarity, this functional relation is plotted in Fig. 4.3.

By differentiation of the potential Eq. 4.5 with respect to $\boldsymbol{\sigma}$, D_t, and D_c etc. respectively, the thermodynamic constitutive relationships are obtained.

$$\boldsymbol{\epsilon} = \frac{\partial G}{\partial \boldsymbol{\sigma}} = \boldsymbol{\epsilon}^e + \boldsymbol{\epsilon}^{in} \tag{4.6}$$

$$Y_t = \frac{\partial G}{\partial D_t} = \frac{\boldsymbol{\sigma}_+ : \boldsymbol{\sigma}_+ + 2\kappa_t\chi(\boldsymbol{\sigma})}{2E_0(1-D_t)^2} \tag{4.7}$$

$$Y_c = \frac{\partial G}{\partial D_c} = \frac{\boldsymbol{\sigma}_- : \boldsymbol{\sigma}_- + 2\kappa_c\chi(\boldsymbol{\sigma})}{2E_0(1-D_c)^2} \tag{4.8}$$

$$Z_i = \frac{\partial H(z_i)}{\partial z_i} = [Y_{0i} + \frac{1}{A_i}(\frac{-z_i}{1+z_i})^{\frac{1}{B_i}}] \qquad (i = c,\ t) \tag{4.9}$$

where A_i, B_i, Y_{0i} and z_i are parameters to be determined, and $\boldsymbol{\epsilon}^e$ and $\boldsymbol{\epsilon}^{in}$ are the elastic and inelastic strain tensors respectively with the forms

$$\boldsymbol{\epsilon}^e = \frac{\boldsymbol{\sigma}_+}{E_0(1-D_t)} + \frac{\boldsymbol{\sigma}_-}{E_0(1-D_c)} + \frac{\nu_0}{E_0}(\boldsymbol{\sigma} - Tr(\boldsymbol{\sigma})\mathbf{I}) \tag{4.10}$$

and

$$\boldsymbol{\epsilon}^{in} = \frac{\kappa_t D_t}{E_0(1-D_t)}\frac{\partial \chi}{\partial \boldsymbol{\sigma}} + \frac{\kappa_c D_c}{E_0(1-D_c)}\mathbf{I} \tag{4.11}$$

in which $\mathbf{I}$ is an identity tensor.

In this model, the tensile and compressive damage are controlled respectively by following two damage surfaces:

$$f_t(Y_t, Z_t) = Y_t - Z_t$$

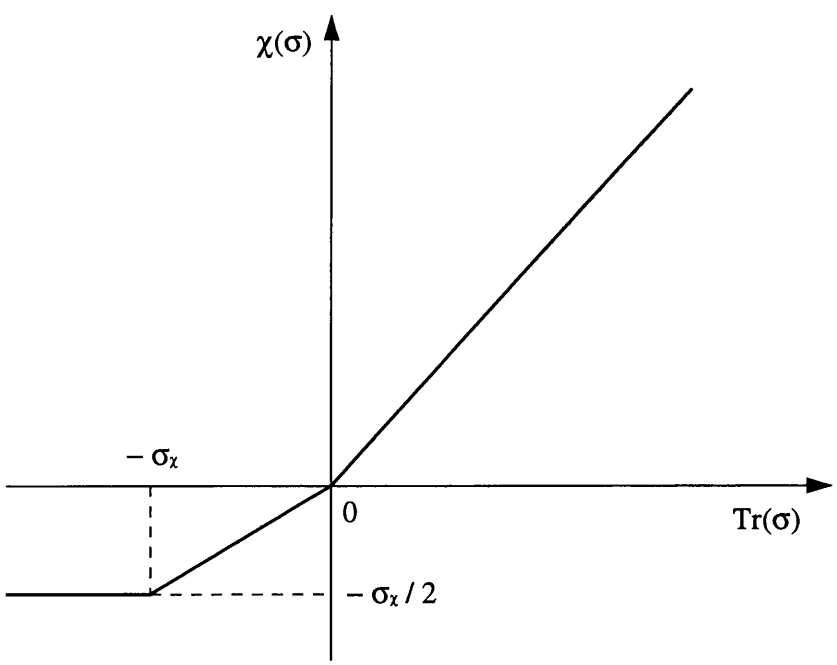

Figure 4.3: Crack Closure Function

$$f_c(Y_c, Z_c) = Y_c - Z_c \tag{4.12}$$

The features of this model are: (1) the permanent deformation caused by damage and the effect of crack closure are included; (2) the evolution of damage is dominated by the local damage energy release rates. Mazars [134] pointed out that this model was more efficient than the previous ones, but its implementation in the F.E.M. was also more difficult. Actually, only a one-dimensional version of this model has been implemented with beam elements [79].

Hence to aid implementation in the FEM, modifications of the models of La Borderie et al [79] are proposed in the following sections.

4.2 Basic Equations

Two models are developed to represent concrete subjected to monodirectional (either tensile or compressive) cyclic loading. The first model (pure damage model) does not include inelastic deformation, whilst the second (inelastic-damage model) does. To avoid the problem caused by separating stress and to enable developed models to apply to plane stress/strain states, only monodirectional loading is considered.

4.2.1 Pure Damage Model — Model I

First, a Helmholtz free energy is defined by

$$A^e = \frac{1}{2}\boldsymbol{\epsilon}^e : K : \boldsymbol{\epsilon}^e \tag{4.13}$$

in which K is an isotropic four-order tensor with the form

$$K_{ijkl} = (1 - D)K^0_{ijkl}$$

$$= \frac{E_0(1-D)}{2(1+\nu_0)}[\frac{2\nu_0}{1-2\nu_0}\delta_{ij}\delta_{kl} + \delta_{ik}\delta_{jl} + \delta_{il}\delta_{jk}] \tag{4.14}$$

where K^0_{ijkl} is the stiffness tensor of virgin material, and δ_{ij} is the Kronecker delta with

$$\delta_{ij} = \begin{cases} 1 \text{ when } i = j \\ 0 \text{ when } i \neq j \end{cases}$$

The differentiation of the potential function with respect to $\boldsymbol{\epsilon}$ and D, respectively, leads to the stress tensor and damage energy release rate as follows:

$$\begin{aligned} \boldsymbol{\sigma} &= \frac{\partial A^e}{\partial \boldsymbol{\epsilon}^e} \\ &= (1-D)K^0 : \boldsymbol{\epsilon}^e - \Delta D K^0 : \boldsymbol{\epsilon}^e \end{aligned} \tag{4.15}$$

$$Y = -\frac{\partial A^e}{\partial D} = \frac{1}{2}\boldsymbol{\epsilon}^e : K^0 : \boldsymbol{\epsilon}^e \tag{4.16}$$

4.2.2 Inelastic-Damage Model — Model II

For the inelastic-damage model, we defined a Gibbs free energy as

$$\begin{aligned} G = \frac{1}{2}[&\frac{\boldsymbol{\sigma} : \boldsymbol{\sigma}}{E_0(1-D)} + \frac{\lambda\nu_0}{E_0}(\boldsymbol{\sigma} : \boldsymbol{\sigma} - Tr^2\boldsymbol{\sigma})] \\ &+ \frac{\kappa D}{E_0(1-D)} Tr(\boldsymbol{\sigma}) \end{aligned} \tag{4.17}$$

where κ is an inelastic material parameter. λ is a parameter which is introduced to consider the effect of damage on Poisson's ratio. The second term in Eq. 4.17 defines the inelastic deformation caused by damage in a similar form to that in ref. [79], but particular attention is paid to the case of monodirectional cyclic loading.

In La Borderie et al's model, Poisson's ratio did not change with damage. However, uniaxial compression experimental results, for example ref. [7] (see Fig. 4.4), show that the increase of transverse strain after damage does not simply depend on the initial Poisson's ratio. For an elastic material under uniaxial loading, to consider the effect of Poisson's ratio, the transverse strain ε' is defined by

$$\epsilon' = -\frac{\nu_0}{E_0(1-D)}\sigma^e \tag{4.18}$$

in which σ^e is elastic stress. If we adopt the same approach in the current case, it would imply that no volume dilation occurs, which does not reflect concrete behaviour.

Therefore, to include volume dilation we replace ν by $\lambda\nu_0$, where

$$\lambda = \frac{1}{1-D^\alpha} \tag{4.19}$$

and α is a parameter with a different value for tension and compression.

Taking κ as zero, Eq. 4.17 reduces to a pure damage model.

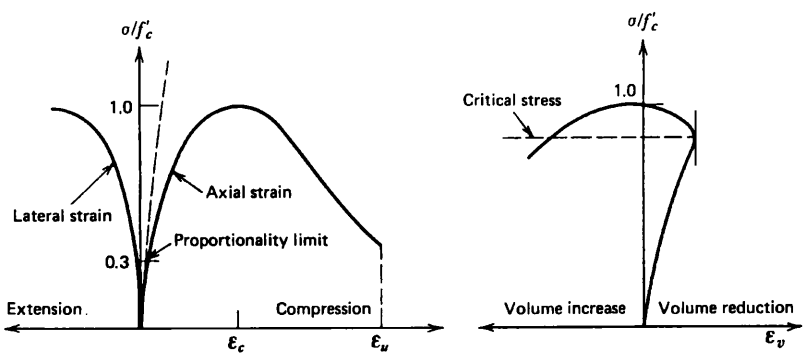

Figure 4.4: Typical Stress-Strain Curve for Concrete in Uniaxial Compression Test [7]

To derive the material constitutive relationship and the damage energy release rate we differentiate G with respect to σ and D. This leads to

$$\begin{aligned}\epsilon &= \frac{\partial G}{\partial \boldsymbol{\sigma}} \\ &= \epsilon^e + \epsilon^{in} \\ &= \frac{\boldsymbol{\sigma}}{E_0(1-D)} + \frac{\lambda\nu_0}{E_0}(\boldsymbol{\sigma} - Tr(\boldsymbol{\sigma})\mathbf{I}) + \\ &\quad + \frac{\kappa D}{E_0(1-D)}\mathbf{I}\end{aligned} \tag{4.20}$$

$$\begin{aligned}Y = \frac{\partial G}{\partial D} = \frac{\boldsymbol{\sigma} : \boldsymbol{\sigma} + 2\kappa Tr\boldsymbol{\sigma}}{2E_0(1-D)^2} \\ + \frac{\alpha D^{\alpha-1}\nu_0}{E_0(1-D^\alpha)^2}(\boldsymbol{\sigma} : \boldsymbol{\sigma} - Tr^2\boldsymbol{\sigma})\end{aligned} \tag{4.21}$$

4.3 Control Equations

To detect the onset of damage for the two models described in the previous section, the same initial damage surface is used. This is defined by

$$f(Y, D) = Y - Y_0 = 0 \tag{4.22}$$

where Y_0 is an initial damage threshold which governs the onset of damage.

With damage, the initial damage surface can expand (harden) or shrink (soften). Subsequent damage surfaces follow an evolution law, which can be defined by a hardening/softening parameter Z similar to that in Eq. 4.9, i.e.

$$f = Y - Y_0 - Z = 0 \tag{4.23}$$

and

$$Z = \frac{1}{A}(\frac{D}{1-D})^{\frac{1}{B}} \tag{4.24}$$

where A and B are parameters to be determined.

A stress point in principal stress space can be either within or on the current damage surface. When the stress state lies within the damage surface, two states may exist. One may be loading, which has not violated the initial damage criterion, and the other may be unloading. Both processes are defined by $\dot{D} = 0$. Once the stress point is on the damage surface, it is loading and is accompanied with a change of the damage surface with $\dot{D} \geq 0$. The damage parameter can be derived from Eq. 4.23 as

$$D = 1 - \frac{1}{1 + [A(Y - Y_0)]^B} \tag{4.25}$$

In summary, we have

$$\begin{aligned} \text{if} \quad & f < 0 && \text{then} \quad \dot{D} = 0, \\ \text{if} \quad & f = 0 \ \text{and} \ \dot{f} < 0 && \text{then} \quad \dot{D} = 0, \\ \text{and if} \quad & f = 0 \ \text{and} \ \dot{f} = 0 && \text{then} \quad \dot{D} \geq 0 \end{aligned} \tag{4.26}$$

With these basic equations, the key issue in the next step is how to implement in a finite element analysis.

4.4 Computational Technique

The implemention of the pure damage model is straightforward because after the onset of damage, the damage variable can be determined directly through the damage energy release rate. However, the implementation of the inelastic-damage model is more complex, since the energy release rate Y depends on

the instantaneous stress and the damage state. Therefore, a damage identification and iteration scheme is developed here.

Two aspects have to be taken into account: firstly detecting damage and then defining the stress state. From Eqs. 4.20 and 4.21, clearly the damage parameter and total strain must be known. A real difficulty arises at the beginning of a loading increment. We know the total strain, but nothing about the stress and damage variable. To tackle this, a scheme has been derived here in which an undamaged elastic stress state predictor, denoted "$\boldsymbol{\sigma}_{pr}$", is assumed, and the updated values are calculated using a Euler Backward algorithm.

Denoting the start state of a loading increment as n, the end state as $n+1$, and Eqs. 4.20 and 4.21 as functions $F_i\,(i = 1, 2)$, a set of non-linear simultaneous equations can be set up in terms of a Taylor expansion.

Before damage or under unloading:

$$\left\{ \boldsymbol{\sigma}^{n+1} \right\} = \left\{ \boldsymbol{\sigma}^{n} \right\} + [J]^{-1} \left\{ F_1^n \right\} \tag{4.27}$$

After damage:

$$\left\{ \begin{array}{c} \boldsymbol{\sigma}^{n+1} \\ D^{n+1} \end{array} \right\} = \left\{ \begin{array}{c} \boldsymbol{\sigma}^{n} \\ D^{n} \end{array} \right\} + [J]^{-1} \left\{ \begin{array}{c} F_1^n \\ F_2^n \end{array} \right\} \tag{4.28}$$

where

$$[J] = \left[\begin{array}{cc} \dfrac{\partial F_1^n}{\partial \sigma} & \dfrac{\partial F_1^n}{\partial D} \\ \dfrac{\partial F_2^n}{\partial \sigma} & \dfrac{\partial F_2^n}{\partial D} \end{array} \right] \tag{4.29}$$

with

BOX 4.1: Basic Algorithm for Pure Damage Model.

1. Evaluate energy release rate
   $Y^{n+1} = \frac{1}{2}\boldsymbol{\epsilon}^{n+1} : K^0 : \boldsymbol{\epsilon}^{n+1}$
2. Check if damaged in previous loading
   IF f^n <Tol THEN $\Delta D = 0$ GOTO 4
3. Check present iteration is under loading or unloading
   IF $Y^{n+1} < Y^n$ THEN $\Delta D = 0$ GOTO 6
4. Check if current damage condition is violated
   IF $f^{(n+1)} <$ Tol THEN $\Delta D = 0$ GOTO 6
5. Evaluate damage parameter
   $$D^{n+1} = 1 - \frac{1}{1 + [A(Y^{n+1} - Y_0)]^B}$$
6. Evaluate stresses
   $\boldsymbol{\sigma}^{n+1} = (1 - D^n)K^0 : \boldsymbol{\epsilon}^{n+1} - \Delta D K^0 : \boldsymbol{\epsilon}^{n+1}$
   or $\boldsymbol{\sigma}^{n+1} = (1 - D^{n+1})K^0 : \boldsymbol{\epsilon}^{n+1}$

$$
\begin{aligned}
\frac{[\partial F_1^n]_{ij}}{\partial \sigma_{kl}} &= \frac{1}{E_0}\left(\frac{1}{1-D} + \frac{\nu_0}{1-D^\alpha}\right)\delta_{ik}\delta_{jl} - \frac{\nu_0}{E_0(1-D^\alpha)}\delta_{kl}\delta_{ij} \\
\frac{[\partial F_1^n]_{ij}}{\partial D} &= \frac{\sigma_{ij}}{E_0}\left[\frac{1}{(1-D)^2} + \frac{\alpha D^{\alpha-1}\nu_0}{(1-D^\alpha)^2}\right] + \frac{\delta_{ij}}{E_0}\left[\frac{\kappa}{(1-D)^2} - \frac{\alpha D^{\alpha-1}\nu_0\sigma_{mm}}{(1-D^\alpha)^2}\right] \\
\frac{\partial F_2^n}{\partial \sigma_{kl}} &= \frac{\boldsymbol{\sigma}_{kl} + \kappa\delta_{kl}}{E_0(1-D)^2} + \frac{2\alpha D^{\alpha-1}\nu_0}{E_0(1-D^\alpha)^2}(\boldsymbol{\sigma}_{kl} - \sigma_{mm}\delta_{kl}) \\
\frac{\partial F_2^n}{\partial D} &= \frac{\sigma_{ij}\sigma_{ij} + 2\kappa\sigma_{mm}}{E_0(1-D)^3} + \frac{2(\alpha D^{\alpha-1})^2\nu_0}{E_0(1-D^\alpha)^3}(\sigma_{ij}\sigma_{ij} - \sigma_{mm}^2) \\
&\quad - \frac{1}{AB}\left(\frac{D}{1-D}\right)^{\frac{1}{B-1}}\left(\frac{1}{1-D}\right)^2.
\end{aligned}
\tag{4.30}
$$

Boxes 4.1 and 4.2 show the details of the algorithms for the two models, respectively.

BOX 4.2: Basic Algorithm for Inelastic-Damage Model.

1. Evaluate predictor stress state and energy release rate
   $\boldsymbol{\sigma}_{pr}^{n+1}$, Y_{pr}^{n+1}
2. Check if damaged in previous loading
   IF $f^n <$ Tol THEN $\Delta D = 0$ GOTO 6
3. Check present increment is under loading or unloading
   IF $(Y^{n+1})_{pr} < (Y^n)_{pr}$ THEN $\Delta D = 0$ GOTO 6
4. Check if current damage condition is violated
   IF $(f^{(n+1)})_{pr} <$ Tol THEN $\Delta D = 0$ GOTO 6
5. Iterate non-linear simultaneous equations Eq.4.28
   for evaluating the change in stress $\boldsymbol{\sigma}$ and damage variable D
   GOTO 7
6. Iterate non-linear simultaneous equations Eq.4.27
   for evaluating the change in stress $\boldsymbol{\sigma}$
7. Update stresses, damage parameter and energy release rate
   $\boldsymbol{\sigma}^{n+1} = \boldsymbol{\sigma}^n + \Delta\boldsymbol{\sigma}$
   $D^{n+1} = D^n + \Delta D$
   $$Y^{n+1} = \frac{\boldsymbol{\sigma}^{n+1} : \boldsymbol{\sigma}^{n+1} + 2\kappa Tr(\boldsymbol{\sigma}^{n+1})}{2E_0(1 - D^{n+1})^2} \quad \text{(before damage)}$$
   $$Y^{n+1} = Y_0 + \frac{1}{A}\left(\frac{D^{n+1}}{1 - D^{n+1}}\right)^{\frac{1}{B}} \quad \text{(after damage)}$$

4.5 Numerical Examples

The models are assessed under uniaxial cyclic tension and uniaxial cyclic compression with plane strain and plane stress elements, respectively. Both one element and four elements tests have been conducted. Figs. 4.5 and 4.6 show respectively the cyclic responses of the two models, with the following parameters chosen only for the purpose of testing the cyclic trend of concrete.

$$
\begin{aligned}
E_0 &= 31800 MPa \\
\nu_0 &= 0.2 \\
Y_0 &= 3.35 \times 10^{-2}\, MPa \text{ (for cyclic tension)} \\
&= 0.15 \times 10^{-1}\, MPa \text{ (for cyclic compression)} \\
A &= 4.0 \times 10^{-3}\, MPa^{-1} \\
B &= 1.2 \\
\kappa &= 1000.0\, MPa \text{ (for cyclic tension)} \\
&= -4000.0\, MPa \text{ (for cyclic compression)} \\
\alpha &= 1.0 \text{ (for cyclic tension)} \\
&= 10.0 \text{ (for cyclic compression)}
\end{aligned}
$$

The validation of the inelastic damage model under cyclic tension is further evaluated by a comparison with the experimental results of ref. [9]. 4-node plane strain elements are adopted. Material constants are the same as those in the previous examples. The parameters are calibrated against the experiment with the values $A = 2 \times 10^{18}\, MPa^{-1}$, $B = 6.4$, $Y_0 = 6.45 \times 10^{-4}$ MPa, $\kappa = 3.5$ MPa, and $\alpha = 1.0$.

The result is depicted in Fig. 4.7. The numerical result of a plastic-damage model from Lee and Fenves [8] is shown in Fig. 4.8 as a comparison.

The results are found to be in reasonably good agreement with experimental results, and as good as those of the plastic-damage model.

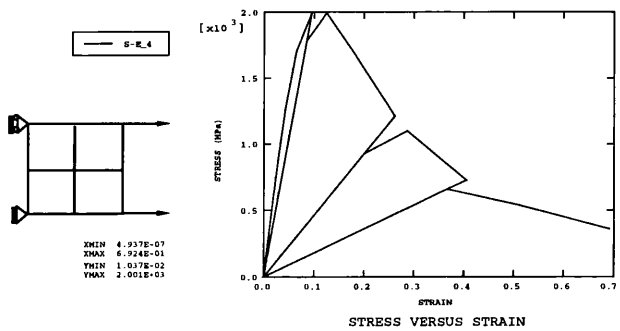

(a) Uniaxial Cyclic Tension

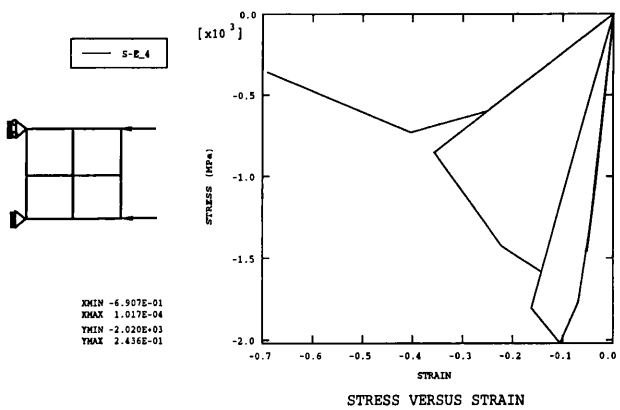

(b) Uniaxial Cyclic Compression

Figure 4.5: Numerical Results for Pure Damage Model

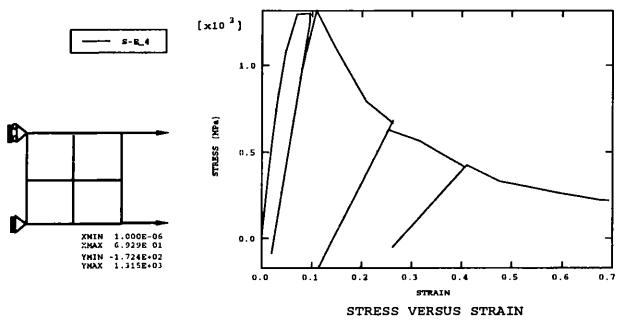

(a) Uniaxial Cyclic Tension

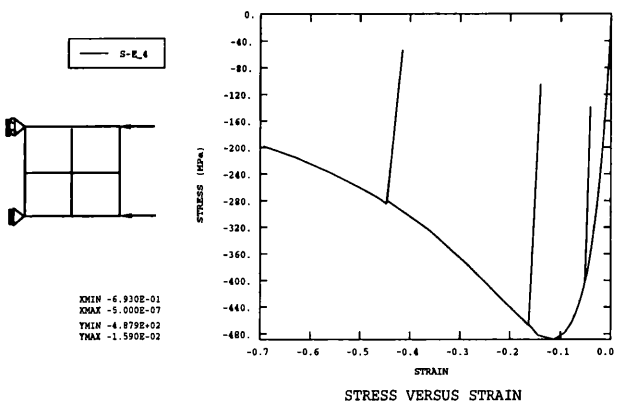

(b) Uniaxial Cyclic Compression

Figure 4.6: Numerical Results for Inelastic-Damage Model

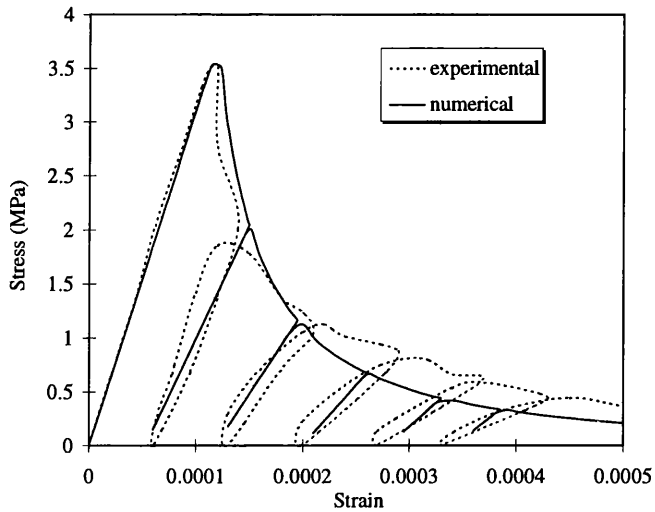

Figure 4.7: Comparison of Inelastic Damage Model with Experiment

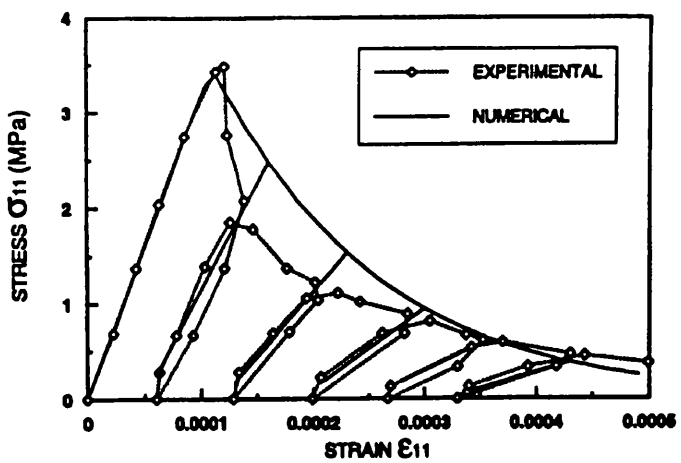

Figure 4.8: Comparison of Lee and Fenves' Model with Experiment [8]

4.6 Summary

In this chapter, a pure damage model and an inelastic damage model were proposed. In the latter, the effect of damage on transversal deformation and inelastic deformation are involved. The computational techniques for these models were developed, which enabled them to be implemented using numerical methods in plane strain and plane stress states.

Although both models only can be applied as they stand to concrete under monodirectional loading, they are an essential step towards developing more complex or biaxial damage models. The pure damage model is simple and easy to programming using FE code, while the inelastic-damage model can simulate the nonelastic strain response under monodirectional cyclic unloading very well.

The numerical results indicate the validation of the models. However, to deal with situations involving reverse cyclic loading or when tension and compression co-exist, more powerful damage models are developed in Chapter 5.

Chapter 5

Damage Models for Concrete Subjected to Reverse Cyclic and Biaxial Loading

5.1 Introduction

As noted earlier, neither of the models in Chapter 4 can simulate both tension and compression simultaneously for a plane stress or strain state. Although La Borderie et al's damage model covered inelastic strain and the effect of crack closure, the positive and negative parts of principal stress in their formulations could not be determined a priori due to a description in a stress-space. This causes difficulties for finite element implementation and its application is limited to problems which are dominated by uniaxial stress states.

In this chapter, two damage models are developed which overcome these difficulties. Two new potential functions are respectively defined for the two model. One (model III) is directly described in principal strain-space, based on the assumption that damage occurs in the principal stress/strain directions. The other (model IV) is developed using the postulate that the spher-

ical and deviatoric components of the principal strain/stress tensor have different contributions to damage.

5.2 Reverse Cyclic Loading Damage Model — Model III

5.2.1 Basic Equations

To simulate the response of concrete in the softening regime, a description of damage model in strain-space is more appropriate, because strain is known at the start of each stage and can be straightwardly separated into the positive and negative parts if needed.

In this model, damage is split into two components, tensile damage and compressive damage. The former is controlled by the tensile principal strain ϵ_p^+ and the latter by the compressive principal strain ϵ_p^-. The state potential Ψ^e is expressed in principal strain space as

$$\begin{aligned}\Psi^e = \frac{1}{2}[&(1-D_t)\epsilon_p^+ K_{pq}^0 \epsilon_q^+ + (1-D_c)\epsilon_p^- K_{pq}^0 \epsilon_q^- + \\ &+ \epsilon_p^+ K_{pq}^0 \epsilon_q^- + \epsilon_p^- K_{pq}^0 \epsilon_q^+]\end{aligned} \tag{5.1}$$

where D_t and D_c are damage variables corresponding to tension and compression, respectively. K_{pq}^0 is the stiffness tensor of virgin material, described in principal strain space. Making use of tensor transformation matrix L, we have

$$K_{pq}^0 = L_{pij} K_{ijkl}^0 L_{klp} L_{qp}^{-1}. \tag{5.2}$$

where the matrix L_{pij} can be derived through the equilibrium of forces in the principal directions of a stress point. These are written as, for a plane stress

state,

$$L_{pij} = \begin{bmatrix} \cos^2\theta & \sin^2\theta & 2\cos\theta\sin\theta \\ \sin^2\theta & \cos^2\theta & -2\cos\theta\sin\theta \end{bmatrix} \tag{5.3}$$

for a plane strain state

$$L_{pij} = \begin{bmatrix} \cos^2\theta & \sin^2\theta & 0 & 2\cos\theta\sin\theta \\ \sin^2\theta & \cos^2\theta & 0 & -2\cos\theta\sin\theta \\ 0 & 0 & 1 & 0 \end{bmatrix} \tag{5.4}$$

and

$$L_{pq} = \begin{bmatrix} (\cos^2\theta + \sin^2\theta)^2 & -2\cos^2\theta\sin^2\theta \\ -2\cos^2\theta\sin^2\theta & (\cos^2\theta + \sin^2\theta)^2 \end{bmatrix} \tag{5.5}$$

where θ is the angle between the component and the principal stress axes.

5.2.2 Constitutive Laws

From the potential Eq.5.1, the thermodynamic constitutive relations can be readily obtained.

The energy release rates corresponding to tensile damage and compressive damage are respectively written as

$$Y_t = -\frac{\partial(\Psi^e)}{\partial D_t} = \frac{1}{2}\epsilon_p^+ K_{pq}^0 \epsilon_q^+ \tag{5.6}$$

$$Y_c = -\frac{\partial(\Psi^e)}{\partial D_c} = \frac{1}{2}\epsilon_p^- K_{pq}^0 \epsilon_q^- . \tag{5.7}$$

The stress and tangential stiffness tensors are derived via the first and second derivatives of the potential with respect to strain, respectively, as follows:

$$\begin{aligned}\sigma_{ij} &= \frac{\partial \Psi^e}{\partial \epsilon_{ij}} \\ &= (1-D_t)\epsilon_p^+ K_{pq}^0 \frac{\partial \epsilon_q^+}{\partial \epsilon_{ij}} + (1-D_c)\epsilon_p^- K_{pq}^0 \frac{\partial \epsilon_q^-}{\partial \epsilon_{ij}} + \\ &\quad + \epsilon_p^+ K_{pq}^0 \frac{\partial \epsilon_q^-}{\partial \epsilon_{ij}} + \frac{\partial \epsilon_p^+}{\partial \epsilon_{ij}} K_{pq}^0 \epsilon_q^- \end{aligned} \tag{5.8}$$

$$\begin{aligned}\frac{\partial \sigma_{ij}}{\partial \epsilon_{kl}} &= \frac{\partial^2 \Psi^e}{\partial \epsilon_{ij} \partial \epsilon_{kl}} \\ &= (1-D_t)(\epsilon_p^+ K_{pq}^0 \frac{\partial^2 \epsilon_q^+}{\partial \epsilon_{ij} \partial \epsilon_{kl}} + \frac{\partial \epsilon_p^+}{\partial \epsilon_{kl}} K_{pq}^0 \frac{\partial \epsilon_q^+}{\partial \epsilon_{ij}}) + \\ &\quad + (1-D_c)(\epsilon_p^- K_{pq}^0 \frac{\partial^2 \epsilon_q^-}{\partial \epsilon_{ij} \partial \epsilon_{kl}} + \frac{\partial \epsilon_p^-}{\partial \epsilon_{kl}} K_{pq}^0 \frac{\partial \epsilon_q^-}{\partial \epsilon_{ij}}) + \\ &\quad + \epsilon_p^+ K_{pq}^0 \frac{\partial^2 \epsilon_q^-}{\partial \epsilon_{ij} \partial \epsilon_{kl}} + \frac{\partial \epsilon_p^+}{\partial \epsilon_{kl}} K_{pq}^0 \frac{\partial \epsilon_q^-}{\partial \epsilon_{ij}} + \frac{\partial \epsilon_p^+}{\partial \epsilon_{ij}} K_{pq}^0 \frac{\partial \epsilon_q^-}{\partial \epsilon_{kl}} + \\ &\quad + \frac{\partial^2 \epsilon_p^+}{\partial \epsilon_{ij} \partial \epsilon_{kl}} K_{pq}^0 \epsilon_q^- \end{aligned} \tag{5.9}$$

5.2.3 Control Function

It is well known that concrete behaves totally differently under tension and compression. Two independent damage surfaces $f_t = 0$ and $f_c = 0$ are required to control the evolution of damage under tensile and compressive loading, respectively. In the context, the subscripts t and c serve to denote tension and compression respectively.

Since the magnitude of the damage energy release rate is a measure of how susceptible the material is to damage, it is adopted to define the damage surfaces. Thus

$$f_t(Y_t, D_t) = Y_t - Z_t = 0 \tag{5.10}$$

$$f_c(Y_c, D_c) = Y_c - Z_c = 0 \tag{5.11}$$

where the hardening /softening parameter Z is expressed as

$$Z_t = Y_{t0} + \frac{1}{A_t}(\frac{D_t}{1-D_t})^{\frac{1}{B_t}} \tag{5.12}$$

$$Z_c = Y_{c0} + \frac{1}{A_c}(\frac{D_c}{1-D_c})^{\frac{1}{B_c}} \tag{5.13}$$

in which Y_0, A and B have the same definitions as those in chapter 4, except they now correspond to tensile and compressive damage.

Thus from Eqs. 5.10 to 5.13 we obtain

$$D_t = 1 - \frac{1}{1 + [A_t(Y_t - Y_{t0})]^{B_t}} \tag{5.14}$$

$$D_c = 1 - \frac{1}{1 + [A_c(Y_c - Y_{c0})]^{B_c}} \tag{5.15}$$

5.2.4 Implementation

The implementation of this model is relatively simple, since the derived formulations are described in principal strain-space and no inelastic deformation is involved at this stage. The computational scheme is the same as that for the pure damage model (model I) described in Chapter 4.

To obtain the stress tensor and tangential stiffness from Eqs. 5.8 and 5.9, the first and second derivatives of the principal strain tensor with respect to the strain tensor, i.e. $\partial\epsilon_p/\partial\epsilon_{ij}$ and $\partial^2\epsilon_p/\epsilon_{ij}\epsilon_{kl}$, have to be known.

The strain tensor ϵ_{ij} can be decomposed into two parts, a spherical part associated with a change in volume, and a deviatoric part associated with a change in shape (distortion). That is

$$\epsilon_{ij} = e_{ij} + \frac{1}{3}\epsilon_{kk}\delta_{ij} \tag{5.16}$$

where e_{ij} is the deviatoric strain tensor, and $\epsilon_{kk}/3$ is the mean strain.

Based on the coincidence of the direction of principal strain tensor with its deviatoric tensor, we can express the principal strain ϵ_p in the following form

$$\epsilon_p = e_p + \frac{1}{3}\epsilon_{kk}\delta_p. \tag{5.17}$$

in which e_p is the principal value of the deviatoric strain tensor. It can be obtained from Appendix A, i.e.

$$\begin{bmatrix} e_1 \\ e_2 \\ e_3 \end{bmatrix} = \frac{2\sqrt{J_2'}}{\sqrt{3}} \begin{bmatrix} \sin(\theta + \frac{2\pi}{3}) \\ \sin\theta \\ \sin(\theta + \frac{4\pi}{3}) \end{bmatrix} \tag{5.18}$$

with $e_1 > e_2 > e_3$ and $-\pi/6 \leq \theta \leq \pi/6$, and

$$\theta = \frac{1}{3}\arcsin(-\frac{3\sqrt{3}}{2}\frac{J_3'}{(J_2')^{\frac{3}{2}}}) \tag{5.19}$$

where $J_2^{'}$ and $J_3^{'}$ are the deviatoric strain invariants.

Hence, we have

$$\begin{aligned} \frac{\partial \epsilon_q}{\partial \epsilon_{ij}} &= \frac{\partial}{\partial \epsilon_{ij}}(e_q + \frac{\epsilon_{rr}}{3}I_q) \\ &= \frac{\partial e_q}{\partial \epsilon_{ij}} + \frac{I_q\delta_{ij}}{3} \end{aligned} \tag{5.20}$$

$$\begin{aligned} \frac{\partial^2 \epsilon_q}{\partial \epsilon_{ij}\partial \epsilon_{kl}} &= \frac{\partial}{\partial \epsilon_{kl}}(\frac{\partial e_q}{\partial \epsilon_{ij}} + \frac{\delta_{ij}I_q}{3}) \\ &= \frac{\partial^2 e_q}{\partial \epsilon_{ij}\partial \epsilon_{kl}} \end{aligned} \tag{5.21}$$

The detailed derivations for $\partial e_q/\partial \epsilon_{ij}$ and $\partial^2 e_q/\partial \epsilon_{ij}\partial \epsilon_{kl}$ in Eqs. 5.20 and 5.21 are provided in Appendix B.

5.2.5 Example

To test the response of the damage model under reversed cyclic loading, 4-node linear plane strain/stress elements are used , with the parameters $E_0 = 31.8$ GPa, $\nu_0 = 0.2$, $A_t = A_c = 4.0 \times 10^{-3} MPa^{-1}$, $B_t = B_c = 1.2$, $Y_{t0} = 3.35 \times 10^{-2}$ MPa, and $Y_{c0} = 1.5 \times 10^{-2}$ MPa. Note that the parameters are chosen arbitrarily only for testing the trend under reversed cyclic loading. The numerical results are plotted in Fig.5.1.

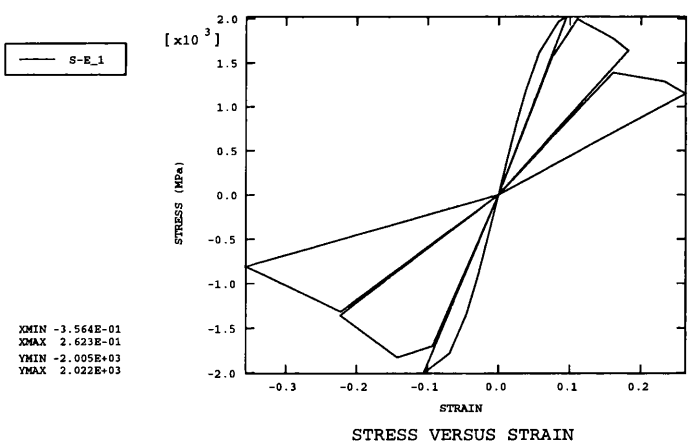

Figure 5.1: Response of Reverse Cyclic Loading from Model III

5.3 Biaxial Damage Model — Model IV

It is generally recognized that the non-linear behaviour of concrete under biaxial loading is difficult to handle mathematically and computationally. For this reason, the numerical simulation of concrete under biaxial loading is quite limited. To realise a modelling for biaxial loading, a new concept and model are proposed in this section.

The developed model stems from the idea of stiffness correction in plasticity mechanics, so a good starting point is to recall basic plasticity theory.

Consider an initial elastic body subjected to an external load. A plastic deformation can be superimposed after a certain level of stress is reached. However, the most significant feature of the plastic deformation is its irreversibility and load path dependence. The onset of plastic deformation (or yield) is governed by an initial yield criterion, for example the Drucker-Prager failure criterion. This is given in the following form.

$$f(I_1, J_2) = \alpha I_1 + \sqrt{J_2} - \kappa = 0 \tag{5.22}$$

in which $I_1 = \sigma_{ii}$ is the first invariant of stress tensor, $J_2 = s_{ij}s_{ij}/2$ is the second invariant of the deviator stress tensor s_{ij}, and α and κ are material constants. Subsequent yield conditions are described through hardening/softening rules.

A flow rule defines the direction and magnitude of the plastic strain rate vector $d\epsilon_{ij}^p$ which is assumed to be proportional to the stress gradient of a plastic potential function $\Psi(\sigma_{ij}, \epsilon_{ij}, \kappa)$. This is written by

$$d\epsilon_{ij}^p = d\lambda \frac{\partial \Psi}{\partial \sigma_{ij}} \tag{5.23}$$

where $d\lambda$ is a plastic multiplier. By means of the flow rule, the increment

constitutive relation can be expressed as

$$\begin{aligned} d\sigma_{ij} &= K^e_{ijkl}\,(d\epsilon_{kl} - d\epsilon^p_{kl}) \\ &= K^e_{ijkl}(d\epsilon_{kl} - d\lambda\frac{\partial \Psi}{\partial \sigma_{kl}}) \\ &= K^{ep}_{ijkl} d\epsilon_{kl} \end{aligned} \tag{5.24}$$

where K^e_{ijkl} and K^{ep}_{ijkl} are the tensors of elastic and elastic-plastic stiffness, respectively. $d\epsilon_{kl}$ is an increment of strain.

For the Drucker-Prager yield function with its associated flow rule, we can derive the elastic-plastic stiffness tensor as

$$\begin{aligned} K^{ep}_{ijkl} &= K^e_{ijkl} + K^p_{ijkl} \\ &= K^e_{ijkl} - \frac{1}{9\kappa\alpha^2 + G_0} H_{ij} H_{kl} \end{aligned} \tag{5.25}$$

in which G_0 is the shear modulus of material and

$$H_{ij} = 3K_0\alpha\delta_{ij} + \frac{G_0}{\sqrt{J_2}} s_{ij}. \tag{5.26}$$

where K_0 is the bulk modulus of material.

It is obvious from the above that the essence of plasticity theory is to describe the response of an elasto-plastic material by means of a stiffness modification of the material. It is found from Eq. 5.26 for a Drucker-Prager model that the modification is associated with the deviatoric stress.

The same approach is applied to the present biaxial damage model, and the different contribution of the hydrostatic and deviatoric components to damage are distinguished. A new potential function and a set of damage parameters are proposed.

5.3.1 Potential Function

The simplest form of potential energy can be written as

$$\Psi^e = \frac{1}{2}\epsilon_{uv} K_{uvst} \epsilon_{st} \tag{5.27}$$

where K_{uvst} is the stiffness of material, and ϵ_{uv} is a strain tensor.

The substitution of Eq. 5.16 into Eq. 5.27, in conjunction with considering that the hydrostatic and deviatoric components have different contributions to damage, leads to

$$\begin{aligned}\Psi^e = &\frac{1}{2}(1-D)(e_{uv}K^0_{uvst}e_{st} + \epsilon_m \delta_{uv} K^0_{uvst} e_{st} + \epsilon_m e_{uv} K^0_{uvst} \delta_{st}) + \\ &+ \frac{1}{2}(1 - D\beta)\epsilon_m^2 \delta_{uv} K^0_{uvst} \delta_{st}\end{aligned} \tag{5.28}$$

where e_{uv} is the deviatoric strain tensor, $\epsilon_m = (\epsilon_{11} + \epsilon_{22} + \epsilon_{33})/3$ is the mean stress, and δ_{uv} an identity tensor. D is a combined tension/compression damage parameter, and β is a damage multiplier associated with mean stress for uniaxial loading and with the total energy release rate for biaxial loading.

The damage parameter D is defined as a weighted average of a scalar tensile and compressive damage parameters, D_t and D_c. This has the form

$$D = \frac{\sum \sigma_p^+ D_t + \sum |\sigma_p^-| D_c}{\sum |\sigma_p|} \tag{5.29}$$

where σ_P^+ and σ_P^- are the positive and negative parts of the principal stress tensor respectively, and $\sum |\sigma_P|$ is the sum of the absolute values of principal stresses. This definition implies that damage under uniaxial loading is governed by the corresponding damage parameters, while under biaxial loading two damage parameters, D_t and D_c, contribute to the induced damage together. The effective contribution is in proportion to the ratio of relative

positive and negative principal stresses to the sum of absolute values of the principal stress. This effect is equivalent to separating the stress tensor into positive and negative parts, but it greatly simplifies the implementation in a FE code.

Based on the failure characteristics of concrete, we assume that the effect of hydrostatic component on damage is less than that of the deviatoric component. Thus a damage multiplier β is introduced to reduce the effect of damage parameter on the hydrostatic component. It is defined as a ratio of the average stress to the maximum principal stress for uniaxial loading, i.e.

$$\beta = |\frac{\sigma_m}{\sigma_1}|, \tag{5.30}$$

while for biaxial loading it is related to total energy release rate by

$$\beta = 1 - \frac{1}{1 + A_m Y_E e^{-B_m Y_E}} \tag{5.31}$$

in which A_m and B_m are two parameters to be determined, and Y_E is the total energy release rate. Clearly, we have $\beta \leq 1$.

5.3.2 Constitutive and Evolution Laws

From Eq.5.28, the thermodynamic force, stress, and tangential stiffness can be derived as follows

$$Y_t = \frac{1}{2}\frac{\sum \sigma_p^+}{\sum |\sigma_p|}[\epsilon_{uv} K^0_{uvst} \epsilon_{st} - (1-\beta)\epsilon_m^2 \delta_{uv} K^0_{uvst} \delta_{st}] \tag{5.32}$$

$$Y_c = \frac{1}{2}\frac{\sum |\sigma_p^-|}{\sum |\sigma_p|}[\epsilon_{uv} K^0_{uvst} \epsilon_{st} - (1-\beta)\epsilon_m^2 \delta_{uv} K^0_{uvst} \delta_{st}] \tag{5.33}$$

$$\sigma_{ij} = (1 - \frac{\sum \sigma_p^+}{\sum |\sigma_p|} D_t - \frac{\sum |\sigma_p^-|}{\sum |\sigma_p|} D_c) K^0_{ijst} \epsilon_{st} + \\ + (1 - \beta)(\frac{\sum \sigma_p^+ D_t + \sum |\sigma_p^-| D_c}{\sum |\sigma_p|}) \frac{\epsilon_m}{3} \delta_{ij} \delta_{uv} K^0_{uvst} \delta_{st} \qquad (5.34)$$

$$\frac{\partial \sigma_{ij}}{\partial \epsilon_{ij}} = (1 - \frac{\sum \sigma_p^+}{\sum |\sigma_p|} D_t - \frac{\sum |\sigma_p^-|}{\sum |\sigma_p|} D_c) K^0_{ijkl} + \\ + (1 - \beta)(\frac{\sum \sigma_p^+ D_t + \sum |\sigma_p^-| D_c}{\sum |\sigma_p|}) \frac{\delta_{ij} \delta_{kl}}{9} \delta_{uv} K^0_{uvst} \delta_{st} \qquad (5.35)$$

The damage surface and evolution law have the same forms as in model III.

5.3.3 Implementation

We denote the beginning state of a loading increment as n, and the end state as $n + 1$. Box 5.1 presents the detailed algorithm of this model.

5.4 Applications to Concrete

In this section, several examples are presented to test the proposed models. The finite element implementation uses a single two-dimensional, 8-node quadratic plane stress element and are conducted for uniaxial loading, biaxial loading, as well as reverse cyclic loading. Loading is controlled by displacement to simulate the response of concrete in the softening regime. In order to compare with experimental results from refs. [9] and [5] the following material properties are adopted in numerical computation: Young's Modulus $E_0 = 31.8GPa$, Poisson's ratio $\nu_0 = 0.18$, maximum tensile strength $3.5MPa$, and maximum compressive strength $-27.6MPa$. The parameters calibrated from the experiments are listed in Tab. 5.4. It should be noted that making

BOX 5.1: Basic Algorithm for Model IV

1. Evaluate energy release rate
   Y_t^{n+1} and Y_c^{n+1}
2. Check present increment is loading or unloading
   IF $Y_t^{n+1} < Y_t^n$ THEN $\Delta D_t = 0$ GOTO 6
   IF $Y_c^{n+1} < Y_c^n$ THEN $\Delta D_c = 0$ GOTO 6
3. Check if current damage conditions are violated
   IF $f_t^{n+1} <$ Tol THEN $\Delta D_t = 0$ GOTO 5
   IF $f_c^{n+1} <$ Tol THEN $\Delta D_c = 0$ GOTO 5
4. Evaluate tensile and compressive damage parameters, respectively.
   $$D_t^{n+1} = 1 - \frac{1}{1 + [A_t(Y_t^{n+1} - Y_{t0})]^{B_t}}$$
   $$D_c^{n+1} = 1 - \frac{1}{1 + [A_c(Y_c^{n+1} - Y_{c0})]^{B_c}}$$
   GOTO 6
5. $D_t^{n+1} = D_t^n$
   $D_c^{n+1} = D_c^n$
6. Evaluate total damage parameter D
   IF unloading THEN $D^{n+1} = D^n$
   ELSE evaluate total damage parameter D^{n+1} (Eq. 5.29)
7. Evaluate stress tensor, σ_{ij}
8. Evaluate tangential stiffness, $\partial\sigma_{ij}/\partial\epsilon_{ij}$
9. Evaluate the eigenvalue of stress tensor, σ_p
10. Evaluate and Update parameters
    $\frac{\sum \sigma_p^+}{\sum |\sigma_p|}$, $\frac{\sum |\sigma_p^-|}{\sum |\sigma_p|}$, β, Z_t and Z_c

Table 5.1: Parameters for Numerical Computation

	Model	III	Model	IV
A_t	5000.0	MPa^{-1}	7000.0	MPa^{-1}
A_c	21.0	MPa^{-1}	29.0	MPa^{-1}
A_m			2.0	MPa^{-1}
B_t	1.3		1.1	
B_c	1.05		0.94	
B_m			0.7	MPa^{-1}
Y_{t0}	2.0×10^{-4}	MPa	1.9×10^{-4}	MPa
Y_{c0}	4.0×10^{-4}	MPa	3.0×10^{-4}	MPa

small changes to these parameters, other concrete with different properties can be modeled. If only the ultimate strength is required, modifying A_t and A_c is sufficient.

5.4.1 Uniaxial Loading Test

Figs.5.2 and 5.3 illustrate the results of the two models III and IV under uniaxial tension and compression. These are compared with the experimental results under tensile loading (Gopalaratnam and Shah (1985) [9]) and compressive loading (Karsan and Jirsa(1969) [5]). Excellent agreement between the numerical analyses and the experimental results are obtained. Similar comparisons were carried out by Lee and Fenves (1998) [8] using a plastic-damage model (see Fig. 5.4). It is demonstrated that the proposed models can simulate concrete response as well as the plastic-damage model. It also shows closer agreement than Lee and Fenves's model during certain stages under uniaxial tension loading.

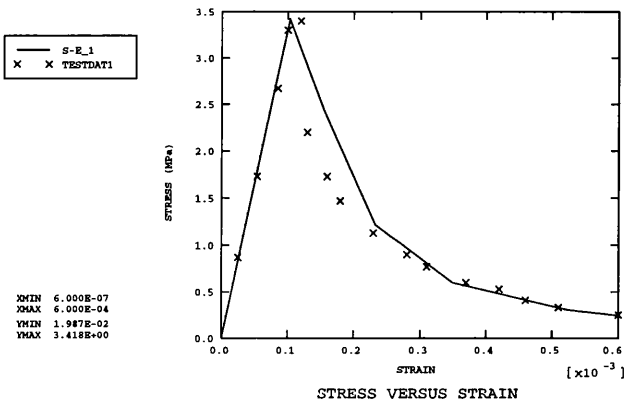

(a)

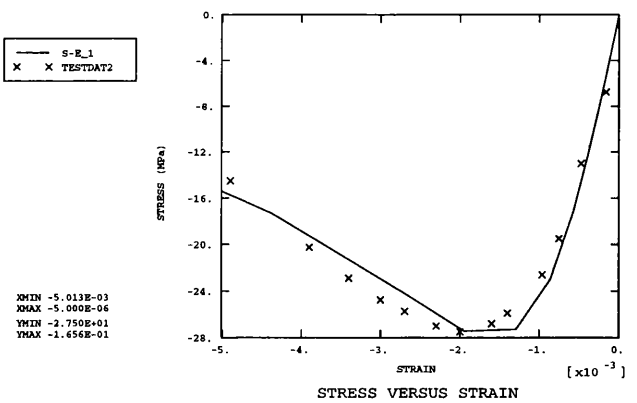

(b)

Figure 5.2: Comparison of Numerical Solutions of Model III with Experimental Results under (a) Uniaxial Tension [9]; and (b) Uniaxial Compression [5]

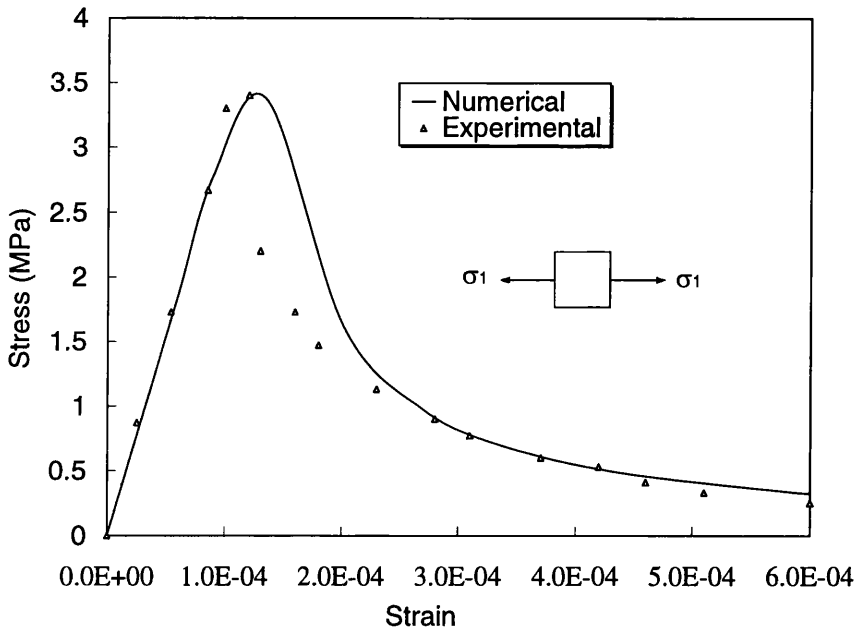

(a)

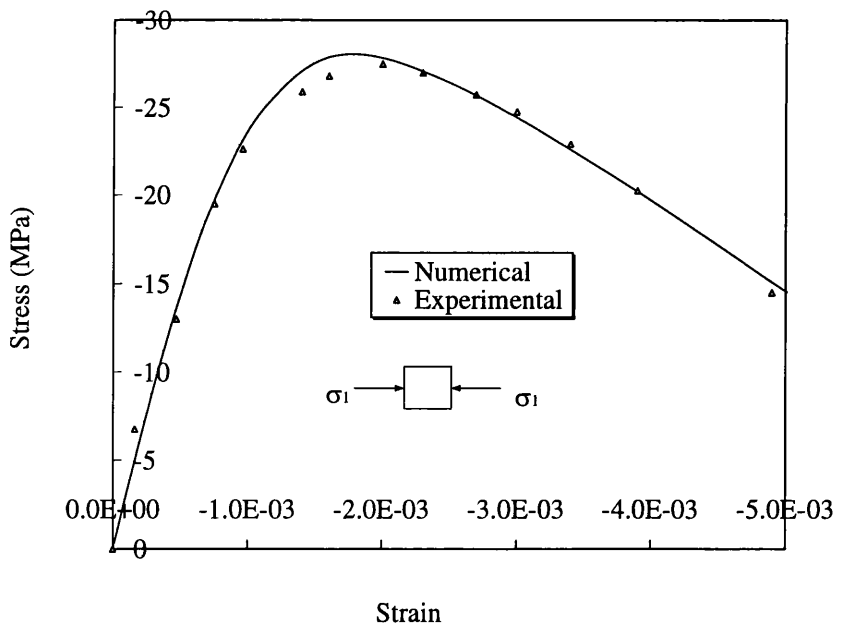

(b)

Figure 5.3: Comparison of Numerical Solutions of Model IV with Experimental Results under (a) Uniaxial Tension [9]; and (b) Uniaxial Compression [5]

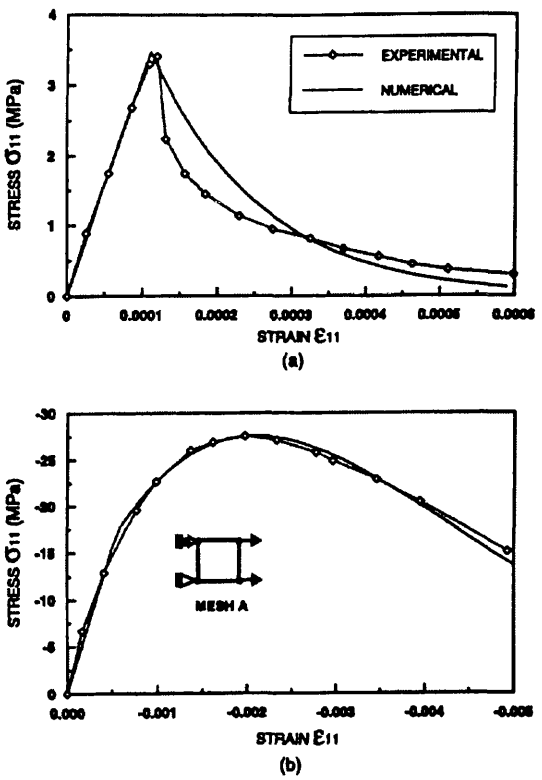

Figure 5.4: Comparison of Numerical Solutions of Lee et al's Model with Experimental Results under (a) Uniaxial Tension (Gopalarantnam and Shah 1985); and (b) Uniaxial Compression (Karasan and Jirsa 1969)

5.4.2 Biaxial Loading Test

Numerical simulation using model IV for biaxial tensile and compressive loading are carried out respectively. Fig. 5.5 provides an entire biaxial tensile stress and strain relation.

Figs. 5.6 and 5.7 give the numerical results of biaxial tension and compression under three stress ratios respectively, in conjunction with the corresponding experimental results of Kupfer et al [10]. The numerical analyses show a very good agreement in trend with Kupfer et al's experimental results.

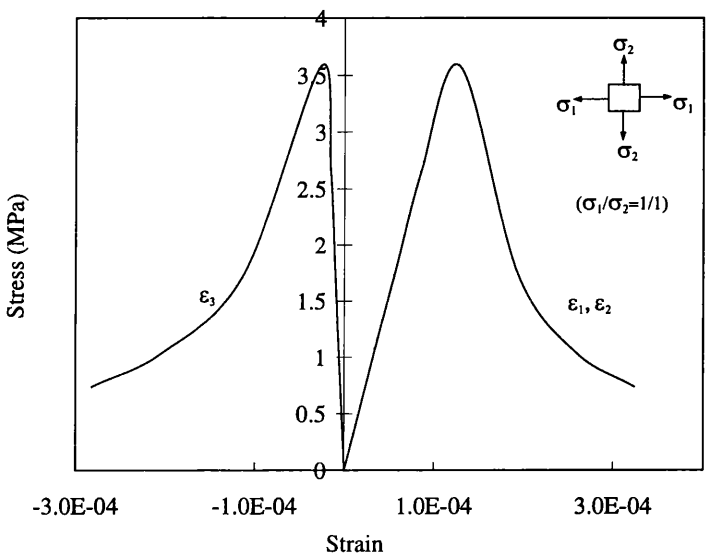

Figure 5.5: Relationship of Stress versus Strain under Biaxial Tension

5.4.3 Reverse Cyclic Loading Test

Reverse cyclic loading is imposed on the same model as above. The result is depicted in Fig.5.8. Loading paths are tensile loading, tensile unloading, compressive loading and compressive unloading, and the whole cycle is repeated several times. The detailed paths are as follows:

$$0 \Rightarrow 1 \Rightarrow 0 \Rightarrow 2 \Rightarrow 0 \Rightarrow 3 \Rightarrow 4 \Rightarrow 0 \Rightarrow 5 \Rightarrow 0 \Rightarrow 6 \Rightarrow 7 \Rightarrow 0 \Rightarrow 8 \Rightarrow 0$$

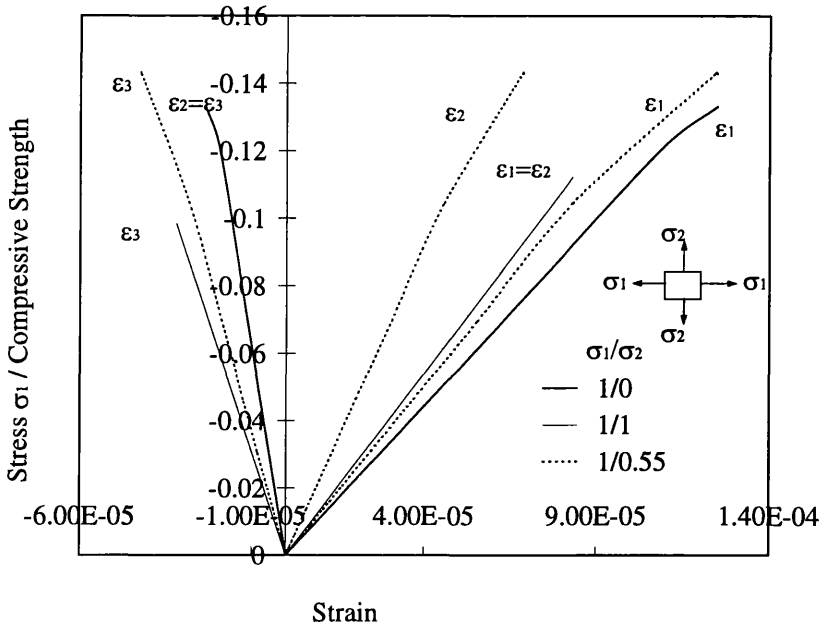

(a)

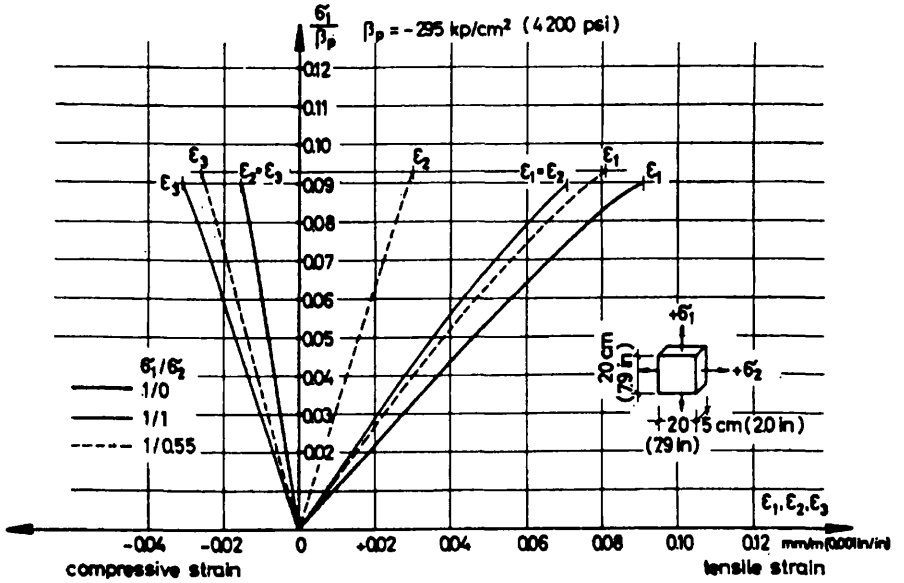

(b)

Figure 5.6: Stress-Strain Relationship under Biaxial Tension (a) Numerical Results from Model IV; (b) Experimental Results [10]

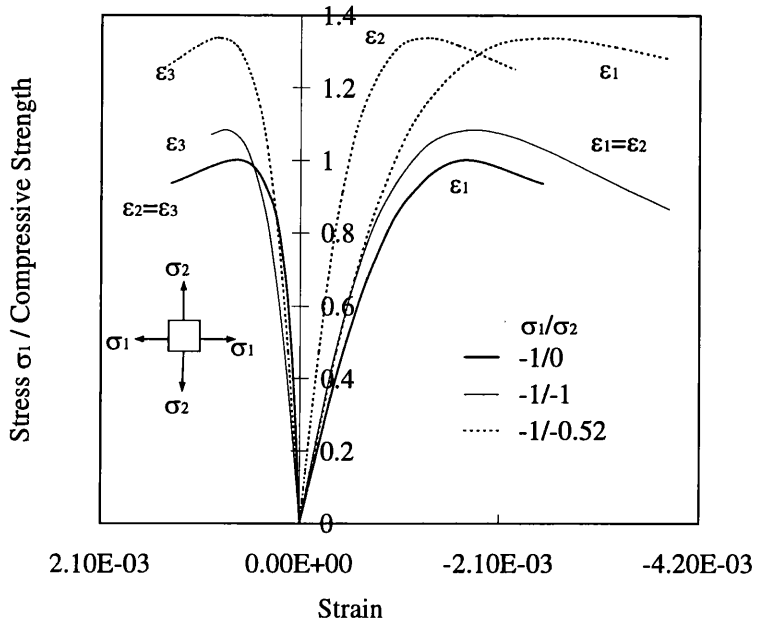

(a)

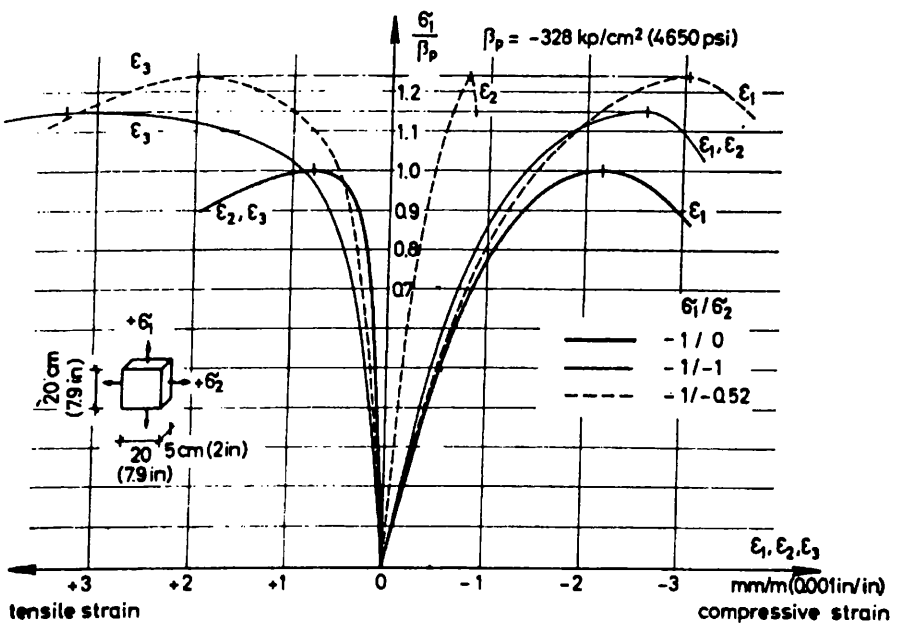

(b)

Figure 5.7: Stress-Strain Relationship under Biaxial Compression (a) Numerical Results from Model IV; (b) Experimental Results [10]

$\Rightarrow 9 \Rightarrow 10 \Rightarrow 0 \Rightarrow 11 \Rightarrow 0$

5.5 Discussion and Summary

Two new damage models are developed in this chapter, where different assumptions are proposed. Model III is based on a maximum principal strain postulate, i.e. the positive part of maximum principal strain governs tensile damage, whilst the negative part of the maximum principal strain dominates compressive damage. Model IV considers the different contribution of the hydrostatic and deviatoric components to damage. Since a weighted damage parameter is introduced, the computational complexity caused by separating strain/stress into positive and negative parts in existing models is overcome. The definition of the damage multiplier produces a satisfactory simulation of concrete behaviour under biaxial loading.

The implementation in finite element code of the two models is greatly

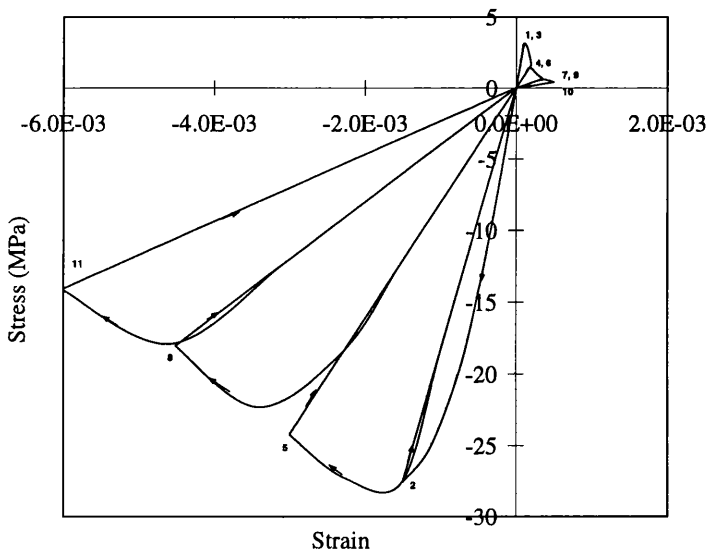

Figure 5.8: Response of Reverse Cyclic Loading from Model IV

simplified due to a description of potential energy in a strain space.

Although the phenomena of inelastic strain and crack closure are important features of concrete and further study is quite necessary, they are outside the scope of this thesis. The present models, however, are sufficient to simulate the matrix subjected to pull-out in fibre reinforced concrete, where tension and compression coexist in different places. In addition, further development of the models to include the inelastic response and crack closure should be fairly straightforward, although not without some difficulties.

Although the two models are developed from different concepts and assumptions, the comparison of the numerical analyses with the experiments demonstrates that they all can simulate the response of concrete subjected to uniaxial (models III and IV) and biaxial loading (model IV) very well. Finite element simulation with reverse cyclic loading also works well.

However, it is a fact that model IV is more powerful than model III. The main advantages of the former are that it is simple mathematically, does not require separating strain/stress due to introducing a weighted damage parameter, and can satisfactorily describe the behaviour of concrete under biaxial loading due to adopting a damage multiplier.

Chapter 6

Modelling Pull-Out

In steel fibre reinforced cement-based composites, since the ultimate strain capacity of the matrix is lower than that of fibre, the matrix fails before the full potential capacity of the fibre is achieved. In this case, the fibres which bridge the cracks formed in the matrix contribute to the energy dissipation through the processes of debonding and pull-out. The efficiency of this contribution is commonly assessed by the maximum crack bridging force (peak pull-out load) and the total energy absorption (pull-out work) during the fibre's pull-out.

Many factors affect the behaviour, including the properties of fibre, matrix and interface, fibre size, volume fraction, distribution, orientation, and geometry. However, in order to understand the entire response of a composite and to also develop a good pull-out model, a sound understanding of the contribution of a single perpendicular fibre and its pull-out mechanisms is essential. For this reason, section 6.1 will briefly describe the basic pull-out behaviour of a cement-based composite reinforced by a single perpendicular fibre.

As reviewed in Chapter 1 for existing finite element models of the pull-out problem, an interface is usually simulated by means of spring elements,

contact elements or specially developed elements in conjunction with a linear or non-linear stiffness. The direct application of interface elements is feasible for perpendicular fibres with small slip (usually less than 0.1 mm). For those composites with inclined, deformed or curved fibres, geometric constraints and Poisson's ratio will cause interaction and separation between fibre and matrix. Moreover, for a smooth short fibre, large sliding and full pull-out from matrix can occur after full debonding.

Considering only the change in the interface element stiffness, as in the existing models, is insufficient to describe this complex response. Therefore, a new and comprehensive pull-out model is required. In order to develop such a model which merges various pull-out mechanisms into one analytical model with little or no convergence problems in a non-linear analysis under large slip, many aspects have to be taken into account: (1) before debonding, the transmission of normal and shear stresses through the interface between fibre and matrix; (2) debonding criterion and debonding length; (3) after debonding, interfacial friction behaviour and interaction, and the large relative sliding of fibre against matrix; (4) matrix spalling and snubbing due to inclined fibre bending.

To deal with this, a novel modelling method is proposed in this chapter. A contact algorithm with friction, in conjunction with certain constraint conditions, is adopted to cope with the interaction and separation between fibre and matrix, and large relative sliding. The corresponding theory on contact with friction was outlined in Chapter 2.

To detect the onset and development of debonding in existing numerical models [77, 61], strength or fracture criteria were employed. In the strength-based methods, debonding was simulated by the shear failure of interface elements. In the fracture-based models, an initial crack length was first defined

and singular interface elements were placed at the interface crack front. The energy release rate was then calculated to decide whether debonding occurs or not. In the former, due to debonding, discontinuous and unstable computational results are often met, while in the latter the analysis has to be carried out for a series of meshed models with different crack lengths. An alternative consideration, where bonding and debonding are assumed as the constitutive properties of a given interface, is given in Section 6.2.

Since large relative sliding during pull-out can result in severe damage of the matrix (concrete), convergence difficulties often arise. In order to solve this problem at the beginning of this work, various attempts were made by employing different concrete models such as the smeared crack model etc. The results showed that using existing concrete models convergence was extremely difficult to achieve under relatively large sliding. This problem was also encountered by Leung and Chi [46], as described in Chapter 1. To overcome this, the strategy here regards matrix spalling and large deformation as a kind of material damage. Concrete damage models developed in Chapters 4 and 5 are adopted.

Another problem to be considered in modelling pull-out of inclined fibres is that when a fibre bends, snubbing and a substantial separation of the fibre occurs at its exit point. Its effect on pull-out behaviour is complex. Dealing with this will be described in Section 6.3. Finally, to evaluate the modelling accuracy, the sensitivity of various parameters is analyzed in the last section.

6.1 Pull-Out Characteristics of a Single Perpendicular Fibre

To analyse pull-out mechanisms of a single perpendicular fibre, we start with a typical bond force-slip relationship, i.e. the crack bridging force versus crack opening relation, Fig. 6.1. The curve can be subdivided into three stages. Stage 1 is controlled by elasticity, stage 2 by damage/fracture and stage 3 by friction. Fig. 6.2 illustrates the contribution of the bond force P_{bd} in the bonded zone and the frictional force P_{dd} in the debonded zone. Clearly, the total pull-out force P_t is simply given by

$$P_t = P_{bd} + P_{dd} \tag{6.1}$$

In Fig. 6.2, L denotes the bonded length before any debonding has occurred (i.e. the fibre length) and a denotes the debonded length; τ is the friction stress along the interface of the debonded zone; while g_T is the total slippage at the fibre exit point from the matrix and includes both the elastic and plastic slips.

We shall now derive a relationship between the pull-out force P_t and slip g_T during the complete pull-out process. In this context, the subscripts t, bd and dd donate total, bonded and debonded states respectively, and c, m and f represent composite, matrix and fibre respectively. The subscript numbers represent the stage number.

In stage one, we suppose the fibre and matrix are fully bonded (see Fig.6.3), so that force P_{t1} is completely transmitted from the fibre to the matrix through bond. According to St. Venant's principle, the average stress of the composite away from the load point can be written as

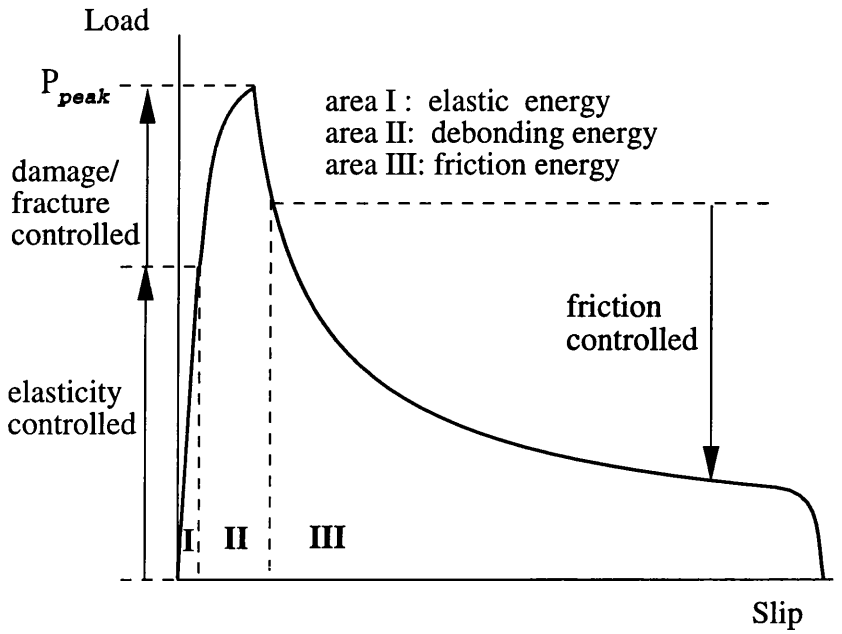

Figure 6.1: Typical Relationship of Bond Stress vs. Local Slip

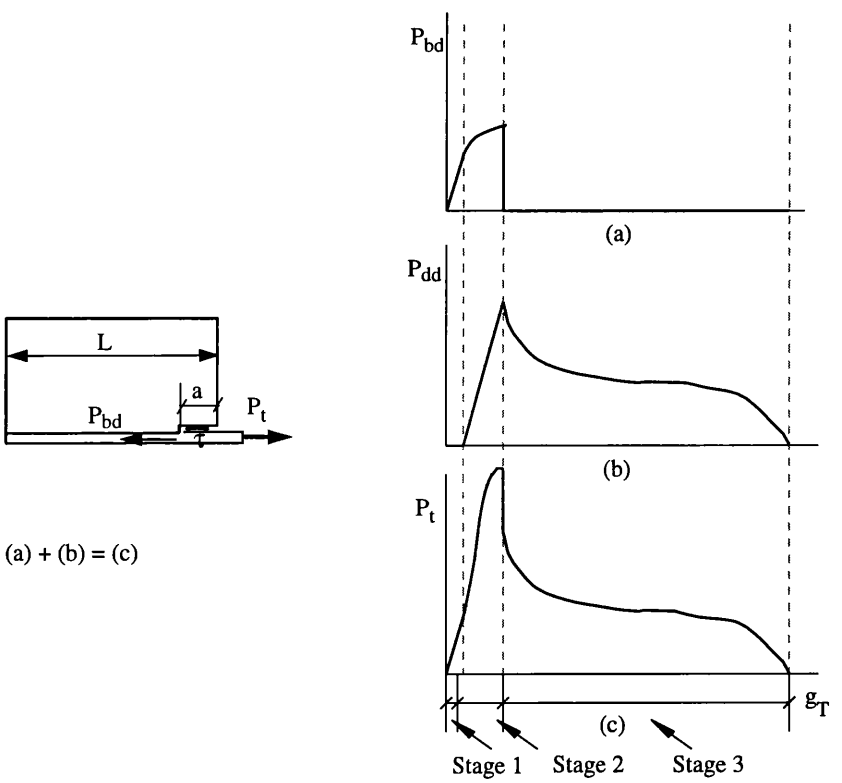

Figure 6.2: Relationship between Forces during Pullout

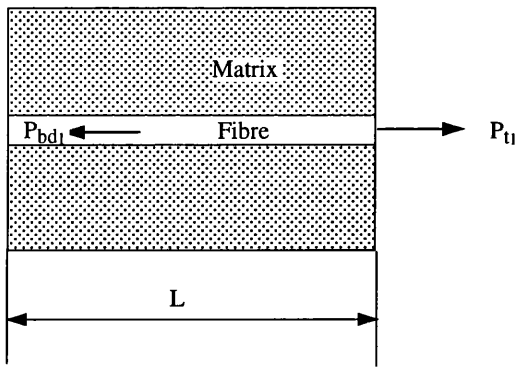

Figure 6.3: Fully Bonded Fibre

$$\sigma_c = \frac{P_{t1}}{A_c} = \frac{P_{bd1}}{A_c} = E_c \frac{g_T}{L} \tag{6.2}$$

where $A_c = A_m + A_f$ is the cross-section area of the composite, and $E_c = V_f E_f + (1 - V_f) E_m$ is the Young's modulus of the composite. V_f is the fibre volume fraction. From Eq. 6.2, the pull-out load P_{t1} can be written as

$$P_{t1} = P_{bd1} = E_c A_c \frac{g_T}{L} = \frac{K_c g_T}{L} \tag{6.3}$$

where $K_c = A_c E_c$ is the stiffness of the composite. During this stage, the friction force P_{dd1} is equal to zero because there is no debonding.

Beyond the elastic bond limit, debonding starts to occur (Fig. 6.4). A length a of the interface crack can be defined by a strength or fracture criterion. For the debonded part, the friction shear stress τ is assumed to be constant over a. Thus, the total friction force in the debonded zone is

$$P_{dd2} = \pi \phi a \tau \tag{6.4}$$

in which ϕ is the diameter of the fibre.

In stage two, regardless of the contribution of the debonded matrix, P_{bd2} is similar to that in stage one, that is

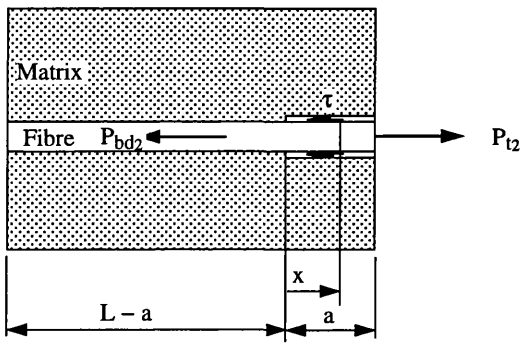

Figure 6.4: Fibre with Partial Debonding

$$P_{bd2} = \frac{K_c g_{Tbd}}{L-a} = \frac{K_c R_a g_{Tbd}}{a} \tag{6.5}$$

where g_{Tbd} is the deformation of the bonded part, and R_a is the ratio of the debonded length to bonded length. Combining Eqs. 6.4 and 6.5 and replacing a by x in Eq. 6.4, the total pull-out load at any cross section of the debonded zone is obtained as

$$\begin{aligned} P_{t2}(x) &= P_{bd2} + P_{dd2}(x) \\ &= \frac{K_c R_a g_{Tbd}}{a} + \pi\phi\tau x \end{aligned} \tag{6.6}$$

In order to relate the pull-out load P_{t2} to the total deformation g_T at the fibre exit point, consider an equilibrium of an infinitesimal free body in the debonded zone, as shown in Fig.6.5. To simplify the analysis, it is assumed that this infinitesimal segment is in uniaxial tension. Thus, the fibre stress σ_f at $x + \Delta x$ can be written in the following form,

$$\sigma_f(x+\Delta x) = \frac{P_{t2}(x) + \pi\phi\tau\Delta x}{A_f} = E_f \frac{\Delta g_{Tdd}}{\Delta x} \tag{6.7}$$

From Eq. 6.7 the total deformation g_{Tdd} in the debonded zone can then be derived as follows

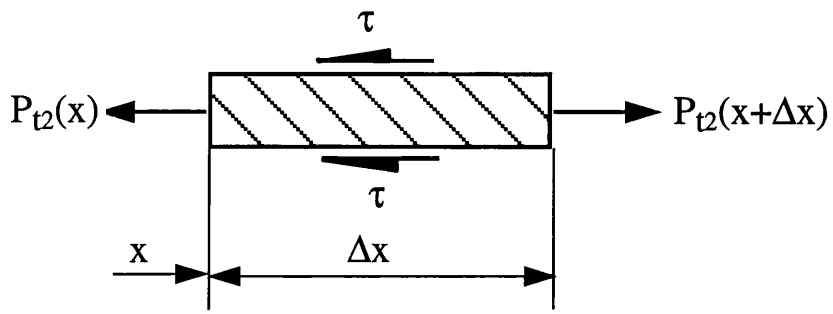

Figure 6.5: Free Body Diagram of Infinitesimal Segment of Fibre

$$g_{Tdd} = \int_0^a dg_{Tdd} = \frac{1}{E_f A_f} \int_0^a [P_{t2}(x)dx + \pi\phi\tau(dx)^2] \tag{6.8}$$

Ignoring the higher order term in the right-hand side of Eq. 6.8 and using Eq.6.6, Eq.6.8 becomes

$$\begin{aligned} g_{Tdd} &= \frac{1}{K_f} \int_0^a P_{t2}(x)dx \\ &= \frac{1}{K_f}(K_c R_a g_{Tbd} + \frac{\pi\phi\tau a^2}{2}) \end{aligned} \tag{6.9}$$

where $K_f = E_f A_f$ is the fibre stiffness. Since the total deformation g_T is the sum of the deformations in the bonded and debonded zones, we have

$$\begin{aligned} g_T &= g_{Tdd} + g_{Tbd} \\ &= \frac{R_a + R_K}{R_K} g_{Tbd} + \frac{\pi\phi\tau a^2}{2K_f} \end{aligned} \tag{6.10}$$

in which $R_K = K_f/K_C$ is the fibre relative stiffness. From Eq.6.10, g_{Tbd} can be easily derived as

$$g_{Tbd} = \frac{R_K}{R_a + R_K}(g_T - \frac{\pi\phi\tau a^2}{2D_f}) \tag{6.11}$$

Finally, substituting Eq. 6.11 into Eq. 6.6, the total pull-out load in stage two is obtained.

$$P_{t2} = \frac{K_f R_a}{a(R_a + R_K)} g_T + [1 - \frac{R_a}{2(R_a + R_K)}]\pi\phi\tau a \tag{6.12}$$

After the peak pull-out load is reached, the load drops until the fibre has fully debonded from the matrix. After this the bonding force P_{bd3} drops to zero and pullout is completely controlled by friction. During the third stage, the friction force at the interface is assumed to be uniform, any friction decay being ignored. Thus

$$P_{t3} = P_{dd3} = \pi\phi\tau L \tag{6.13}$$

Figs. 6.2 (a) and (b) illustrate the change of P_{bd} and P_{dd} with slip.

Based on the Eqs. 6.3, 6.12 and 6.13, and considering friction degradation, the relationship among the forces P_t, P_{bd} and P_{dd} is schematically presented in Fig. 6.2(c). It can be concluded that for a composite with given material properties and geometry, the pull-out response is mainly dominated by stage two and stage three. The former controls the peak crack bridging load, and depends primarily on the ratio of debonded length to bonded length, the debonded length and the residual interfacial friction force. The latter is an indicator of the softening process, and is only governed by the residual interfacial friction force associated with frictional degradation.

In addition, observing Fig. 6.1, we find that the pullout work of area I + area II required to overcome elastic deformation and to debond the interface is much less than that of area III caused by friction after full debonding. Since a primary purpose of adding fibres into a brittle matrix is to enhance its material toughness, and the pullout work is a measure of the material

toughness, the modelling of the frictional mechanism is of special importance in understanding and modelling pullout behaviour.

6.2 Basis of the Model

The bond stress-slip curve of a composite with a perpendicular fibre is a basic characteristic of its interfacial properties, whilst the interfacial behaviour is determined by the material properties of the matrix and fibre, interfacial chemical adhesion and the manufacturing technique. Once these are given, the interfacial properties are uniquely defined. In addition, the bond stress-slip relation also embodies information such as interfacial friction and transverse shrinkage etc. Therefore, we assume the bond stress-slip relationship of a composite with a perpendicular fibre as a local interfacial constitutive property. Based on this hypothesis, the bond shear stress at any point along the interface will depend on the relative slip at the same point.

Similar postulates can be found in the theoretical works of Naaman et al.[16] and Nammur and Naaman [4]. In ref. [4], a linear bond stress-slip relationship before debonding and a constant shear stress after debonding were assumed. In ref. [16], the degradation of shear stress after debonding was considered by means of the decrease of the misfit between matrix and fibre (introduced in Chapter 1).

To accurately describe interfacial bonding, debonding and friction degradation in this work, the bond stress-slip relationship is directly obtained by means of a curve fitted from the experimental relationship of crack bridging force versus crack opening for a perpendicular fibre. Based on experimental data, two curve fitting methods are employed, piecewise linear and piecewise regressions. The latter includes linear regression for stage one and power regression for stages two and three. Obviously, such a curve when applied to

a composite with randomly distributed fibres, requires additional considerations.

Based on the basic assumption that bond stress-slip relationship is a constitutive property of the interface, the magnitude of the pull-out load depends totally on the bond stress-slip relationship of each point along the fibre. In other words, it depends on the transmission of shear stress on the interface. Consequently, a contact algorithm with friction is adopted to simulate this transmission.

6.2.1 Definition of Contact Surfaces

For a contact problem, a contact pair for the interactive surfaces has first to be defined, i.e. a contactor and a target, sometimes called a slave surface and a master surface. For steel fibre reinforced concrete, the fibre side is chosen as the master surface and the concrete side as the slave surface.

Consider contact of a point x_s on a slave surface with a quadratic slide line segment (consisting of points x_1, x_2 and x_3) on a master surface (see Fig. 6.6). We can find such a point x on the segment so that it is closest to point x_s. Then, a contact element can be formed by points x_s and x, and the local normal N and tangential T vectors of point x can be determined. Obviously, the normal N is related to the contact gap g_N.

Since x is on a segment of the master surface, its position is completely defined by the interpolation function $N_i(\xi)$ of the segment. For a quadratic segment, we have

$$\begin{aligned} N_i &= \frac{1}{2}\xi\xi_i(1+\xi\xi_i) \quad i = 1, 3 \\ N_i &= 1-\xi^2 \quad i = 2 \end{aligned} \tag{6.14}$$

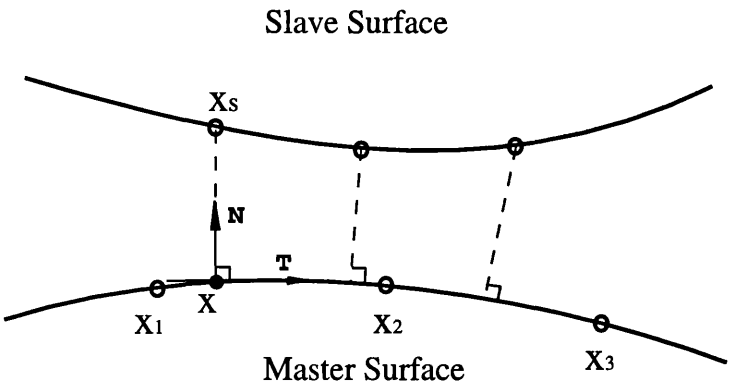

Figure 6.6: Quadratic Slide Line Segment

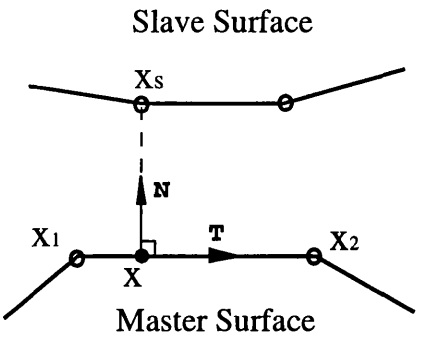

Figure 6.7: Linear Slid Line Segment

and for a linear segment (see Fig. 6.7)

$$N_1 = \frac{1}{2}(1-\xi)$$
$$N_2 = \frac{1}{2}(1+\xi) \tag{6.15}$$

To determine the position of point x, we define

$$\mathbf{N}g_N = \mathbf{x} - \mathbf{x_s} = N_i(\xi)\mathbf{x}_i \tag{6.16}$$

$$\mathbf{T} = \frac{d\mathbf{x}}{d\xi} / \left|\frac{d\mathbf{x}}{d\xi}\right| \tag{6.17}$$

where $dx/d\xi = (dN_i/d\xi)x_i$ and the other variables have been defined in Chapter 2. Obviously, the normal and tangential vectors must be orthogonal, i.e.

$$\mathbf{N} \cdot \mathbf{T} = N_i(\xi)\frac{dN_j(\xi)}{d\xi}\mathbf{x}_i \cdot \mathbf{x}_j = \mathbf{0} \tag{6.18}$$

From this equation, point x can be solved iteratively.

When contact occurs, the interaction is measured through the normal gap (separation) g_N and the tangential gap (slippage) g_T. Their computational expressions are given by Eqs. 2.3 and 2.4 in Chapter 2. The contact is controlled by g_N. Commonly, if $g_N > 0$, the two contact surfaces have no contact, and the contact algorithm is not considered. When $g_N \leq 0$ or $g_T > 0$, contact or slip occur respectively.

From a bond stress-slip curve we can see that after full debonding there is still a residual friction strength at the interface. However, with a basic contact algorithm, the transmission of interfacial forces will cease after debonding ($g_N > 0$). In fact, due to the effect of Poisson's ratio and fibre inclination etc. separation of interface is unavoidable during pull-out. To ensure that the bond stress-slip relationship is still workable under the separated situation, a normal constraint has to be enforced on the interface, and there must be no influence on the transmission of the tangential stress. This demands that firstly, the gap g_N must be kept to zero or within zero and an allowable value specified for the cases with large separation; secondly, the contact states, including sticking and sliding, are only determined by the tangential gap g_T. To realize the above conditions, different interfacial constraints are defined as follows.

6.2.2 Constraint Conditions and Implementation

Constraints in Normal Direction

Two normal constraint conditions are considered in the present model.

For a small clearance, the separation is mostly caused by transverse shrinkage of fibre due to the effect of Poisson's ratio. In this case, the normal gap $g_N = 0$ is defined. When the interface tends to separate, a negative pressure p_0 is enforced to constrain the contact surfaces together. The constraint condition (hard contact) can be expressed as

$$\boxed{\begin{aligned} &g_N \geq 0 \\ &t_N \leq p_0 A_{con} \\ &g_N t_N = 0 \end{aligned}} \tag{6.19}$$

where A_{con} is area of a contact element, and the constraint is schematically presented in Fig. 6.8.

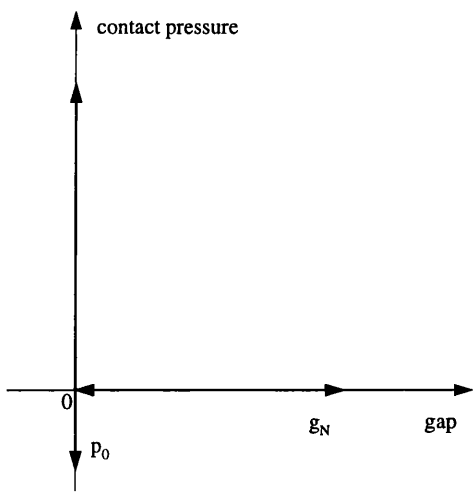

Figure 6.8: Contact Pressure-Gap Relationship

For a large clearance, separation mainly stems from reinforcement geo-

metry and matrix constraint, such as the case of a curved bar in reinforced concrete. With large separation, a tensile stress enforced at the interface is not enough to prevent the interface opening. An alternative constraint approach is to allow the interface to sustain a certain separation g_0, and the normal load-transmitting capability to decrease exponentially with the separation. This ensures that the tangent load transmits continuously until the given value g_0 is achieved. This exponential pressure-gap relationship (soft contact) [135] is

$$\begin{array}{lll} t_N = 0 & for & g_N \geq g_0 \\ t_N = -\frac{p_0 A_{con}}{e-1}[(1-\frac{g_N}{g_0})(e^{(1-\frac{g_N}{g_0})}-1)] & for & -6g_0 \leq g_N < g_0 \\ t_N = -\frac{p_0 A_{con}}{e-1}[7e^7 - 1 - (6+\frac{g_N}{g_0})(8e^7-1)] & for & g_N < -6g_0 \end{array} \tag{6.20}$$

and is illustrated diagrammatically in Fig. 6.9.

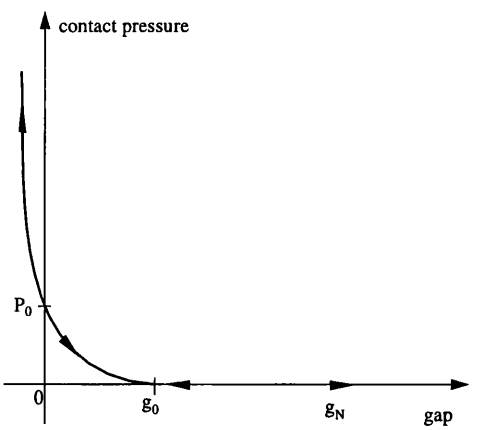

Figure 6.9: Exponential Pressure-Gap Relationship

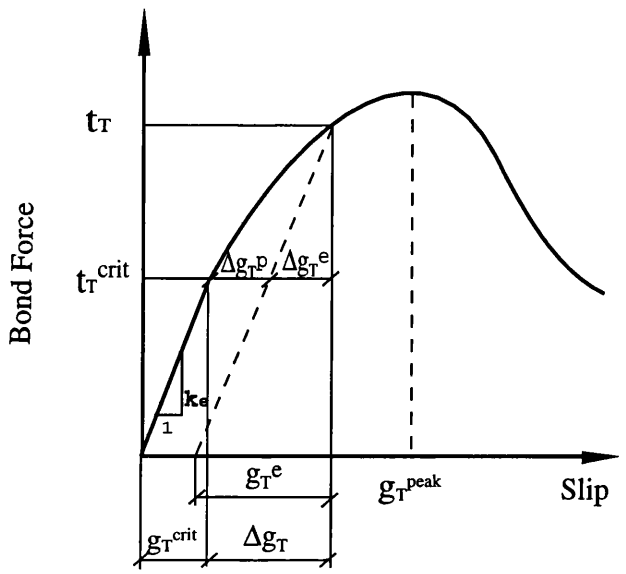

Figure 6.10: Assumed Bond Force vs. Slip Relationship

Constraints in Tangential Direction

During a sticking contact, only elastic tangential slip exists. The shear force and relative slip on the interface yield the following relation before a critical slippage g_T^{crit} is attained.

$$t_T = k_e g_T \tag{6.21}$$

where k_e is the bond modulus in the linear-elastic portion of a bond force-slip curve (see Fig. 6.10).

When the slippage g_T exceeds the critical value g_T^{crit}, the slip is accompanied by an unrecoverable relative motion. The total slip g_T is the sum of the elastic slip and the unrecoverable relative motion, i.e.

$$g_T = g_T^{crit} + \Delta g_T = g_T^{crit} + \Delta g_T^e + \Delta g_T^p \tag{6.22}$$

Depending on the adopted bond stress-slip curve, the constraints are then given as follows:

$$\boxed{t_T = k_{ei} g_T \qquad i = 1, 2, \ldots} \tag{6.23}$$

or

$$\boxed{\begin{array}{lll} t_T = k_e g_T & for & g_T \leq g_T^{crit} \\ t_T = a_1 g_T^{b_1} & for & g_T^{crit} < g_T \leq g_T^{peak} \\ t_T = a_2 g_T^{b_2} & for & g_T > g_T^{peak} \end{array}} \tag{6.24}$$

with

$$\boxed{\begin{array}{l} f = t_T \leq 0 \\ \dot{g}_T \geq 0 \\ f \dot{g}_T = 0 \end{array}} \tag{6.25}$$

where $a_1, a_2, b_1 \, and \, b_2$ are regression coefficients, and g_T^{peak} is the slip corresponding to the peak load point. f and $\dot{g}_T$ have been defined in Chapter 2.

With these constraints, the modelling of pull-out can be conducted. The constraints in the normal direction for the case with small separation and in the tangent direction are implemented by the penalty method. The augmented Lagrangian technique is employed to deal with the case with large separation.

The non-linear finite element code ABAQUS [135] was used for implementing the contact algorithm in conjunction with new developed code for dealing with the constraints in the tangential direction and for modelling some special pull-out mechanisms, such as snubbing etc.

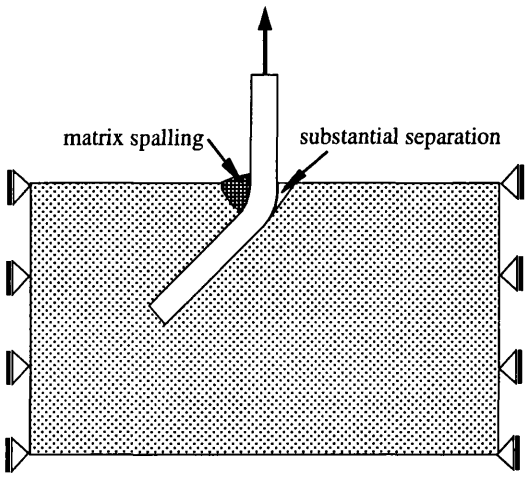

Figure 6.11: Illustration of Matrix Spalling and Substantial Separation

6.3 Modelling of Other Pull-Out Mechanisms

In addition to the mechanisms discussed previously, a composite with randomly distributed fibres will suffer local snubbing and substantial separation at the fibre exit point from the matrix due to fibre bending, as sketched in Fig. 6.11.

Snubbing

To cover the effect of snubbing, a Coulomb friction law is used to measure its contribution to the interfacial shear force in the form

$$t_T^{snub} = \mu p A_{con} \tag{6.26}$$

where μ is a friction coefficient, and p is the contact pressure inducing local friction. The extra shear force is added to the total interfacial shear force during each loading increment.

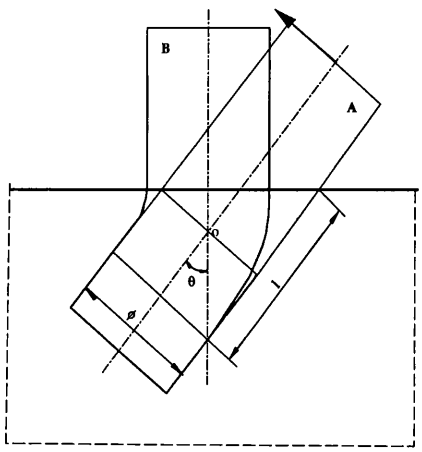

Figure 6.12: Determination of Substantial Separation Length

Substantial Separation

A substantial separation at the fibre exit accompanies matrix spalling. The same method is adopted for its simulation as in the soft contact model. The differences are: an individual contact pair has first to be defined within an estimated separated length l; then a pressure p_0 with the same magnitude as the bond strength ($2.0MPa$ in the present analyses) constrains the interface. When the normal force on the interface exceeds its ultimate tensile bond capacity, the interface opens, which results in the matrix spalling on the other side of interface.

Assuming, in Fig. 6.12, the fibre is bent from a position A to B around point "o", the opening length can be approximated by

$$l = \phi(\tan\theta + \frac{1}{2\tan\theta}) \tag{6.27}$$

in which θ is the inclined angle of the fibre, and ϕ is the fibre diameter.

6.4 Validation of 2-D Model

Because a fibre is surrounded by the matrix, pull-out behaviour is essentially three dimensional. Existing two dimensional pull-out modelling do not fully describe an actual three dimensional situation. Some methods have been used for solving this problem, such as axisymmetric models [78], or two-dimensional multiplane finite element meshes [61]. These approaches are practical for a perpendicular fibre. However difficulties arise for randomly distributed fibres. Three dimensional interface modelling is very complex, and requires excessive computer time and storage.

The introduction of contact algorithms with friction in the present model makes the substitution of 2-D for 3-D possible. A friction contact area A_{con} for each contact element is defined as

$$A_{con} = \frac{\pi\phi}{2} L_{con} \tag{6.28}$$

where L_{con} is the length of contact element. By this, the transverse effect of matrix on fibre is applied to the whole perimeter of the fibre.

This approximation is assessed by means of a pull-out numerical model with a perpendicular fibre. A two dimensional plane strain model and an axisymmetric model are used (Fig.6.13) respectively. The same material properties and constraint conditions are defined.

In the two dimensional plane model, 8-node quadratic plane strain quadrilateral elements are used for the fibre, and 6-node quadratic plane strain triangle elements for the matrix. For the axisymmetric model, both matrix and fibre are meshed with 8-node quadratic axisymmetric quadrilateral elements. The results are compared in Fig. 6.14 and very close agreement is obtained.

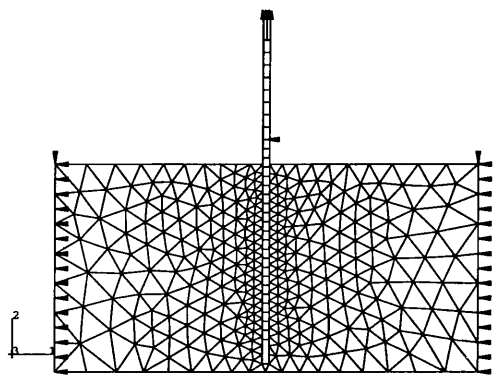

(a)

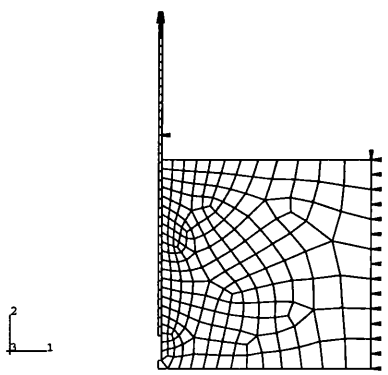

(b)

Figure 6.13: Configurations of Pull-Out Models: (a) Two Dimensional Plane Model; (b) Axisymmetric Model

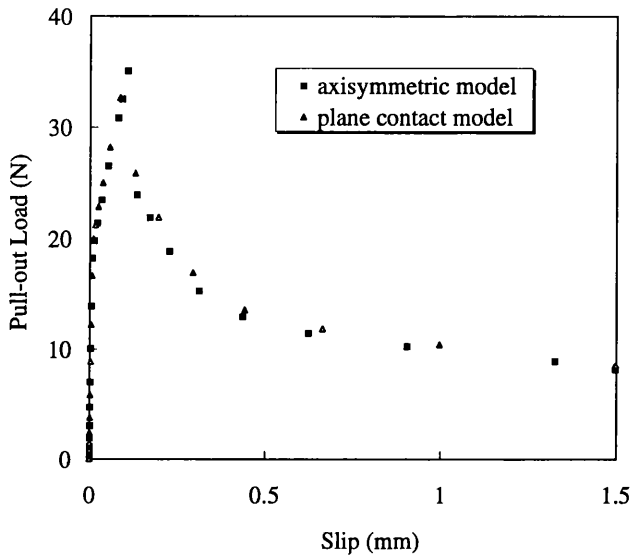

Figure 6.14: Comparison of Results of Two Models

Using the same model, the capability of modelling full pull-out is examined. Figs. 6.15 and 6.16 are evidence that it works well and has a similar configuration with the experimental curve [11].

6.5 Choice of Model Parameters

Many factors could influence the numerical results, such as the structural constraints, interfacial constraints, the magnitude of the loading increment, element size, the coefficient of friction, and the separating length at the fibre exit. For this reason, the choice of various parameters are discussed in the following. All analyses are performed using the same 2-D plane model with a fibre inclined at 45^0.

Structural Constraints

Several different constraints are depicted in Fig. 6.17: (a) at the two sides of the matrix; (b) at the top of the matrix, but close to the fibre; and (c) at the

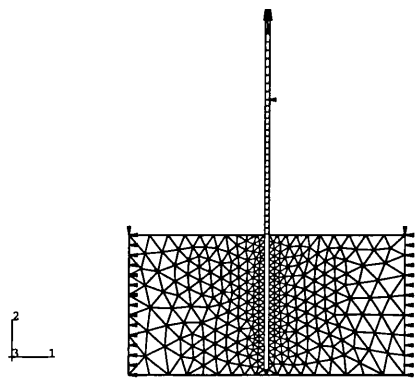

Figure 6.15: Configuration after Full Pull-Out

top of the matrix, but a little distance from the fibre.

The influence of structural constraints on pull-out responses are plotted in Fig. 6.18. The results indicate that for the top constraints, different constraint lengths lead to different pull-out responses. Full constraint (case b) limits the deformation of matrix and causes an increase of the pull-out load. Insufficient constraint (case c) results in convergence problems of non-linear solution. In fact, the crack surface is stress free. Therefore, the lateral constraint (case a) is more reasonable for a pull-out experiment and numerical analysis.

Interface Constraints

Four different contact pressures for the hard contact model were tested, i.e. 10 MPa, 100 MPa, 1000 MPa and 10000 MPa (see Fig. 6.19). The deformed configurations are shown in Figs. 6.20 to 6.23. For the very small contact pressure, $p_0 = 10$ MPa, an interfacial crack initiates prematurely and propag-

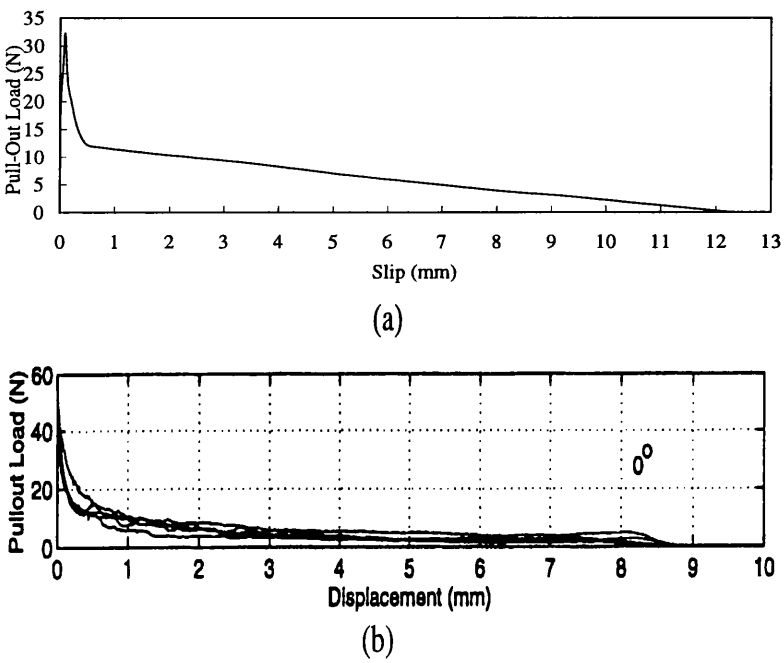

Figure 6.16: Full Pull-Out Responses: (a) Numerical Result; (b) Experimental Result [11]

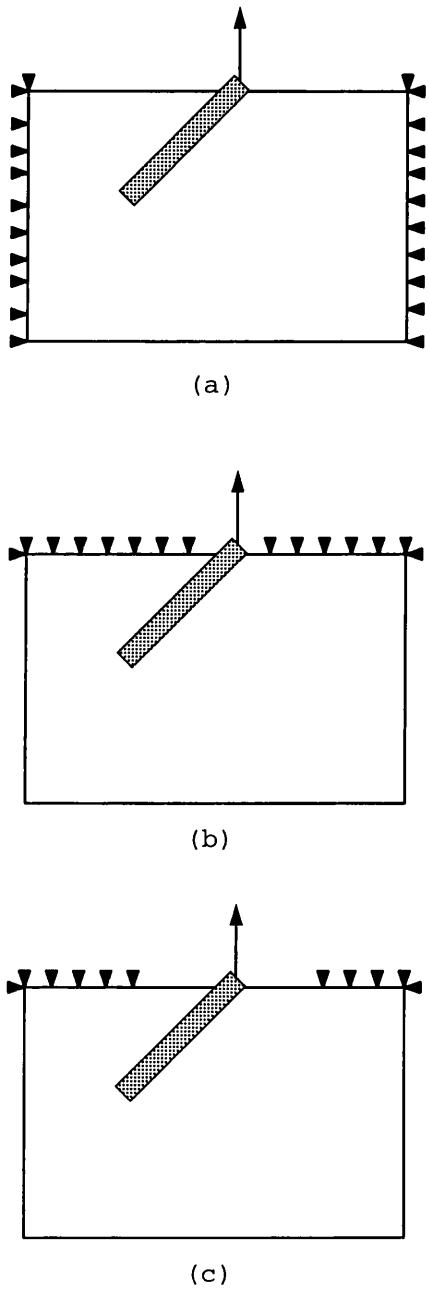

Figure 6.17: Different Structural Constraints

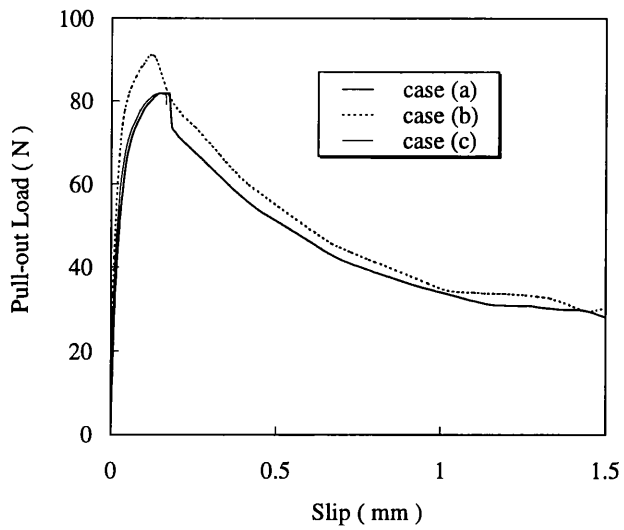

Figure 6.18: Effect of Different Structural Constraints on Pull-Out Response

ates rapidly passing over the whole fibre length along one side of the fibre (Fig. 6.20), leading to the collapse of the computational system. The phenomenon can also be explained by tensile principal stress contours, Fig. 6.24, and vector plots, Fig. 6.25, under four different loading increments. These contours and vector plots describe the propagation process of the interfacial crack from the active to passive ends of the fibre through the transmission of tensile principal stress along the interfaces. Fig. 6.19 shows that to obtain a insensitive numerical result, any value of p_0 over 1000 MPa can be adopted.

Initial Loading Increment

To describe the softening stage of the pull-out response, displacement loading has to be adopted in a finite element analysis. The total expected displacement is loaded by a series of increments. The term "increment" is defined as the ratio of the current loaded displacement to the total expected displacement.

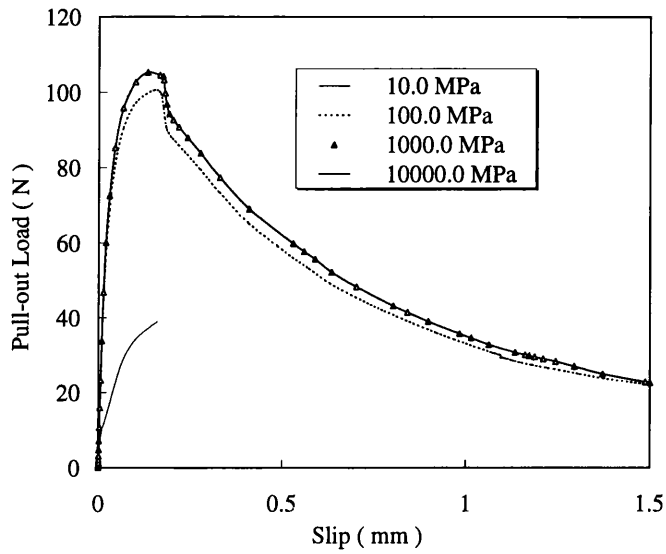

Figure 6.19: Effect of Constraint Pressure on Pull-Out Response

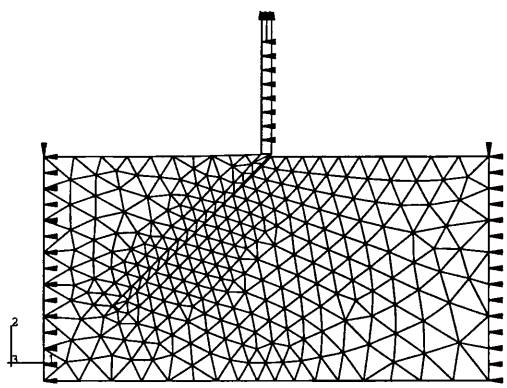

Figure 6.20: Deformed Configuration for $p_0 = 10$ MPa

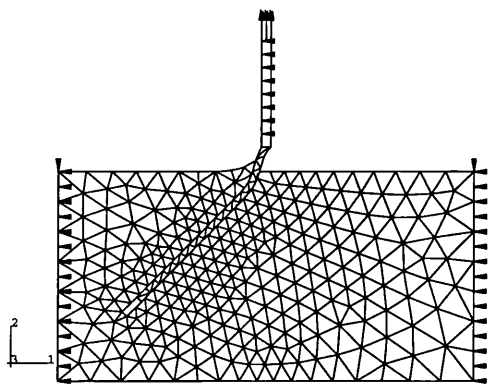

Figure 6.21: Deformed Configuration for $p_0 = 100$ MPa

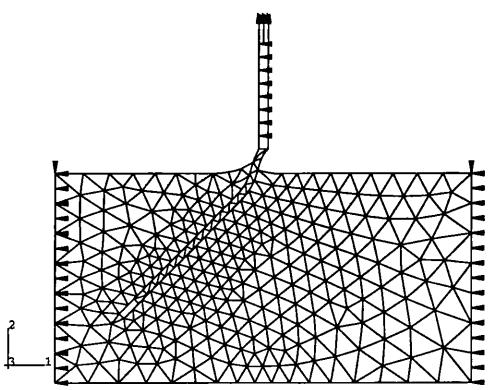

Figure 6.22: Deformed Configuration for $p_0 = 1000$ MPa

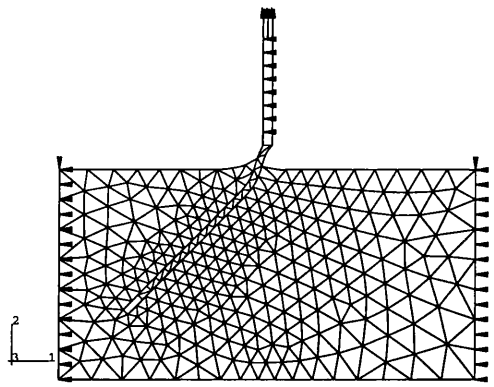

Figure 6.23: Deformed Configuration for $p_0 = 10000$ MPa

Obviously, too small an initial increment will increase computational time, and be prone to diverge at the discontinuities of a piecewise fitted bond stress-slip curve due to a discontinuous first derivative. For a large initial increment it may be difficult to reach an equilibrium solution.

Several initial increments are evaluated, from 0.0001 to 0.01. Among the chosen range, none influenced the pull-out response (Fig. 6.26). Each increment is generally convergence after four to five iterations. The increase of initial increment is accompanied by a decrease of the total number of increments to complete an analysis (Fig. 6.27).

Generally, to ensure modelling accuracy around the discontinuities of a piecewise fitted bond stress-slip curve, 0.0001 is first chosen. If convergence problem occurs, this can be overcome by increasing the increment to 0.001 so that the discontinuity causing trouble is by-passed.

In the following analyses, an initial increment between 0.0001 to 0.001 is

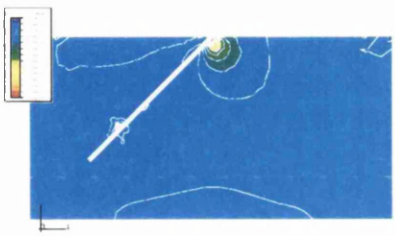

Increment No.= 10

Increment No.= 14

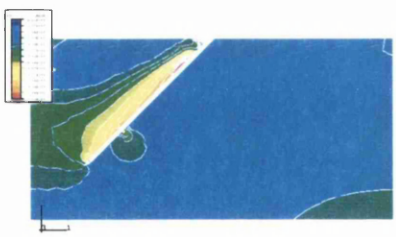

Increment No.= 18

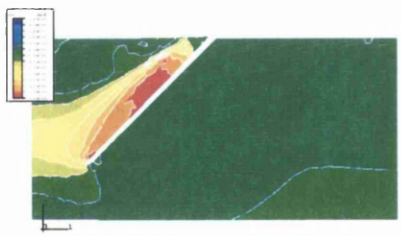

Increment No.= 41

Figure 6.24: Tensile Principal Stress Contours

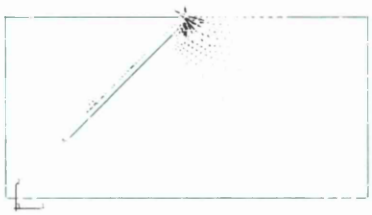

Increment No.= 10

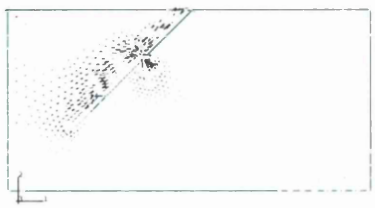

Increment No.= 14

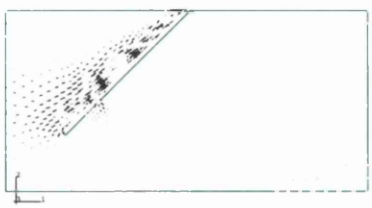

Increment No.= 18

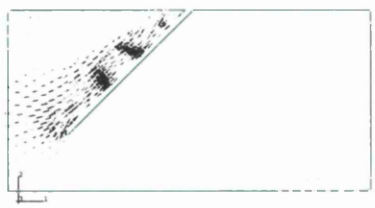

Increment No.= 41

Figure 6.25: Tensile Principal Stress Vectors

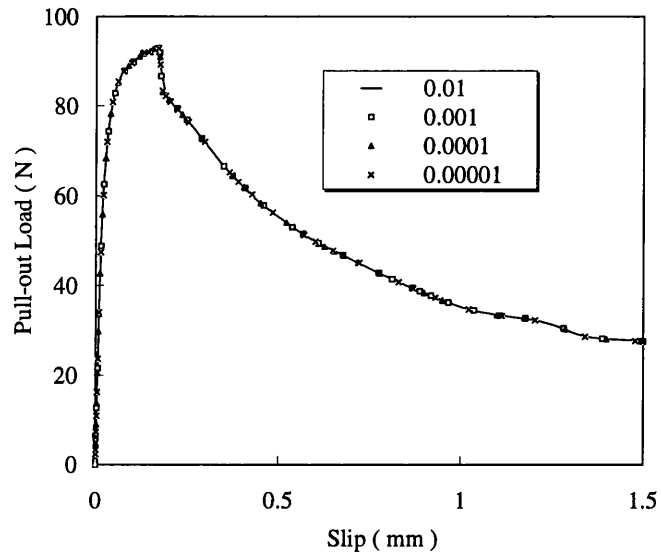

Figure 6.26: Effect of Initial Loading Increment

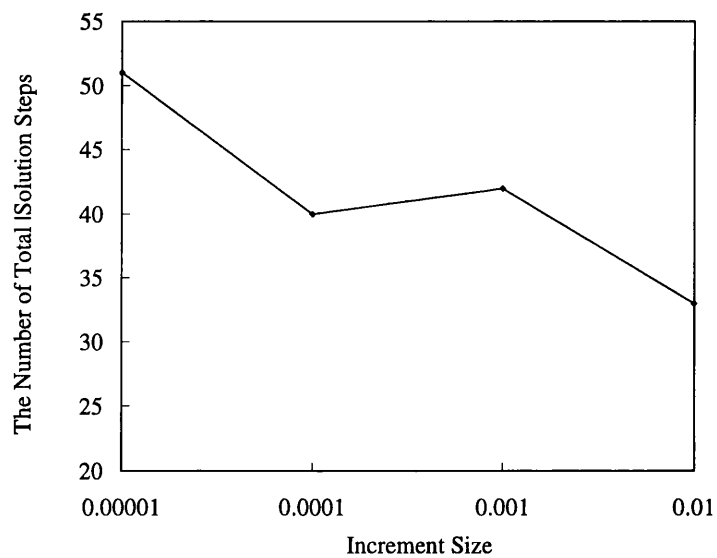

Figure 6.27: Relationship of the Number of Total Solution Steps vs. Increment Size

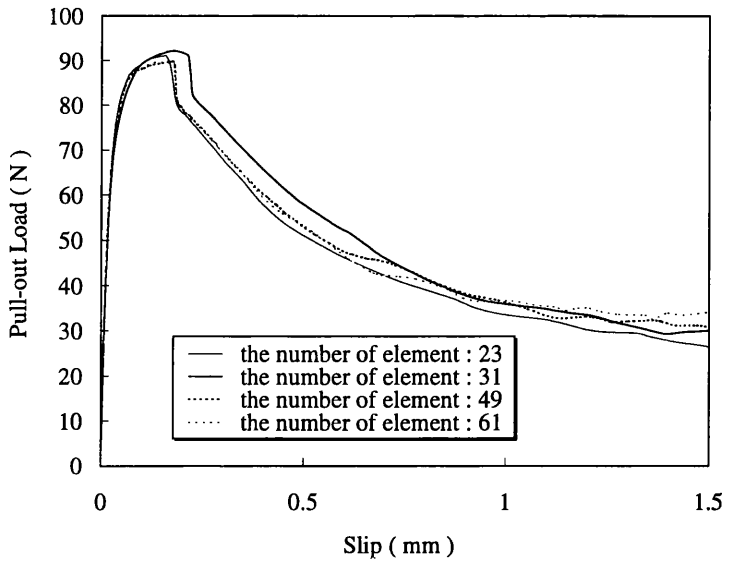

Figure 6.28: Pull-Out Response for Fibre with Triangle Elements

chosen.

Mesh Sensitivity

The simulation of contact with friction in the present model is a key point. So it is necessary to establish whether the pull-out response is affected by the size and shape of elements of the master and slave surfaces.

To illustrate this, the fibre and matrix are meshed using different numbers of elements respectively. The matrix is meshed with triangular elements. Since the fibre suffers large geometric non-linearity under bending, both triangular and quadrilateral elements are tested respectively. The effects of the number of elements on pull-out responses are depicted in Fig. 6.28 for the fibre with triangular elements, Fig. 6.29 for the fibre with quadrilateral elements and Fig. 6.30 for the matrix.

Generally, a change in the number of elements causes a change in peak pull-out loads, but has little influence on the total energy dissipation of pull-

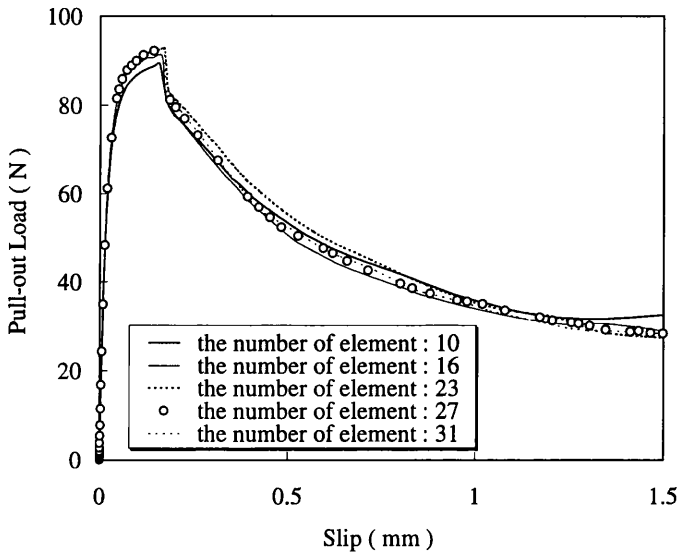

Figure 6.29: Pull-Out Response for Fibre with Quadrilateral Elements

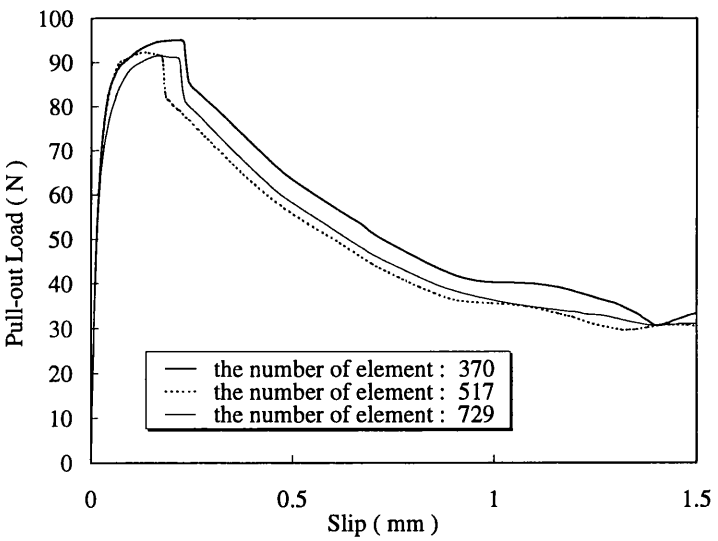

Figure 6.30: Pull-Out Response for Matrix with Quadrilateral Elements

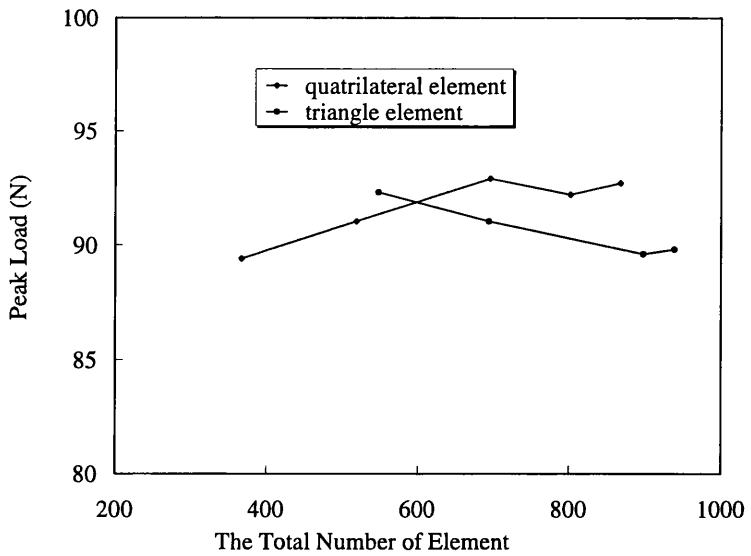

Figure 6.31: Relationship of the Total Number of Element vs. Peak Load

out. For the fibres meshed with triangular elements, a small change in pull-out peak load can be observed, but this stabilizes after 49 elements. With quadrilateral elements the peak load changes within a small range, but the displacements under the peak loads are basically a constant. A stable solution is found after 16 elements.

As for the matrix, the different number of elements exhibit different peak loads and pull-out work (see Fig. 6.30), but the results tend to stabilize after a large number of elements.

To take account of the general influence of fibre and matrix, the relationship of peak load versus the total number of elements is illustrated in Fig. 6.31, in which the fibre has been meshed with two element types. For both element types, a stable peak load is obtained after the total number of elements is about 800. However, between the two element types, peak loads have a relative error around 3.4%. Actually, the experimental evidence from refs. [12, 11] indicated that the experimental scatter of peak load was

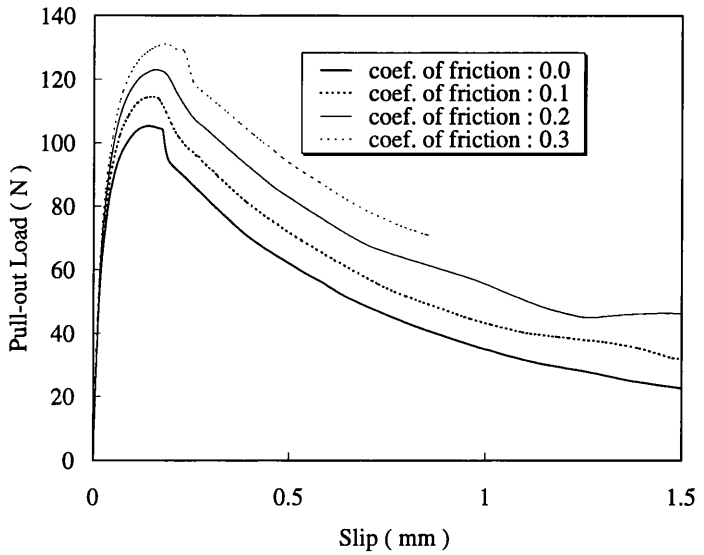

Figure 6.32: Effect of Friction Coefficient on Pull-Out Response

from about 10% to 50%. Therefore, the analytical error is acceptable from an engineering point of view.

From the preceding analyses, it can be concluded that sufficiently large number of elements for fibre and matrix is necessary to ensure modelling accuracy.

Coefficient of Friction

As interpreted earlier in Section 6.3, the effect of snubbing depends on the coefficient of friction. Figs. 6.32 and 6.33 illustrate the effect of the coefficient of friction on the pull-out response, where the normalised peak load is defined as the ratio of the current peak load to that with a perpendicular fibre. The results indicate that the increase of friction coefficient not only increases the peak load, but also the total pull-out work. However, the magnitude of the friction coefficient in the analysis can be determined by simulating the experimental data.

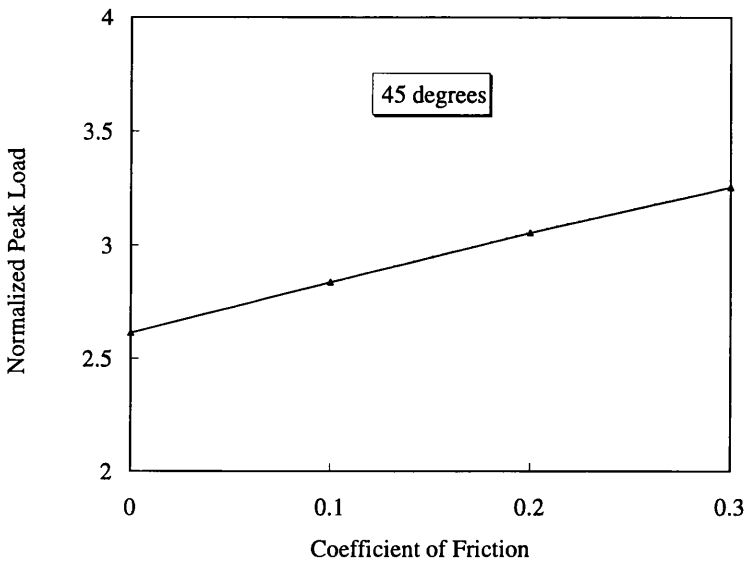

Figure 6.33: Effect of Friction Coefficient on Peak Load

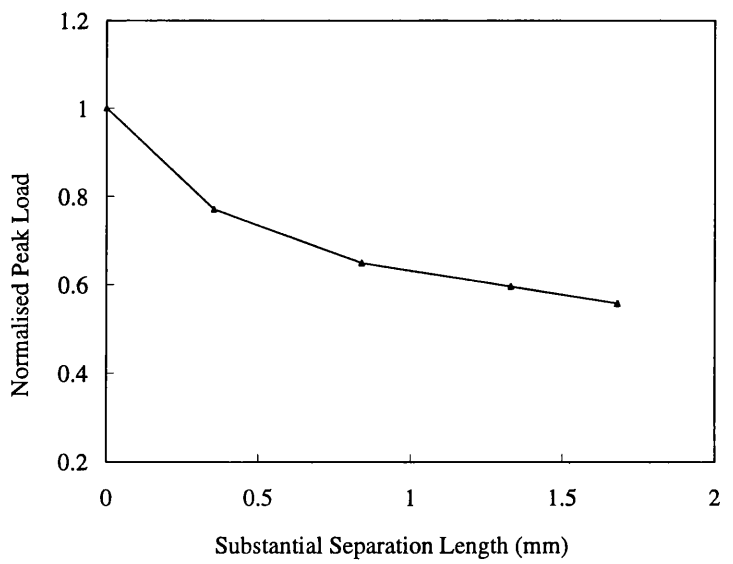

Figure 6.34: Effect of Substantial Separation Length on Peak Load

Substantial Separation Length at Exit Point of Fibre

The substantial separation at the fibre exit will reduce the contact length of the interface and increase the degree of snubbing and spalling. To evaluate this effect, different separation lengths are tested. The results (see Fig. 6.34) show that the separation length has a large influence on the peak pull-out load.

Since the length is affected by many factors, such as fibre and matrix properties etc., how to determine its magnitude is still an open question. Further research including experiment and theory is needed.

6.6 Summary

A pull-out modelling method was proposed in this chapter. With the model, pull-out response with inclined or curved reinforcement can be simulated, and the modelling of large sliding and full pull-out can be achieved.

The different features of the present model from other existing finite element models are:

1. a local bond stress-slip curve fitted from a pull-out experiment with a perpendicular fibre was used to describe the whole process of bonding, debonding, bond degradation and pull-out, with no requirement for an additional strength or fracture criterion;

2. the contact algorithms with friction were introduced to deal with the interaction between contact surfaces;

3. matrix spalling is automatically simulated by means of the concrete damage model;

4. snubbing and the substantial separation at fibre exit are capable of being modeled.

In addition, the use of a two-dimensional model was verified.

The sensitivity analysis of the various parameters indicated that the choice of structural and interfacial constraints influences the numerical results. Lateral structural constraint is recommended for both experiment and analysis. An interfacial constraint large enough to ensure a consistent result is needed for hard contact model.

Due to geometrical non-linearity and load concentration in the vicinity of the fibre exit point from matrix, a sufficiently large number of elements for the fibre and matrix are necessary. Finally the coefficient of friction and the separation length at the fibre exit has a significant influence.

Chapter 7

Pull-out Response of Inclined Fibres

The pull-out mechanisms of a cementitious composite with a fibre perpendicular to crack has been presented in Chapters 1 and 4. Its numerical modelling is relatively straightforward. However, in reality, fibres in a cementitious composite are distributed in a quasi-random manner. Consequently, fibres bridging matrix cracks are generally inclined at an angle to the cracks (see Fig. 7.1).

Inclined fibres subjected to a pull-out load behave differently from perpendicular fibres. Pull-out results from a perpendicular fibre may not be representative of crack bridging behaviour in a composite [11]. In the latter, bridging forces are mainly balanced by debonding mechanisms such as shear friction and cohesive forces. Inclined fibres, however, are also subject to bending mechanisms [49, 12]. These include bending and yielding of the fibre as it exits from the matrix accompanied by snubbing [18], matrix spalling [32, 19, 46] and a substantial separation of the fibre in the vicinity of the fibre exit (Fig. 7.2). Brittle fibres can also break during pull-out.

Several experimental studies of the influence of fibre inclination on pull-out behaviour have been carried out. Pull-out tests of inclined fibres are

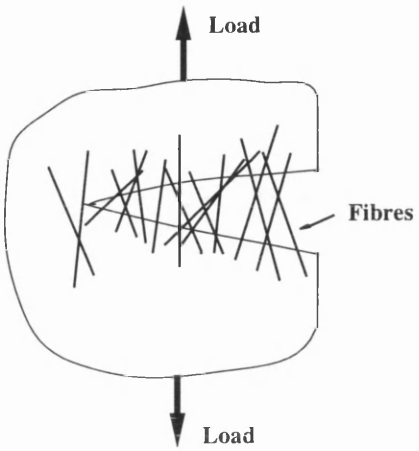

Figure 7.1: Schematic Drawing of Fibres Bridging a Crack

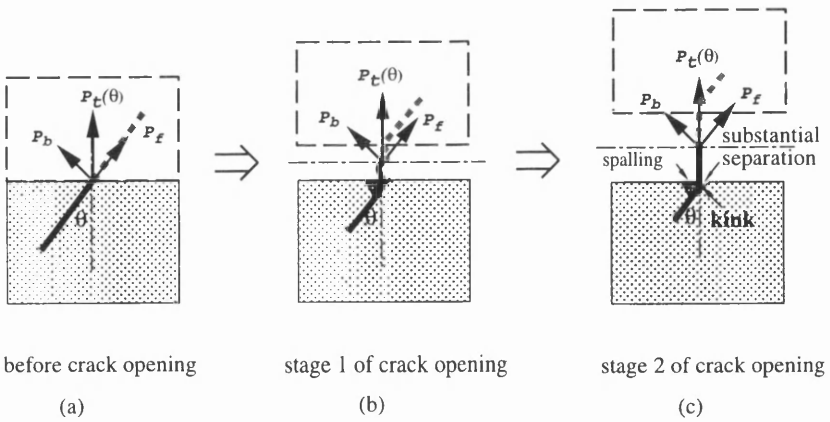

Figure 7.2: Crack Bridging Forces during Pullout

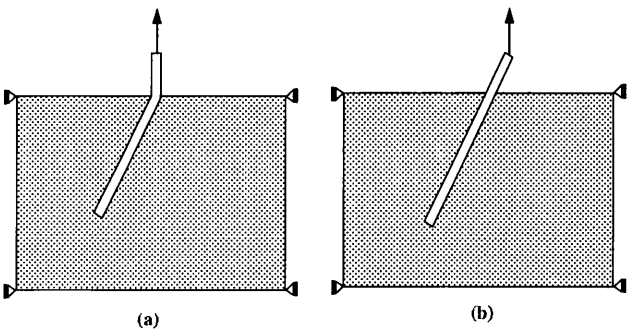

Figure 7.3: Configurations of Pull-out Specimens with: (a) Initially Bent Fibre; (b) Initially Straight Fibre

usually performed using two types of specimen (see Fig. 7.3), one with an initially bent fibre and the other with an initially straight fibre. Using the former specimen, Naaman and Shah [13], and Ouyang et. al. [12] found that the work required to fully pull out inclined steel fibres is larger than that of perpendicular fibres and that the final pull-out load just before the fibre is pulled out of the matrix increases with inclination. This implies that an inclined fibre has a higher residual frictional resistance against sliding.

Leung and Ybanez [136] tested flexible fibres which were either initially straight or initially bent at their exit from the matrix. Significant differences in the pull-out behaviour of the two types were observed. With initially bent fibres, both the peak pull-out load and pull-out work increased with inclination and were significantly higher than those with initially straight fibres, especially when the inclined angle is beyond 45^o. Consequently, they considered that the use of initially bent fibres in pull-out specimens could overestimate crack bridging effectiveness of flexible fibre.

In order to clarify the influence of different specimens and fibre inclination in SFRC on pull-out response, numerical analyses are conducted in this chapter with initially straight and initially bent fibres respectively. These ana-

lyses are also used to further verify the proposed models. The results with the initially bent fibres are compared with the experiments of Ouyang et. al. [12], whilst those with initially straight fibres are checked against those of Naaman and Shah [13], and Leung and Shapiro [11]. The difference between specimens is distinguished and finally the bending mechanisms of inclined fibres are studied.

For concrete reinforced by randomly distributed fibres, another interesting issue to study is the interaction between multiple fibres. Its investigation is of assistance in optimising the distribution of fibres in concrete.

Mandel et al [61] studied the effect of fibre spacing on the interfacial bond strength for perpendicular fibres. In their experiments, fibre spacing of 10ϕ, 12.5ϕ, 16.5ϕ, and 25ϕ (where ϕ denotes the fibre diameter) were used. The results shown that fibre spacing had little effect on the average bond stress per fibre.

To investigate the effect of fibre spacing for inclined fibres with different layouts, numerical analyses of the pull-out of two fibres are also carried out. Finally the interaction between fibres is discussed.

7.1 Modelling Approach

The two dimensional finite element analysis model presented in Chapter 4 is used. Concrete is meshed with 6-node quadratic plane strain elements. Both 6-node and 8-node quadratic plane strain elements are used for fibres respectively.

The Von Mises yield criterion is adopted to characterize the behaviour of steel fibre using a uniaxial yield strength of 347 MPa. The matrix is described either using damage model IV with uniaxial ultimate strength of 34.8 MPa or using a Drucker-Prager yield criterion with material cohesion of 38.1 MPa

and friction angle of material of 18.8^0. Young's modulus and Poisson's ratio are respectively 210 GPa and 0.3 for the fibre, and 23.7 GPa and 0.15 for the matrix. These parameters are based on the common properties of concrete.

For simulating the interface, the contact algorithm with friction introduced in Chapters 2 and 4 is used. A constraint with the hard contact pressure-gap relationship as described in Fig. 6.8 is imposed in the normal direction of the interface with $p_0 = 1000.0$ MPa. The local interfacial bond-slip relationship was obtained by retrofitting the experimental data [12] of a perpendicular fibre, and is employed directly as the tangential constraint. As previously stated, this relationship is assumed to be an inherent macroscopic property of the fibre interface, so that it is applicable for the cases with inclined fibres. The experience from numerical tests indicated that the bond-slip relationship significantly influences the pull-out behaviour of a composite, especially around peak load point. Consequently, it is important that this relationship is accurately defined by sufficient data.

When local snubbing happens during pull-out, Eq.6.26 is used to calculate the contribution of local friction to interfacial shear stress with a coefficient of friction of 0.1.

Analyses indicated that the length of separation at the fibre exit can greatly influence the analytical results. However, this effect mainly reduces the magnitude of pull-out load, and should not change the pull-out mechanisms. On the other hand, since no matrix spalling or separation was actually observed in Ouyang et. al.'s experiments[12], the effect of this separation is omitted in the following analyses. In doing so, the results from numerical analyses are easier to understand and explain.

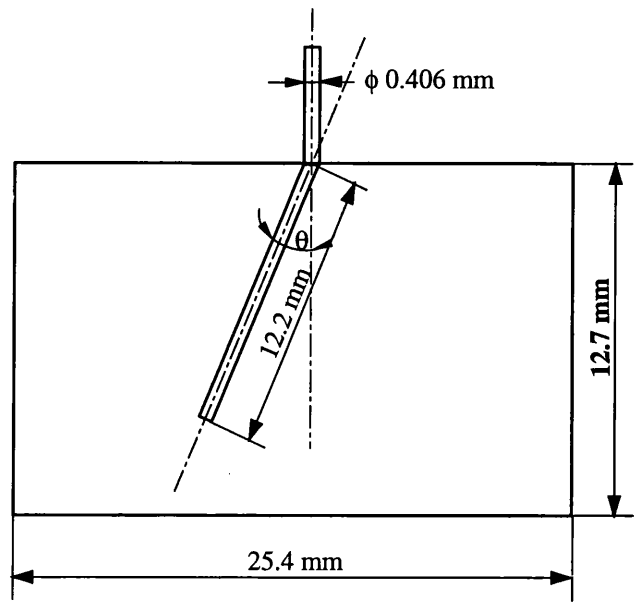

Figure 7.4: Dimension of Specimen for Numerical Modeling

7.2 Pull-out of a Single fibre

The modelling of pull-out for a single fibre is first conducted for initially bent fibres.

To compare the numerical solution against experiment, the model is designed with the same specimen dimensions as in ref. [12], but averaged over the fibres, i.e. $25.4 \times 12.7\,mm$, with a fibre of diameter $0.406\,mm$ and a length of $12.2\,mm$ (see Fig. 7.4). This is equivalent to a fibre volume fraction of 0.15%. Six inclined angles are chosen, 0^o, 14^o, 27^o, 37^o 45^o and 60^o. The first four angles are the same as in ref. [12].

Figs. 7.5 to 7.6 present the typical mesh and deformed configuration for an initially bent fibre with inclined angle of 37^o.

When a crack is first generated, fibres bridging the crack are likely to be initially straight but will gradually change in curvature and possibly kink as the crack opens, see Figs. 7.2. In these circumstances, pull-out resistance

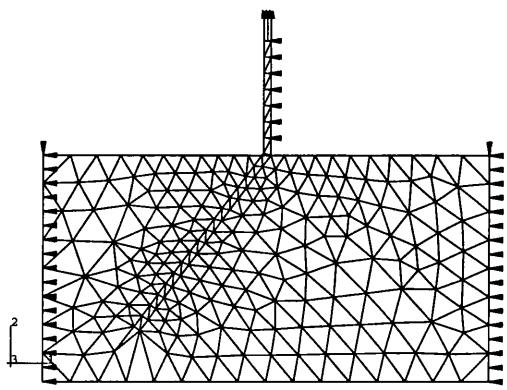

Figure 7.5: Typical Mesh for Initially Bent Fibre

is likely to be enhanced by an additional force provided by the mechanical deformation of the steel fibre at the exit point. To examine this mechanism further, a study is also carried out with initially straight fibres. The same six inclinations as those for initially bent fibres are adopted. Figs. 7.7 to 7.8 illustrate the typical mesh and deformed configuration (37^o) with the load placed exactly at the point where the fibre exits from the matrix (case A). Inevitably, there will be a certain clearance between specimen and loading grip in a practical experiment; in other words it will be almost impossible to place the load point exactly at the fibre exit. Hence we also consider another loading case B where the loading point is placed about $1\,mm$ away from the fibre exit. The relevant mesh and deformed configuration (37^o) are shown in Figs. 7.9 to 7.10.

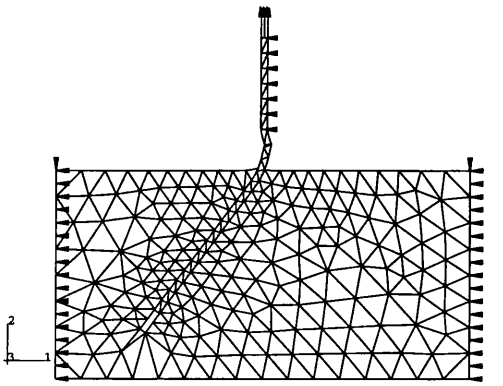

Figure 7.6: Typical Deformed Configuration for Initially Bent Fibre

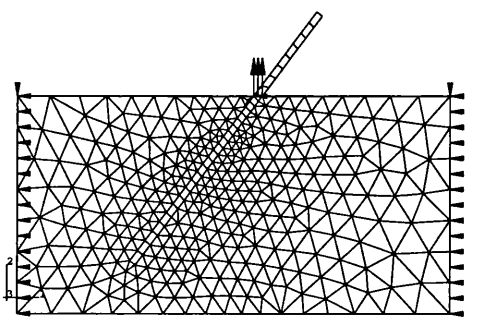

Figure 7.7: Typical Mesh for Initially Straight Fibre (case A)

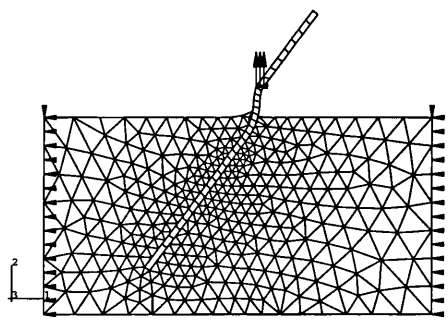

Figure 7.8: Typical Deformed Configuration for Initially Straight Fibre (case A)

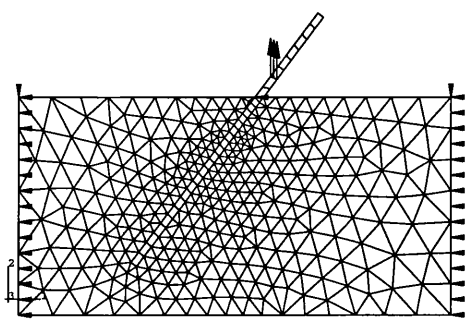

Figure 7.9: Typical Mesh for Initially Straight Fibre (case B)

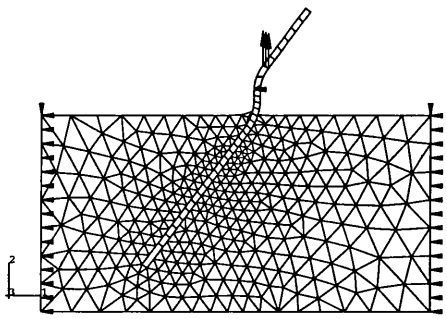

Figure 7.10: Typical Deformed Configuration for Initially Straight Fibre (case B)

7.2.1 Initially Bent Fibres

Figs. 7.11 and 7.12 illustrate the numerical and experimental results [12] respectively. The experimental results represent the average of 16 fibres (Fig. 7.12 (a)) and the average of 8 fibres (Fig. 7.12 (b)) respectively. Notably, the results exhibit substantial experimental scatter.

Comparing both, the numerical pull-out responses is found to agree reasonably with those from the average of 16 fibres for the inclined angles 0^o to 27^o. It is suspected that a 10^o change from 27^o to 37^o changes experimental behaviour so much. For those specimens with 8 fibres, however, the results for 37^o is fairly close to that of 27^o.

The peak loads are plotted in Fig. 7.13. Basically, the numerical results lie between the test data for 16 fibres and 8 fibres, and have a similar trend to the average results of 16 fibres. Increases of both the peak load and pull-out work (the area under the curve) with fibre inclination are verified from these

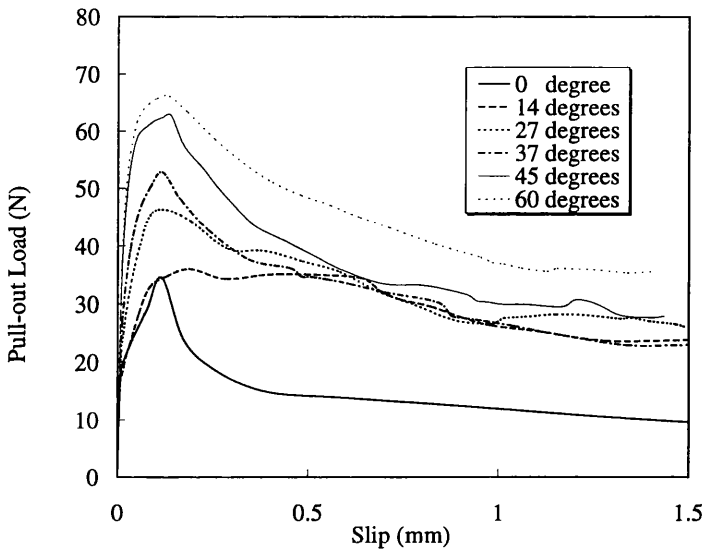

Figure 7.11: Pull-out Curved of Analyses for Initially Bent Fibre

results.

7.2.2 Initially Straight Fibres

The pull-out responses of initially straight fibres for cases A and B are depicted in Figs. 7.14 and 7.15, respectively. A significant difference is observed between cases A and B. In the former, the peak load and pull-out work increases with inclination, but in the latter it peaks at 45^o.

A similar trend was reported by Naaman and Shah [13] who used similar model parameters to the current analysis (fibre diameter of $0.406\,mm$ and embedded length of $13\,mm$). Although their specimens were similar to those with initially bent fibres in appearance (Fig. 7.16), after observing them carefully it is found there was a certain free length of fibres between the specimen and the grip, which corresponds to the loading case B. The analytical peak load for case B shows good correlation with their results (see Fig. 7.17).

Leung and Shapiro [11] performed a series of pull-out tests for steel fibre

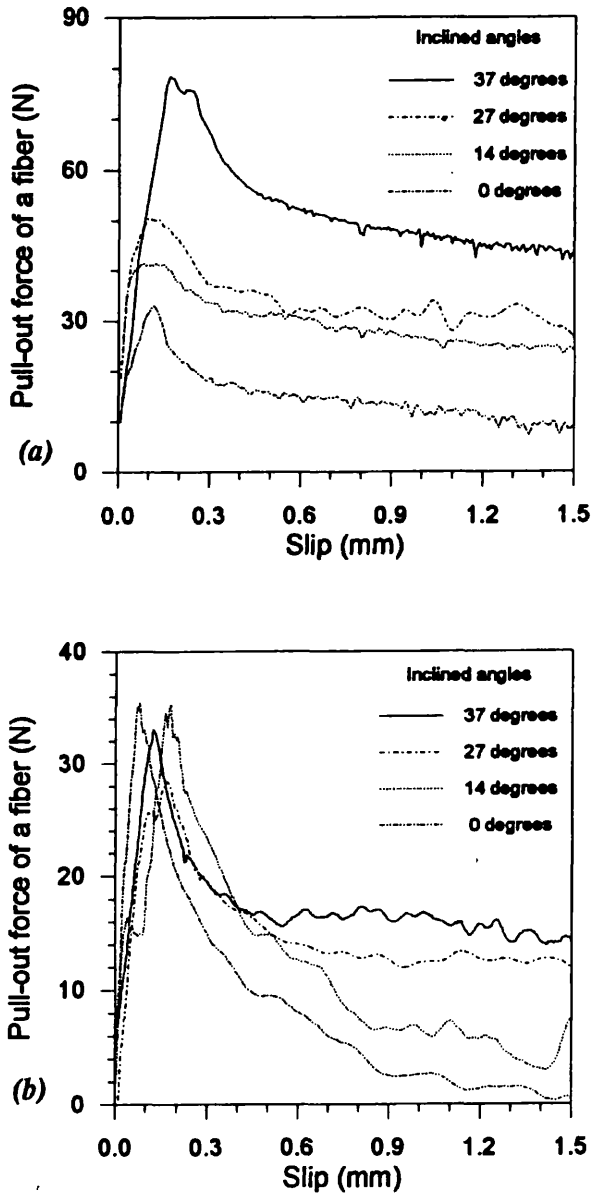

Figure 7.12: Pull-out Curves of Experiments [12]: (a) Specimens with 16 Fibres; (b) Specimens with 8 Fibres

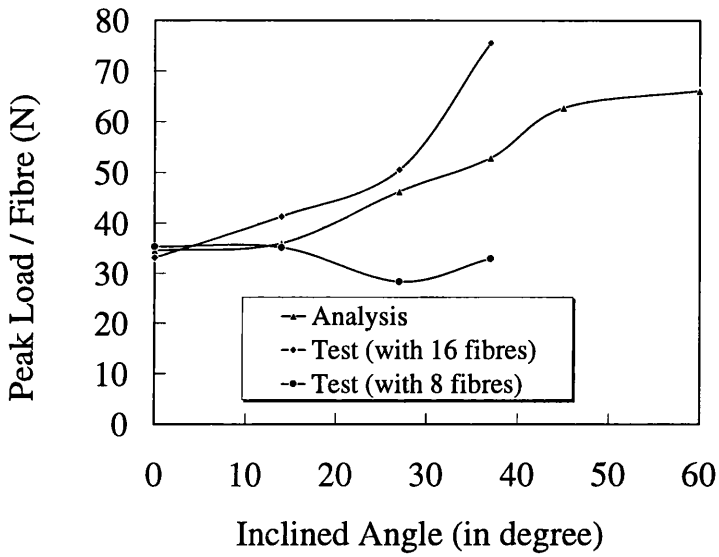

Figure 7.13: Comparisons of Peak Load for Initially Bent Fibres

reinforced concrete using specimens with initially straight fibres. The inclinations included 0^o, 30^o and 60^o. The diameter of the fibre was 0.5 *mm*. Fig. 7.18 gives a family of their experimental curves for a fibre yield strength of 275 MPa. A similar pull-out response between numerical and experimental results can be seen for the slip within 0 to 2 *mm* range. The peak loads are also presented in Fig. 7.17 and there is a maximum peak load as in case B and ref. [13] as well.

From these results, it can be concluded that the variation of peak loads depends, to a great extent, on the position of the loading point, or how much free length of fibre exists.

7.2.3 Comparison of Initially Bent and Initially Straight Fibres

To gain insight into the distinction between the different loading cases, the relationships of peak pull-out load versus inclined angle for all the cases with

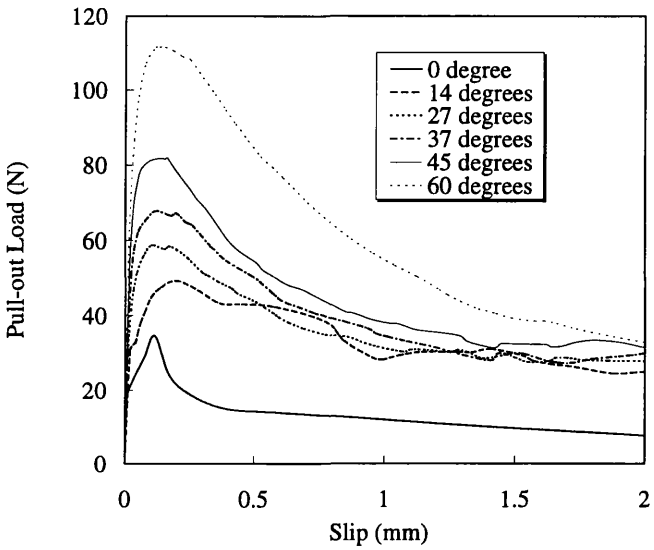

Figure 7.14: Pull-out Curves for Initially Straight Fibres in Case A

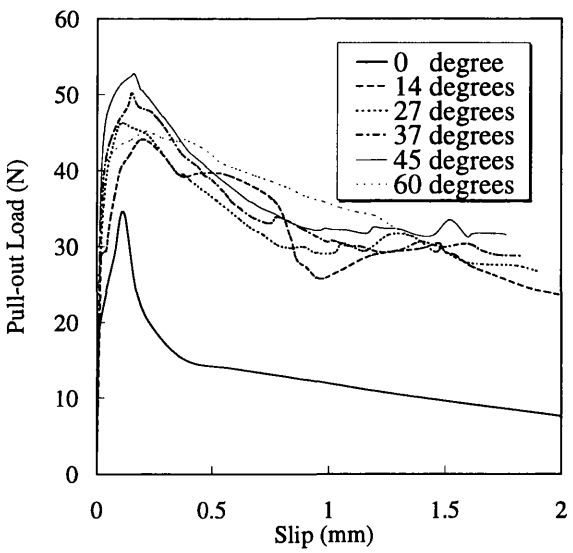

Figure 7.15: Pull-out Curves for Initially Straight Fibres in Case B

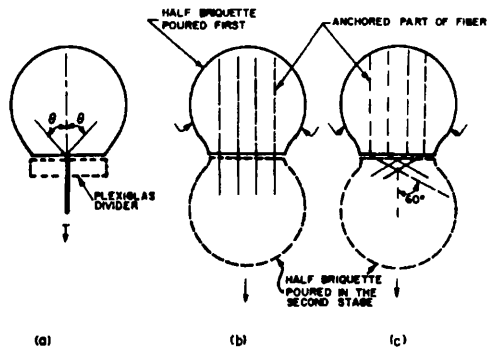

Figure 7.16: Pull-out Specimens of Ref.[13]

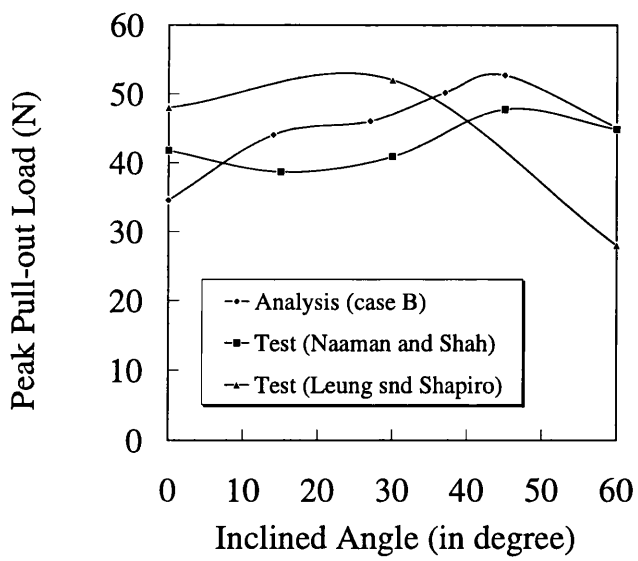

Figure 7.17: Relationships between Peak Pull-out Load and Inclination

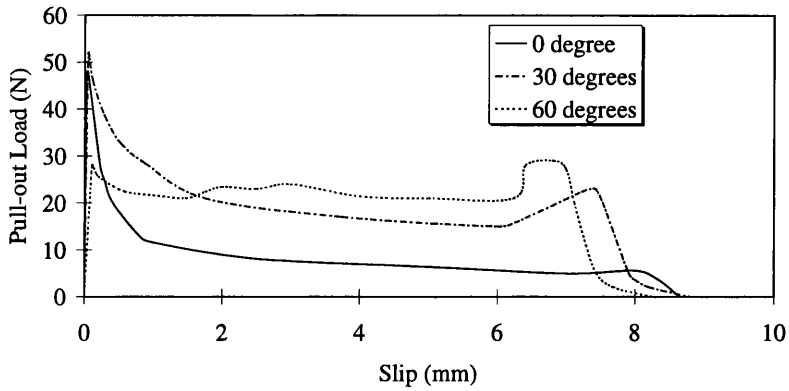

Figure 7.18: Average Response of Experimental Pull-out from Ref.[11]

initially bent and initially straight fibres are merged in Fig. 7.19.

It is evident that case A for initially straight fibres has a similar trend to initially bent fibres. The discrepancy in magnitude comes from the different initial shapes at the fibre exit where the initially bent fibre has yielded before pull-out. Their difference amplifies with the inclination, because under a large inclination the initially bent fibre is more severely yielded at the fibre exit, resulting in a decrease of the peak load , but the initially straight fibre becomes more difficult to bend, leading to a increase of the peak load.

The disparity between cases A and B for initially straight fibres stems from how much fibre extends from the matrix. It is not difficult to imagine that pulling a fibre will be more difficult for case A than case B due to a shorter bending length. The difference between the two curves is a measure of a stiffer bending action.

Overall, even though the case A is closer to the practical situation, where crack opening is equal to zero at the instant when the crack propagates cross

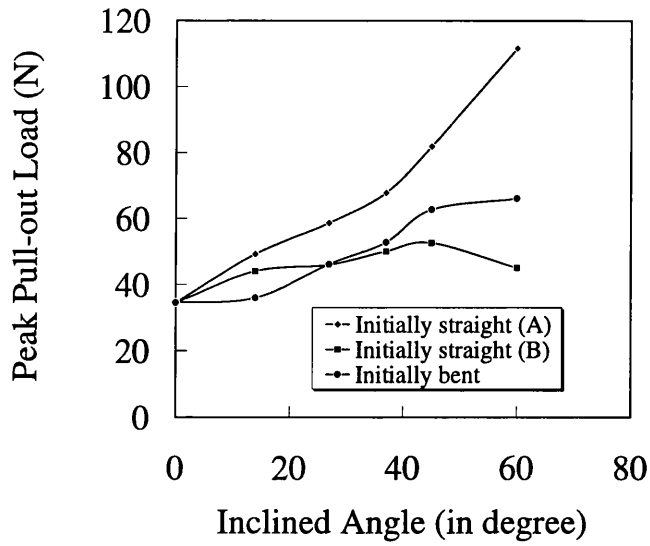

Figure 7.19: Comparison of Trends in Peak Load

the matrix, it is very difficult to simulate this loading case in an experiment. Moreover, since the diameter of fibre is only around $0.5\,mm$, a clearance of more than $1\,mm$ between the grip and specimen is unavoidable and will result in different experimental results. In this sense, a specimen with an initially bent fibre is perhaps more reasonable.

7.2.4 Discussion of Bending Mechanism

The crack bridging force P_t in Fig. 7.2 can be decomposed into two components, an axial component along the fibre (pure pull-out force) P_f and a shear component (bending force) P_b. The axial pull-out component P_f will cause fibre stretching and debonding of the fibre/matrix interface, whilst the shear component P_b will cause bending of the free length of fibre and matrix spalling at the fibre exit point. The increase of peak pull-out load with inclination is most likely due to the bending force creating a large concentrated force at the fibre exit, which raises the pull-out resistance.

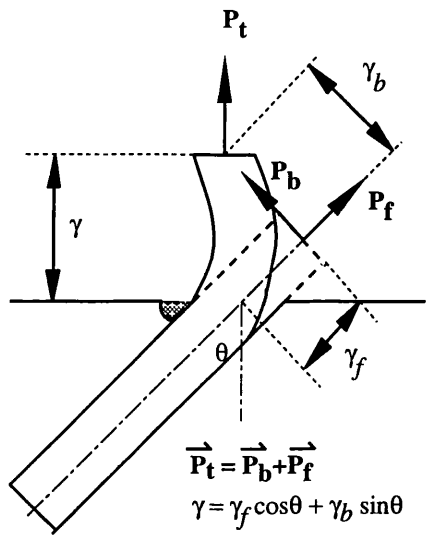

Figure 7.20: Loading Paths of Pull-out Components

To get a clear understanding of this mechanism, a loading regime (see Fig. 7.20) was devised, which separated the pure pull-out and bending actions. Since the magnitude of bending depends on the amount of fibre deformation, a pure pull-out load P_f was first applied incrementally along the fibre axis to a given value γ_f. A bending force P_b was then applied through a distance γ_{bi} at each increment i. In this way, it is possible to assess the contribution of bending under different fibre deformations.

The analytical results for 14^o and 60^o are plotted in Figs. 7.21 and 7.22 respectively. Trends have clearly emerged. Since the contribution of the shear component is less than that of the axial component when the inclination is less than 45^o, the shape of the pull-out curve is dominated by the axial component, but is the opposite for over 45^o.

Comparing curves 2 and 5 in Figs. 7.21 and 7.22 it is found that the axial component (curve 1) of inclined fibres reduces as the inclination increases, while the bending component (curve 2) increases. The action of bending is mostly completed at the early stages of pull-out, especially for large inclin-

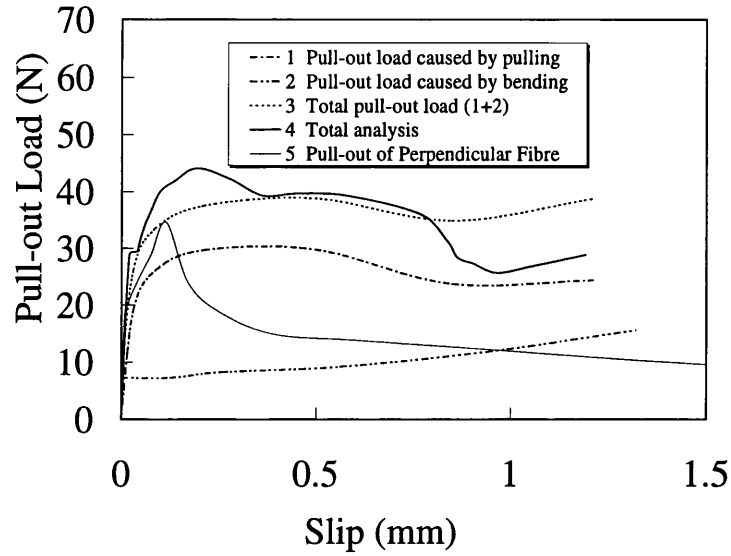

Figure 7.21: Contribution of Pullout Components for 14^o Inclinations

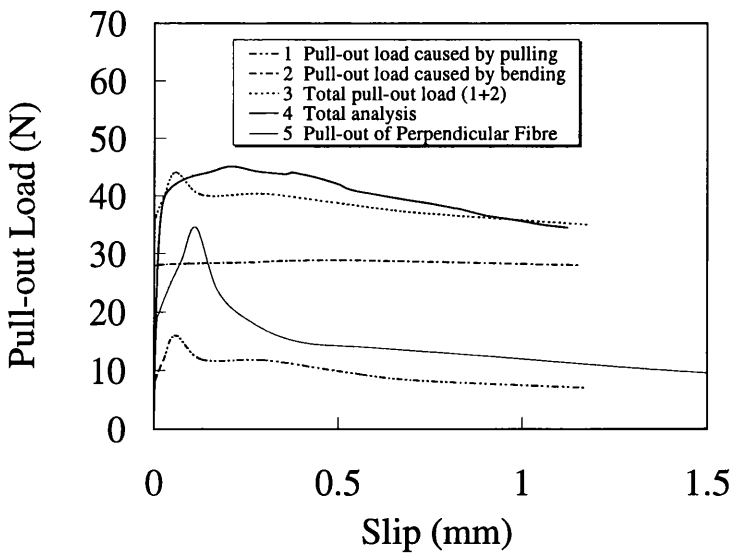

Figure 7.22: Contribution of Pullout Components for 60^o Inclinations

ation e.g. 60^o. This is clearly seen from Fig. 7.23. Therefore the increase of peak load with inclination can be attributed to bending action overwhelming that of pure pull-out. For case B, the optimum combination of the two components appears at 45^o.

Although the substantial separation of the interface at the fibre exit has not been included and the matrix damages only a little in these analyses, it is worth mentioning that, actually, substantial separation and matrix spalling can gradually develop during the early stages of pull-out when the initially straight fibre first starts to change in curvature. The larger the fibre inclination, the earlier this behaviour will occur. As a result, the peak load would decrease when the inclination exceeds a certain threshold value.

7.3 Pull-out of Multiple Fibres

Three fibre layouts are designed to study the interaction between multiple fibres: (1) perpendicular fibres; (2) parallel inclined fibres with an inclined angle of 30^o; and (3) non-parallel inclined fibres with 30^o inclinations. Typical configurations are presented in Figs. 7.24 to 7.26 respectively.

We define fibre spacing as the distance between two fibre axes. For parallel perpendicular fibres, five fibre spacings are chosen, i.e. 2ϕ, 3ϕ, 6ϕ, 11ϕ and 16ϕ. For parallel inclined fibres the spacing includes 2ϕ, 4ϕ and 6ϕ, and is extended to 11ϕ and 16ϕ for non-parallel inclined fibres.

The pull-out responses of the three layouts are illustrated in Figs. 7.27 to 7.29. It is apparent that fibre spacing has no effect on the total pull-out behaviour for perpendicular fibres. For parallel inclined fibres the effect is noticeable. When spacing is less than 4ϕ, there is a large influence on post peak behaviour. After 4ϕ, this influence disappears. However, for non-parallel inclined fibres the effect on post peak behaviour decreases gradually with the

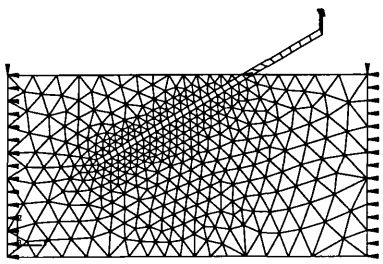

Slip=0 mm

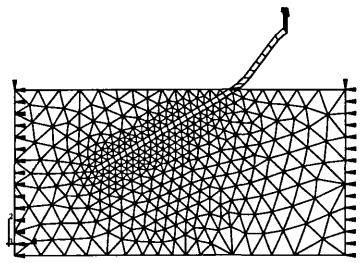

Slip=0.0335 mm

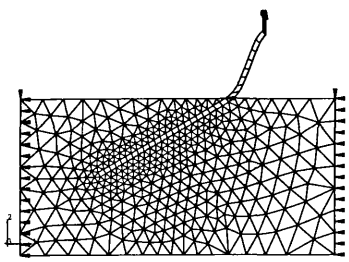

Slip=0.064 mm

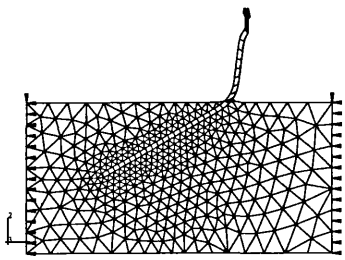

Slip=0.24 mm

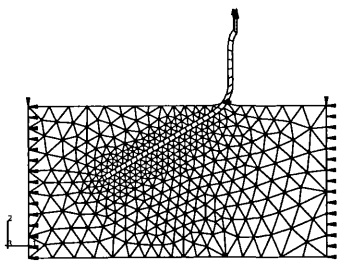

Slip=0.477 mm

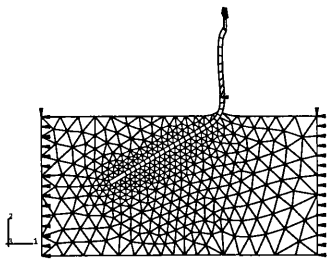

Slip=2.084 mm

Figure 7.23: Bending and Sliding of Fibre

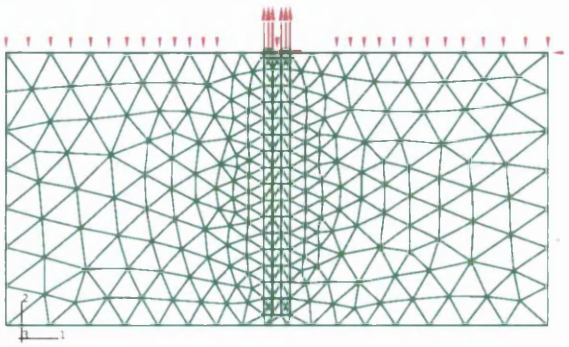

Figure 7.24: Two Perpendicular Fibres

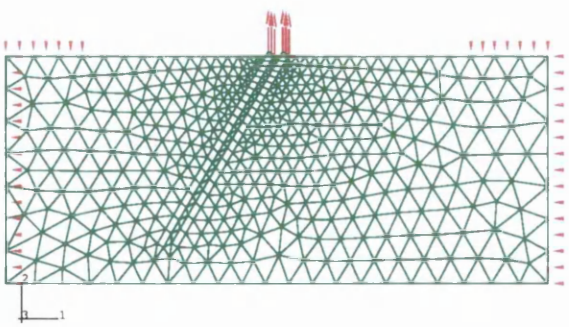

Figure 7.25: Two Parallel Inclined Fibres

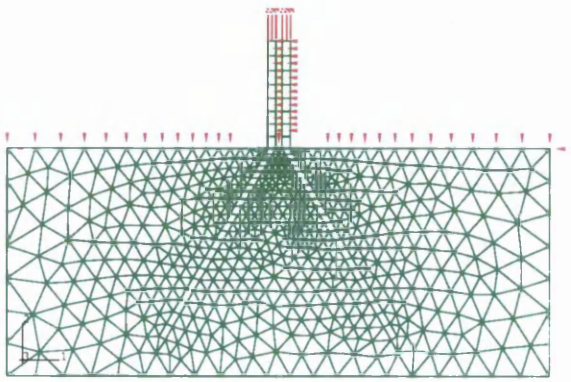

Figure 7.26: Two Non-parallel Inclined Fibres

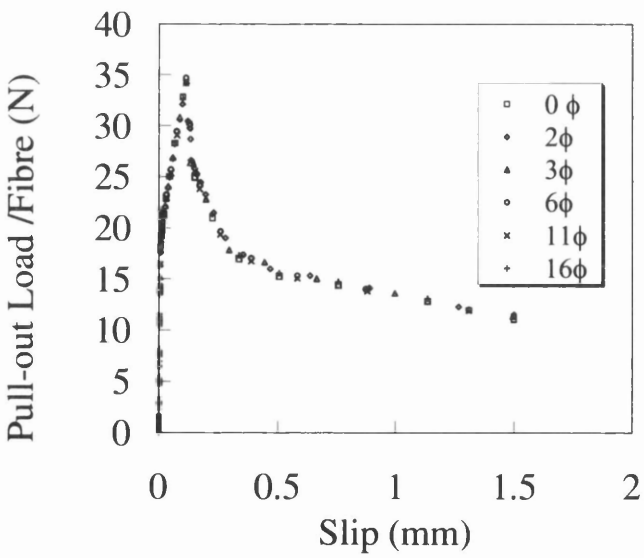

Figure 7.27: Pull-out Response of Perpendicular Fibres

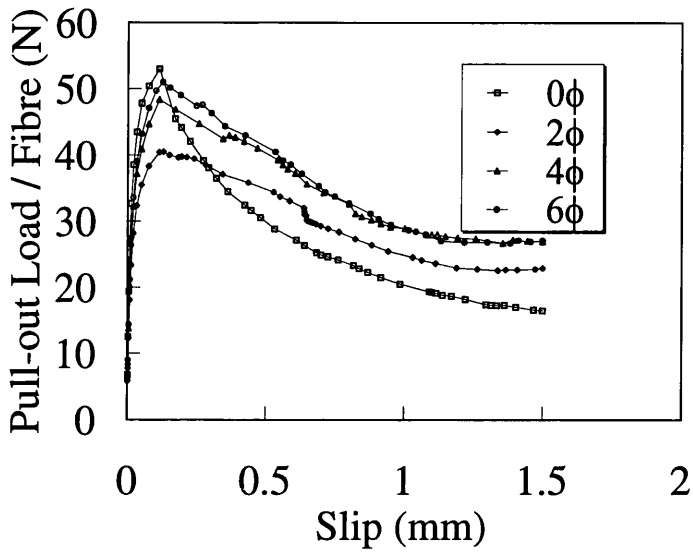

Figure 7.28: Pull-out Response of Parallel Inclined Fibres

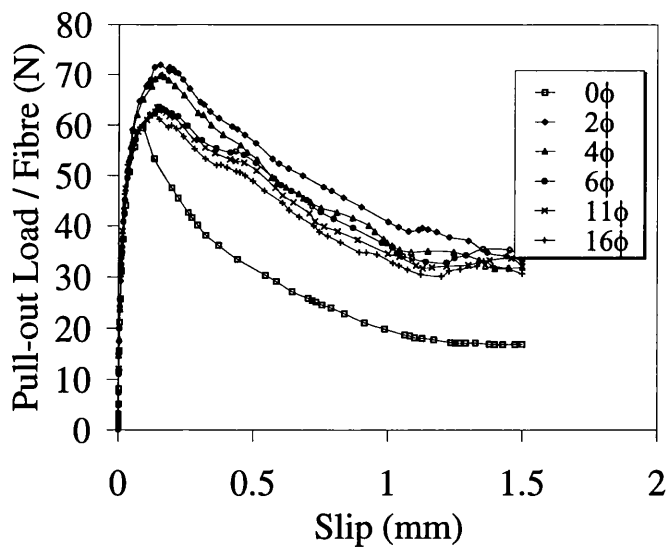

Figure 7.29: Pull-out Response of Non-parallel Inclined Fibres

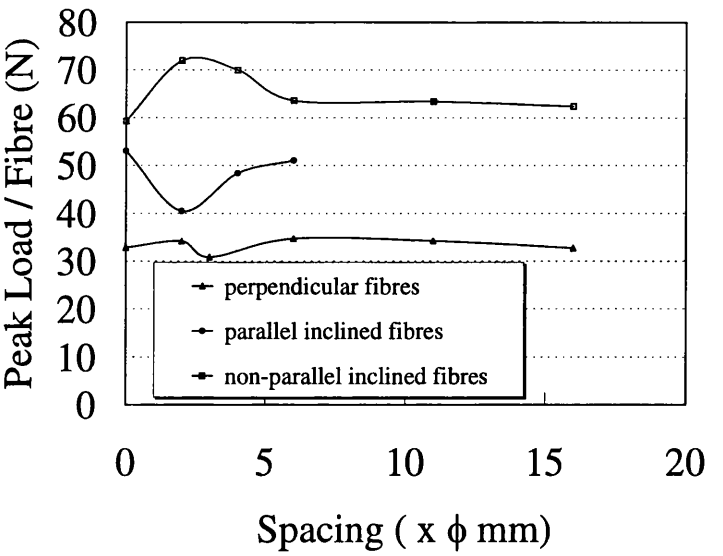

Figure 7.30: Influence of Fibre Spacing on Peak Pull-out Load

increase of spacing.

The effect of fibre spacing on peak pull-out load is shown in Fig. 7.30 for all three layouts. Generally, there is little change on peak loads when the fibre spacing is over 6ϕ, which coincides with experimental results [61]. When fibre spacing is less than 6ϕ, the influence is different for different layouts.

To undertand further the interaction between fibres under small spacing, Figs. 7.31 to 7.33 provide contours of the principal stresses. It can be seen from Fig. 7.31 that based on given boundary condition and bond property the compressive principal stress presents a conical distribution. For small spacing, less then 6ϕ, double fibres behave like a thick fibre. Only a small change of peak load is caused (Fig. 7.30).

However, for parallel inclined fibres (see Fig. 7.32) the concrete between the two fibres is severely damaged due to bending of the fibres. This induces a decrease in the peak pull-out load in Fig. 7.30.

As for non-parallel inclined fibres, Fig. 7.33 shows that as spacing de-

creases the stressed area of concrete changes from only outside of the fibres to including the whole concrete. It is very likely that the existence of one fibre relative to the other fibre enhances the stiffness of concrete when the two fibres are close enough to each other. Thus an increase of peak load occurs.

7.4 Conclusion

The method of modelling bond and pull-out behaviour presented in Chapter 4 can satisfactorily describe the response of cement-based composites reinforced by steel fibres. The model is applicable for the cases with large interfacial sliding and randomly distributed fibres, as long as the bond-slip property of a perpendicular fibre is known in advance and the proper constraints are defined in the contact algorithm with friction. The development of the model offers a computationally efficient approach for investigating composite and interface behaviour.

The analyses of pull-out behaviour of single fibre indicate that both the friction and bending mechanisms are important factors in understanding and investigating the crack bridging forces of FRCC. For low inclinations, friction is dominant, but as the inclination increases, bending takes over as the dominant mechanism. The bending mechanism can improve bond efficiency especially for inclinations less than 60^{o}. From the analyses, it can be concluded that inclined fibres can increase the ultimate strength of a composite through a gain in the peak pull-out load, and enhance resistance against crack propagation and postpone rupture by providing more pull-out work.

Pull-out specimens with initially straight fibres can reasonably represent a practical engineering case, but it is difficult to load the fibre exactly at the fibre exit. The trends in peak pull-out load versus inclination is variable with

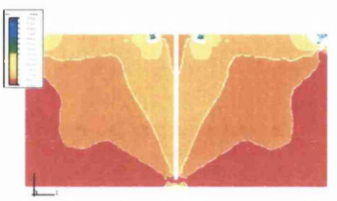

Single Fibre

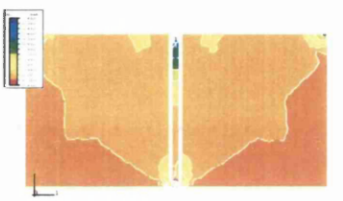

Spacing=2ϕ

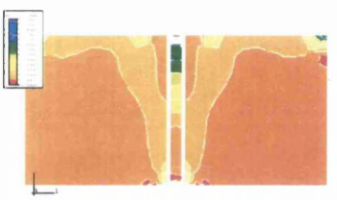

Spacing=3ϕ

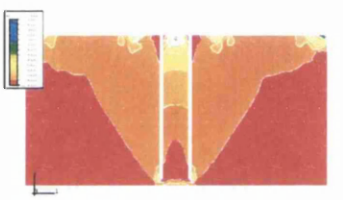

Spacing=6ϕ

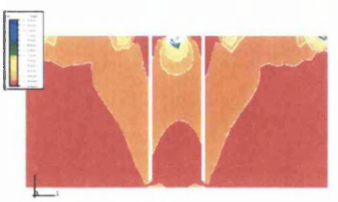

Spacing=11ϕ

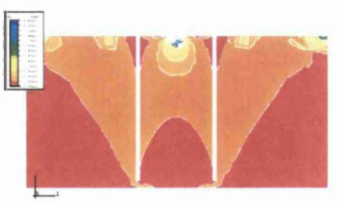

Spacing=16ϕ

Figure 7.31: Compression Principal Stress Contours from Perpendicular Fibres

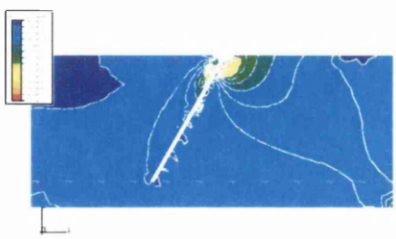

Single Fibre

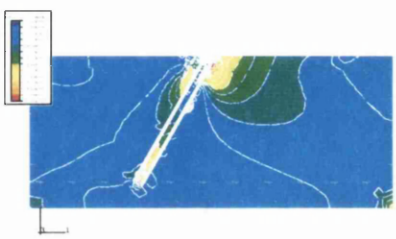

Spacing=2ϕ

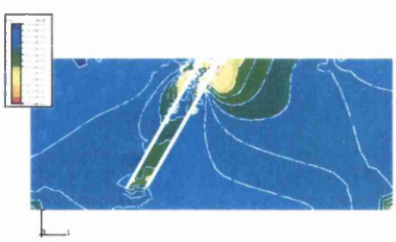

Spacing=4ϕ

Spacing=6ϕ

Figure 7.32: Tensile Principal Stress Contours from Parallel Inclined Fibres

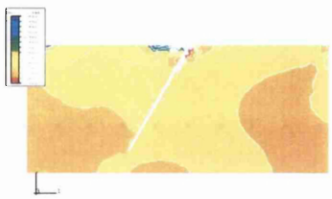

Single Fibre

Spacing=2ϕ

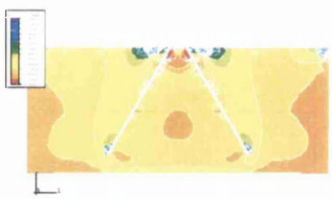

Spacing=4ϕ

Spacing=6ϕ

Spacing=11ϕ

Spacing=16ϕ

Figure 7.33: Compressive Principal Stress Contours from Non-parallel Inclined Fibres

different loading approaches. Perhaps specimens with initially bent fibres are proper substitute for experimental investigation.

The investigation on pull-out with multiple fibres demonstrates that fibre spacing of about 6ϕ represents a threshold. Fibre spacing of greater than 6ϕ has basically no effect on the pull-out behaviour, including peak load and post peak response. Within a spacing of 6ϕ, peak load increases for non-parallel inclined fibres, but decreases for parallel inclined fibres. The influence of fibre spacing on perpendicular fibres may be ignored. When spacing is less than 6ϕ the layout with non-parallel inclined fibres can increase the cracking resistance and bond efficiency.

Therefore, it is recommend that during manufacturing process of FRCC fibres should be completely mixed into concrete so as to prevent parallel layout occurring. However, for the fibre volume fraction commonly used in practical engineering, small fibre spacing would not exist.

In Ouyang et al's tests [12], fibres were laid out parallel with the spacing above 31ϕ for the specimen with 8 fibres and 15ϕ for that with 16 fibres. Based on the studies in this chapter, its difference between the results with 8 fibres and 16 fibres is not caused by the effect of fibre spacing, but must be due to other factors, most probably errors in the experimental procedures.

Chapter 8

Numerical Modelling of Bar Pull-Out in Reinforced Concrete

It is well known that bond behaviour in reinforced concrete plays an important role in understanding and determining the behaviour of reinforced concrete structures under monotonic and cyclic loading. Many experiments have been carried out for reinforced concrete with straight bars, but much less for curved bars, e.g. Phillips et al 1995 [14], and Hota and Naaman 1997 [137]. Similarly, the numerical modelling of pull-out and cyclic behaviour for straight steel bars (including plain, deformed and anchored bars) is often reported, for example refs. [76, 138, 139], but that for curved bars has been little addressed. The difficulty and complexity of modelling is caused by the large separation between the curved reinforcement and concrete under certain pull-out loads, as well as the concrete becoming severely damaged in the vicinity of the curved bar. Convergence and numerical stability become troublesome problems.

The strategy developed in this thesis for the pull-out of fibres is also appropriate to the pull-out of reinforcing bars from concrete, albeit on a dif-

ferent scale. Thus the contact algorithm with friction introduced in Chapter 2 is applied to the interface between the bar and concrete. Bond behaviour and interfacial separation are manipulated by means of different contact constraints. Concrete is simulated by the biaxial concrete damage model described in Chapter 5 and ref. [140]. Finally, the numerical results under pull-out and cyclic loading are compared against experimental results obtained elsewhere.

8.1 Numerical Modelling Approach

Two dimensional finite element analyses are conducted to model the pull-out responses of reinforced concrete with 0^o, 30^o, 60^o and 90^o curved bars.

In order to compare numerical solutions with the experimental results, the model sizes and material properties chosen are similar to those of the specimens in ref. [14] whose detailed configurations are shown in Fig. 8.2. The dimensions of the concrete block is $600 \times 625\,mm$. The diameter of steel bar is $32\,mm$ and the embedded length of bar is $350\,mm$ (see Fig. 8.1). Although the concrete blocks were reinforced by some longitudinal bars and stirrups, their effect is only to increase slightly the stiffness of the concrete. They have no influence on the pull-out response during a numerical analysis and hence their existence is not considered.

The Von Mises yield criterion and the biaxial concrete damage model (model IV) are applied to the steel bar and concrete respectively. Since the required property curve of concrete was not given in ref.[14], the damage model is calibrated using the data from refs. [9, 5]. Tab.8.1 lists the material properties employed in the analyses and from the experiments. The subscripts c, s and u denote concrete, steel bar and ultimate strength respectively.

In order to simulate the practical loading situation in the experiment of

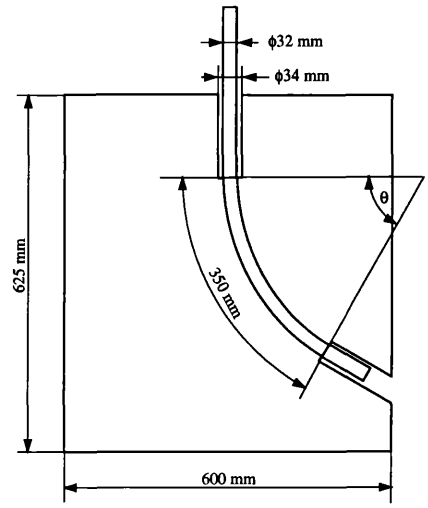

Figure 8.1: Dimension of Specimen for Numerical Modeling

Table 8.1: Material Properties Used in Analysis and from Experiment

	Analysis		Experiment	
E_c	31.8	GPa	26.05~34.13	GPa
E_s	205.7	GPa	205.7	GPa
ν_c	0.18		—	
ν_s	0.3		—	
f_{cu}	34.8	MPa	46.5~54.1	MPa
f_{su}	455	MPa	455	MPa

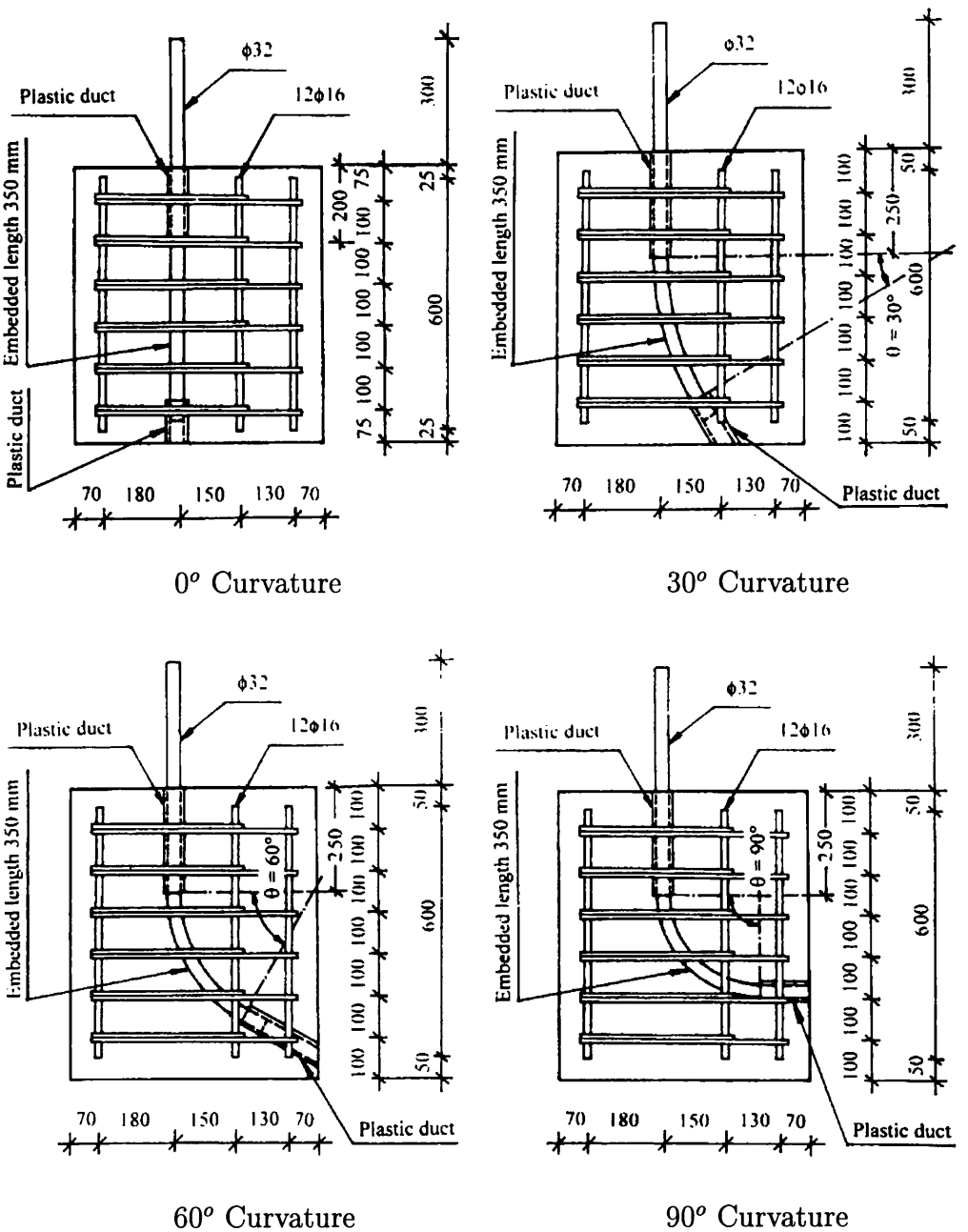

0° Curvature

30° Curvature

60° Curvature

90° Curvature

Figure 8.2: Configurations of Experimental Specimen [14]

ref. [14] the model is constrained at the top. To ensure the bars are pulled out along their curvatures as observed in the experiments, a series of constraints are imposed along the curved segments. This also guarantees the effective implementation of the contact algorithm.

Fig. 8.3 shows the meshed configurations. 8-node quadratic plane strain elements are adopted for both bar and concrete. Since the volume of concrete is much larger than that of steel bar, the concrete is divided into two zones, depending on the distance from the steel bar. The zone in the vicinity of the interfaces is the main transmitting zone of the pull-out load and is densely meshed. The zone far from the bar is sparsely meshed. The mismatch of element nodes between the two zones is dealt with by means of displacement constraint equations. This reduces the number of elements and computational time.

In order to ensure the transmission of tangential load when separation stems from bar curvature and matrix constraint, interface constraints in the normal direction adopts the soft contact relation described in Eq. 6.20 of Chapter 6, with $p_0 = 2.0$ MPa as the bond strength. Eq. 6.24 in Chapter 6 is employed as the constraints in the tangential direction, with regression coefficients: $k_s = 950.0$ N/mm, $a_1 = 1.5921$ N/mm, $b_1 = 0.0832$, $a_2 = 0.87$ N/mm and $b_2 = -0.2678$.

In addition, considering a residual bond stress exists on the interface after full debonding, a residual shear stress of 0.5 MPa observed from the experimental data is exerted on the interfaces after the separation is detected. In snubbing modelling, the friction coefficient of 0.1 is used.

Displacement loading is employed in order to simulate the softening behaviour under pull-out. The finite element analysis used ABAQUS in conjunction with the developed codes for the interfacial constraints and the biaxial

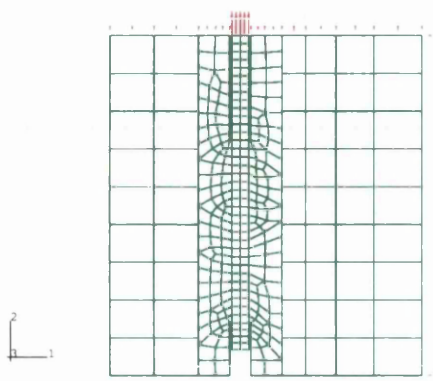

0^o Curvature

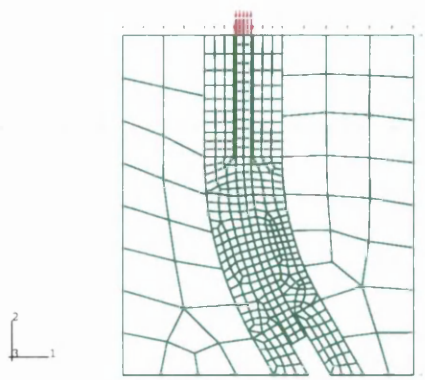

30^o Curvature

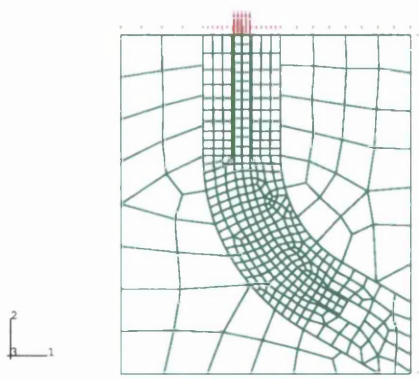

60^o Curvature

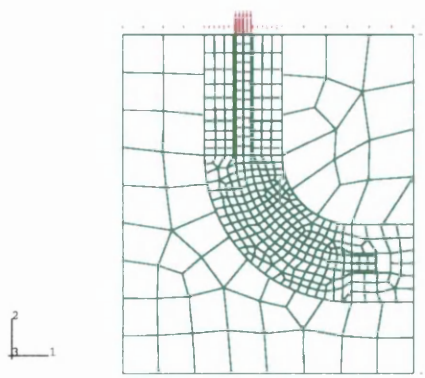

90^o Curvature

Figure 8.3: Meshed Configurations

damage model of concrete.

8.2 Results and Discussion

8.2.1 Pull-Out Test

Fig. 8.4 shows the deformed configurations. Figs. 8.5 to 8.7 present contours of maximum principal stress in the concrete, normal stress in the bars and shear stress respectively. The maximum tensile principal stress vectors is given in Fig. 8.8

From Fig. 8.5, it is found that using subregion meshing has no influence on the stress distribution, but it greatly reduces the number of elements and increases computational efficiency. As the curvature increases, the maximum principal stress distribution tends to concentrate over a small region on the concave side of the bar rather than covering the whole concrete. This suggests that with different curved bars the concrete will fail in different modes under further loading.

The normal stress distributions along the bars indicate that the stress transmits gradually from the active end to the passive end. As curvature increases, the stress concentrates on the inside of bar curvature. However, the shear stress distributions show localisation around the interfaces.

The distribution of maximum tensile principle stress in Fig. 8.8 predicts the positions of debonding on the interfaces. Clearly, as the curvature increases debonding happens from on the two interfaces to only on the convex side. This implies that the interface outside of the curved bar is inclined to damage.

Fig. 8.9 illustrates the relationship of pull-out load versus slip, in which N and T denote the numerical and test results respectively. The trends of

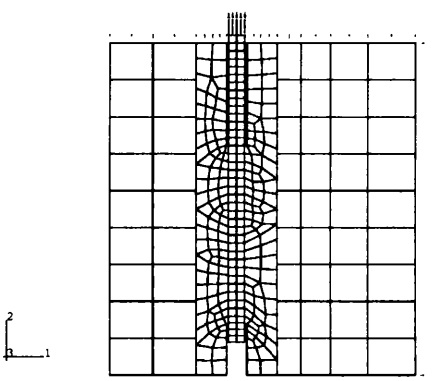

0^o Curvature

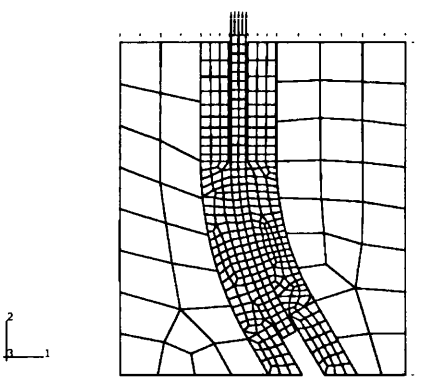

30^o Curvature

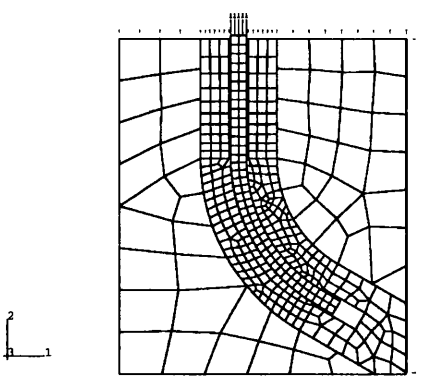

60^o Curvature

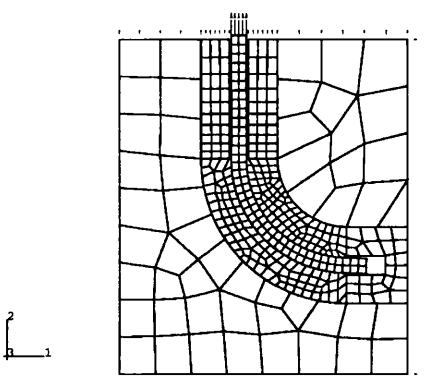

90^o Curvature

Figure 8.4: Deformed Configurations

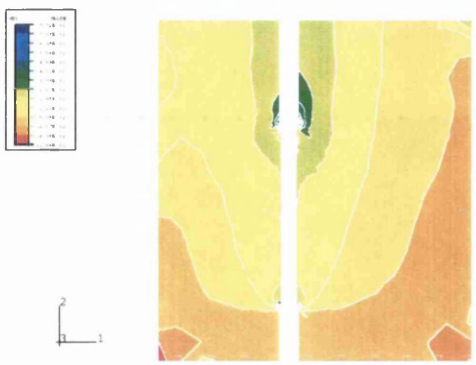

0^o Curvature

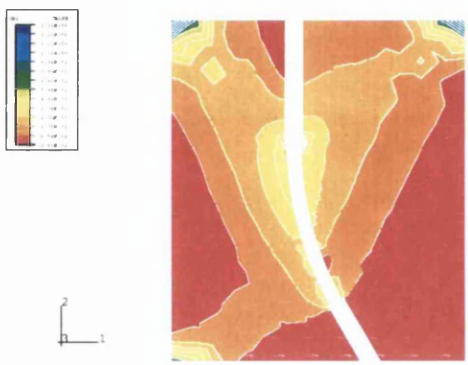

30^o Curvature

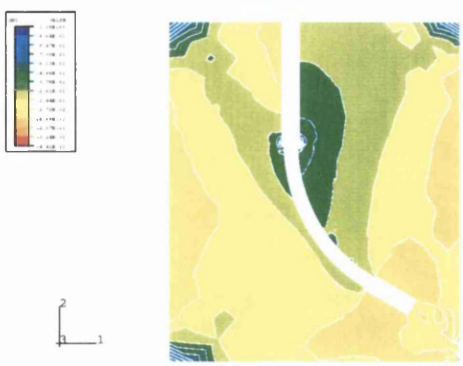

60^o Curvature

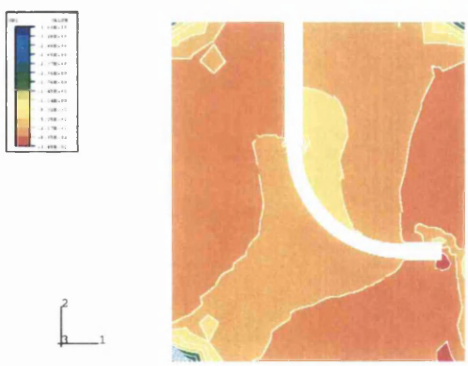

90^o Curvature

Figure 8.5: Maximum Principal Stress Contours of Concrete

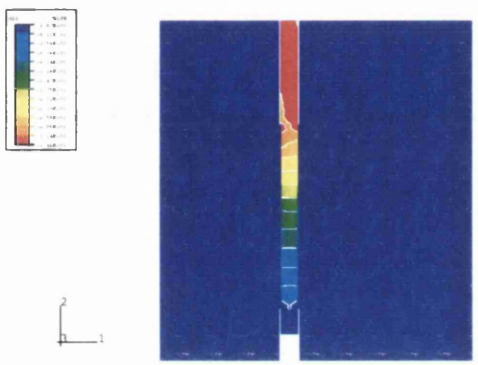

0^o Curvature

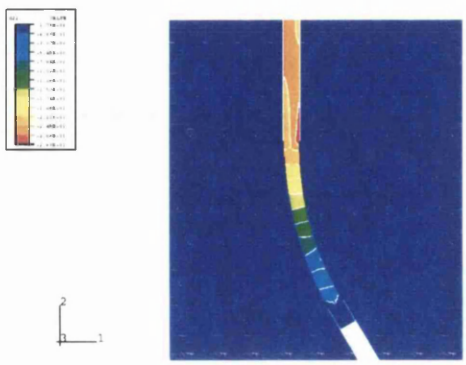

30^o Curvature

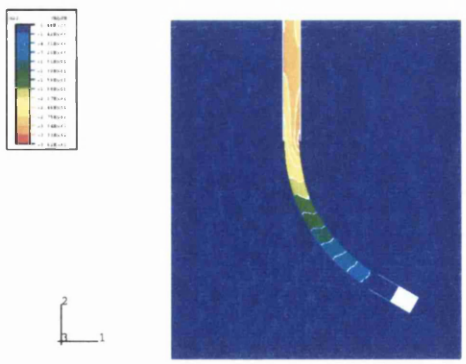

60^o Curvature

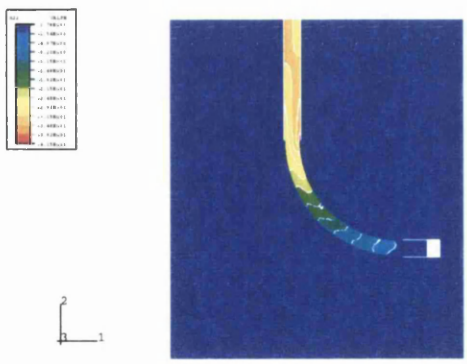

90^o Curvature

Figure 8.6: Normal Stress Contours of Bar

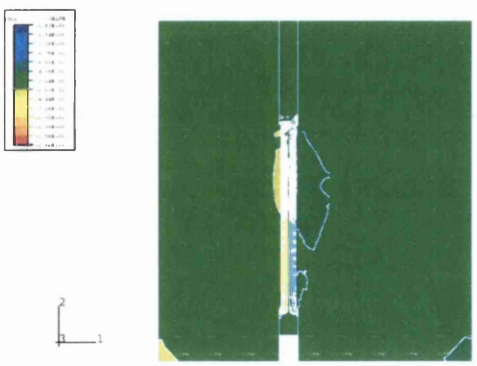

0^o Curvature

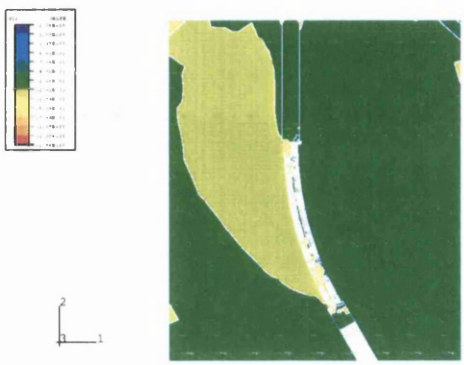

30^o Curvature

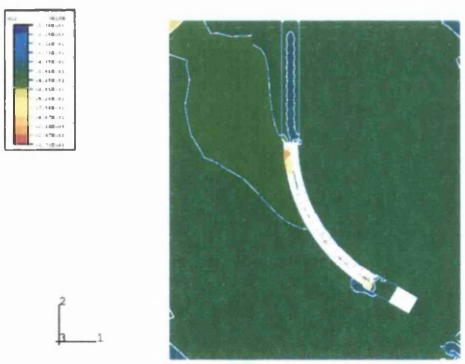

60^o Curvature

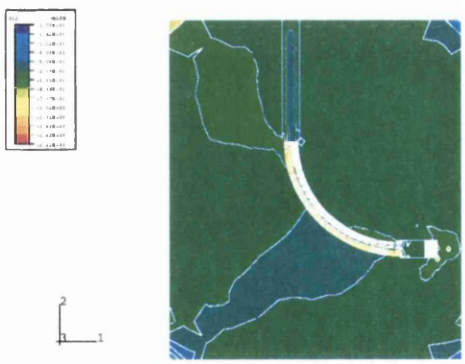

90^o Curvature

Figure 8.7: Shear Stress Contours

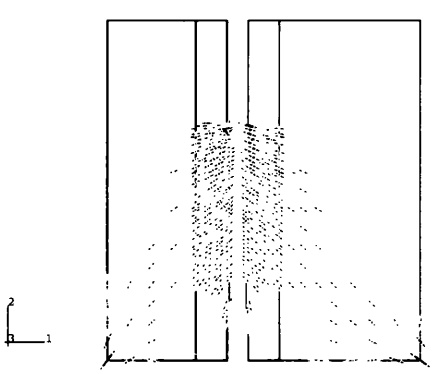

0^o Curvature

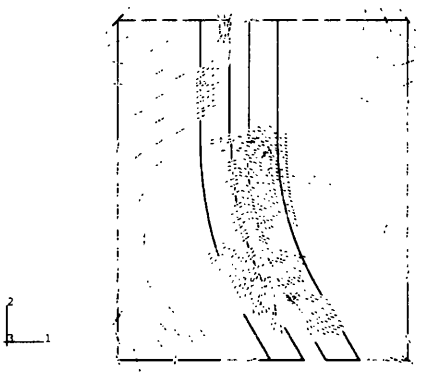

30^o Curvature

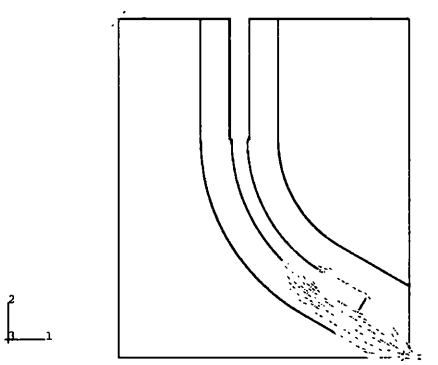

60^o Curvature

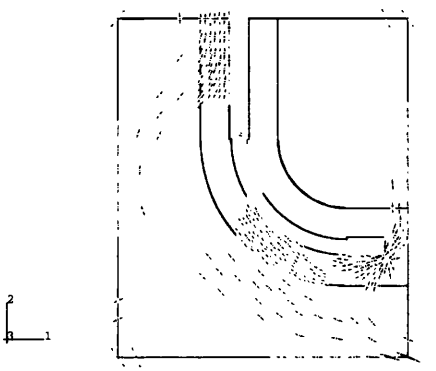

90^o Curvature

Figure 8.8: Maximum Tensile Principal Stress Vectors in Concrete

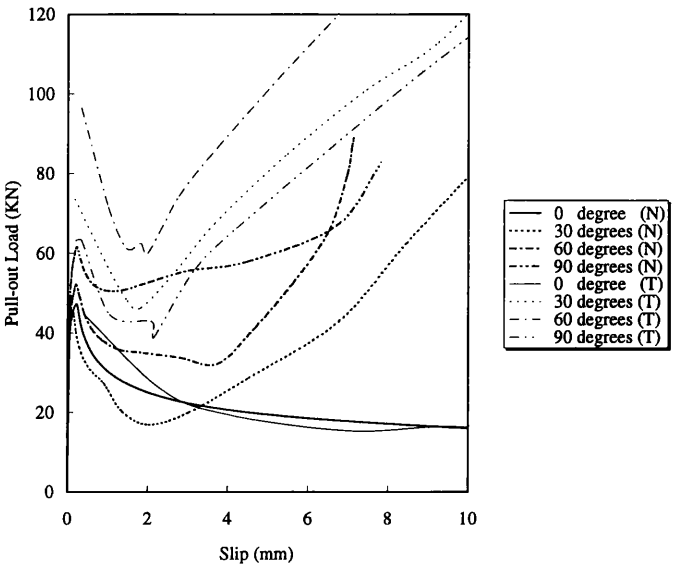

Figure 8.9: Relationship of Pull-Out Load versus Slip

both the numerical and experimental results for 0^o to 60^o are similar. Differences in magnitude are expected, as the concrete strength in the analysis was lower than that of experimental specimens. When the strength of concrete contributes little to the overall pull-out response, such as for the 0^o curvature, good agreement between the analysis and experiment is achieved. For 90^o curvature, the tendency of numerical analysis is similar to that of the experiments with 16 mm diameter bars (see Fig. 8.10). Since no experimental repeat test was carried out and it is difficult to bend 32 mm diameter bar to the desired curvature, it is suspected that there may have been some experimental random error. This may explain the difference in trends between 16 and 32 mm diameter bars for 90^o curvature in the experiments.

Pull-out load and slip relationships demonstrate that pull-out energy increases with curvature within 0^o to 60^o, i.e. the curvature raises the resistance to pull-out, as expected.

The axial stress distributions in the bars and shear stress distributions

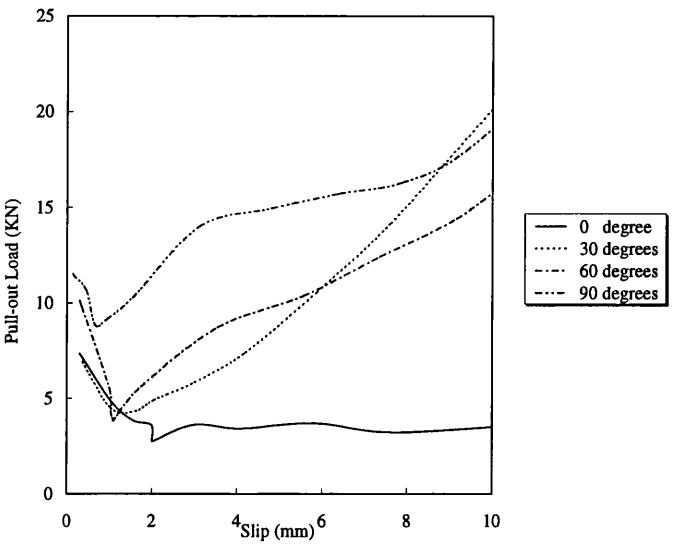

Figure 8.10: Relationship of Pull-Out Load versus Slip from Experiments with $16mm$ diameter bars

along the interfaces are plotted in Figs. 8.11 to 8.12, in which L and R denote left and right interfaces respectively. Axial stress distributions indicate that the difference in magnitude between the left-side and right-side interfaces increases with curvature, which is also apparent in Fig. 8.6. The stress from the active to passive ends is basically a linear distribution. Shear stress distribution with loading develops gradually from the passive end to the whole embedded length.

8.2.2 Cyclic Loading Test

A cyclic pull-out loading test was conducted for the reinforced concrete with a straight bar. The modelling method and parameters chosen are the same as those in the monotonic pull-out loading, except that an unloading stiffness is introduced. Experimental results in Fig. 8.13 indicated that unloading stiffness of the cyclic pull-out is almost a constant. Based on these data a

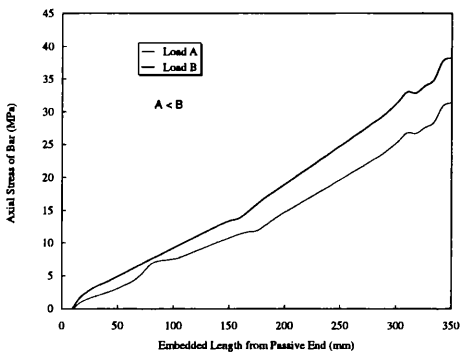

0° Curvature

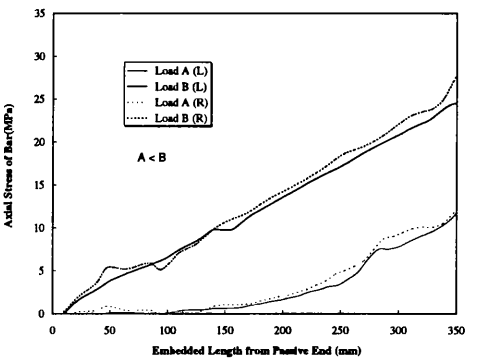

30° Curvature

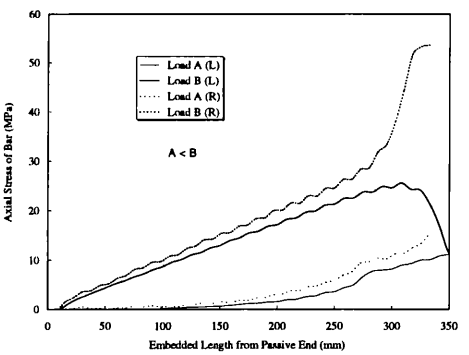

60° Curvature

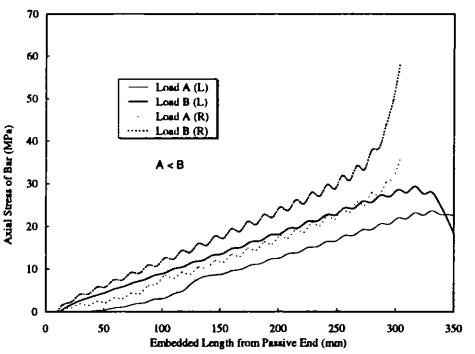

90° Curvature

Figure 8.11: Axial Stress Distributions in Bars

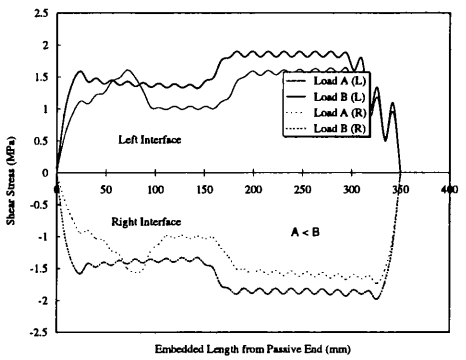

0^o Curvature

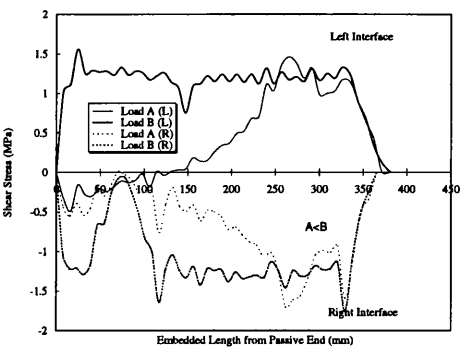

30^o Curvature

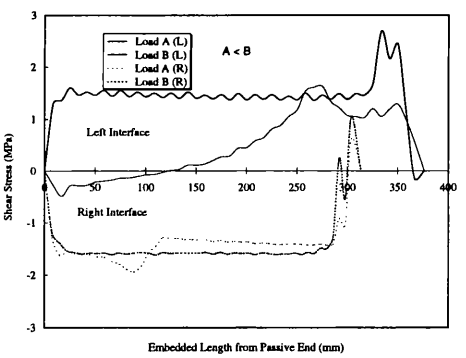

60^o Curvature

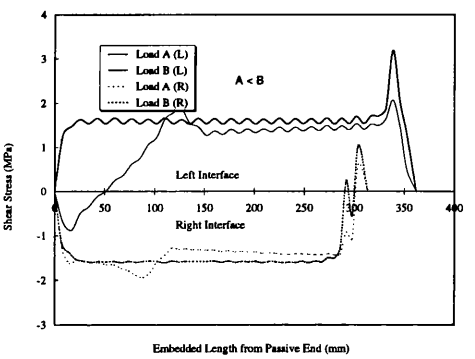

90^o Curvature

Figure 8.12: Shear Stress Distributions along Interfaces

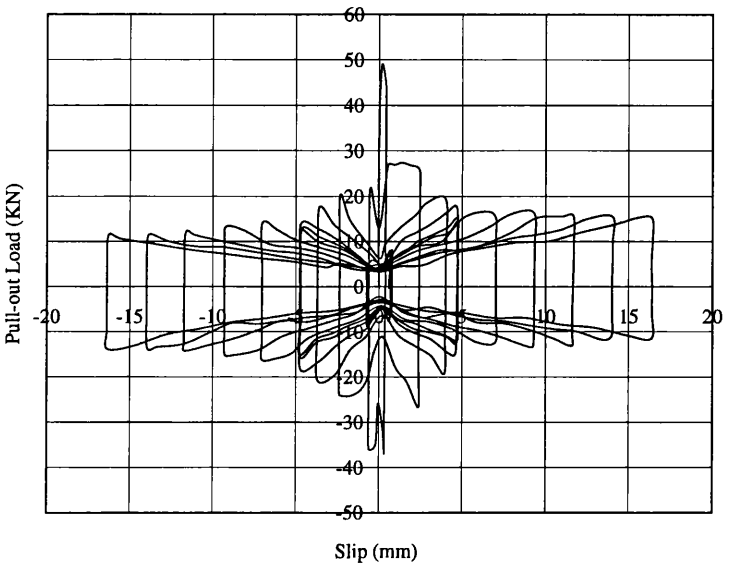

Figure 8.13: Cyclic Pull-out Response from Experiment [14]

unloading stiffness of 850 MPa is defined for the current analysis. The bond stress-slip relationship employs the tensile envelope of experimental bond stress-slip curve under cyclic loading. The results from both the analysis and experiment are compared in Fig. 8.14, where only the tensile curves are shown for the experimental data. Numerical results are found to fit favorably with experimental results.

8.3 Conclusion

The application of a contact algorithm with friction and a concrete damage model accompanied with reasonable constraints to reproduce the pull-out behaviour of reinforced concrete with curved bars is promising. Generally, the complexity in simulating large sliding and separation between contact surfaces has been overcome. The similarity in trends between the numerical analyses and experiments under pull-out, especially for 0^o to 60^o, suggests

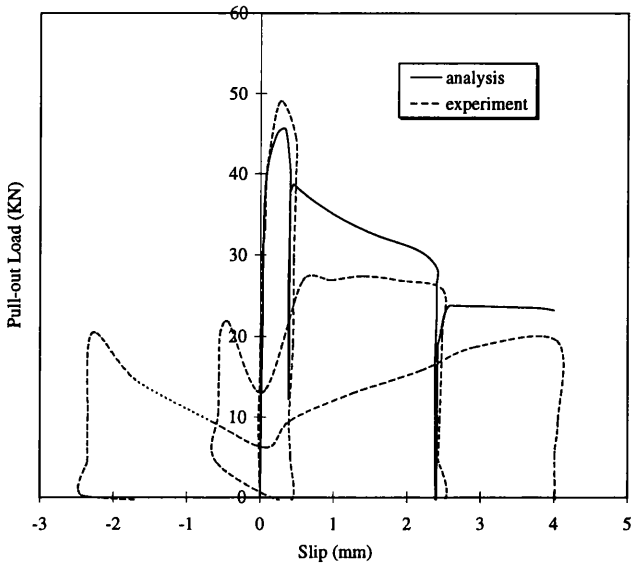

Figure 8.14: Comparison of Numerical Analysis with Experimental Result under Cyclic Loading

that the model is currently reproducing the main mechanisms. To obtain closer numerical agreement, more accurate data for the concrete behaviour is required.

The analytical results indicate that the increase of bar curvature can raise greatly the resistance of pull-out. The efficiency is more obvious for bars with 30^o to 60^o curvatures. For curved bar reinforced concrete, interfacial debonding occurs first at the outside of the bars.

The modelling under cyclic loading is also satisfactory.

Chapter 9

Conclusions and Recommendations

9.1 Summary and Conclusions

This thesis was aimed at developing an effective and comprehensive numerical method for modelling the pull-out response of FRCC, especially for those complex cases with inclined fibres, large interfacial slip and cyclic loading. In this study, many problems were encountered and solved, including how to determine debonding criterion; how to tackle separation of interfaces, fibre sliding against the matrix and severe matrix damage etc. Finally, a pull-out model was developed which consists of a contact algorithm with friction for the interface and damage models for the matrix. This model was used to research the pull-out response of cement composites reinforced by randomly distributed fibres, including single and double inclined fibres with different layouts. Its application was also extended to curved bars in reinforced concrete. From the work, the following conclusions can be made.

- A pure damage model and an inelastic-damage model were proposed. In these models damage is controlled by damage energy release rate. The development of the corresponding computational algorithms en-

ables these models to be implemented in a two dimensional finite element program. Their features are that model I is fairly simple and easy to program, whilst model II can describe the nonlinear loading and unloading responses of concrete subjected to monodirectional cyclic loading very well. Although the two models are only applicable to concrete subjected to monodirectional loading, they are essential steps towards developing more complex damage models.

- The development of damage models III and IV provide effective concrete damage models for revese cyclic and biaxial loading. The description of model III in strain space makes the simulation of tensile and compressive damage by means of separating strain much easier than existing models described in stress space. The introduction of a weighted average damage parameter in model IV overcomes the shortcoming of separating stress/strain into positive and negative and greatly simplifies implementation in the finite element method. Meanwhile, the design of the damage multiplier distinguishes the different contributions of the hydrostatic and deviatoric components of the stress/strain tensor to damage and produces modelling under biaxial loading. The implementation of model IV under biaxial tension and biaxial compression reproduces completely the biaxial experimental results of Kupfer et al.

- The proposed pull-out modelling method merges various pull-out mechanisms of FRCC, such as bonding, debonding, fibre sliding, friction, fibre bending, snubbing, matrix spalling and the substantial separation of the fibre at the exit from the matrix, into one two dimensional finite element model. In this approach, the use of a contact algorithm with

friction makes the interfacial simulation straightforward, requiring only an experimental pull-out load-slip relationship for a single perpendicular fibre, and no additional strength or fracture criteria. The modelling of different interfacial separation magnitudes can be realized by means of changing the constraint conditions in the normal direction of the interface. The development of the damage models enables the automatic simulation of matrix spalling.

- The sensitivity analyses of various modelling parameters provide a guide for using the model. The analyses indicate that to obtain reliable numerical results the choice of structural and interfacial constraints, the number of elements and the separation length at the fibre exit have to be taken into account.

- The applications of the pull-out model to FRCC and bar reinforced concrete, including the cases with single fibre, multiple fibres and curved bars, demonstrate the model can deal with large sliding, large separation and full pull-out. Its application offers a computationally efficient approach for investigating composite behaviour.

- The pull-out results of single inclined fibres indicate that both friction and bending mechanisms are important factors in understanding and investigating the crack bridging forces of FRC. The former holds sway for cases with smaller fibre inclination, whilst the latter dominates the pull-out mechanisms for large fibre inclination. Inclined fibres can enhance the ultimate strength and cracking resistance of a composite, and postpone its rupture due to the increase in peak load and pull-out work.

- The study with different pull-out specimens reveals the important phe-

nomenon that different methods of applying the pull-out load will cause different pull-out responses. The problem has been ignored by experimental researchers. Therefore specimens with initially straight fibres should be used with caution. Although the pull-out specimens with initially straight fibres can reasonably represent the practical engineering case, it is difficult to load the fibres exactly at the fibre exit. Specimens with initially bent fibres are recommended as reasonable substitute for experimental studies.

- From the study of pull-out with multiple fibres it is concluded that for the fibre volume fraction commonly adopted in engineering the effect of fibre spacing on pull-out can be ignored. In experimental research, specimens with a single fibre can be used to assess the average pull-out behaviour of a composite with a similar inclined angle fibre. The entire response of a composite can be then obtained through probabilistic and statistical analyses of the results from various single fibre researches.

- The prospect of applying the developed model to curved bar reinforced concrete has been demonstrated. Adopting reasonable contact constraints can overcome the complexity in simulating large sliding and separation caused by bar curvature. The analyses indicate that the increase of bar curvature can raise greatly the pull-out resistance. The efficiency is more obvious for bars with 30^o to 60^o curvatures.

9.2 Suggestions for Further Work

The work presented in this thesis provides an important means for studying pull-out behaviour of SFRCC and bar reinforced concrete, and an important basis for further development of the damage concrete model. Based on

the present research, further development and consolidation of the work are suggested as follows:

- Based on damage model IV, a more powerful biaxial damage model can be developed to include inelastic residual deformation and crack closure effect under reverse cyclic loading. This can be completed though adding a plastic term and crack closure function into the potential equation.

- Complex reinforcement geometry can cause serious damage to the matrix in the vicinity of the interface, and severe distortion in corresponding elements. This will influence the proper working of the initial contact pairs, resulting in convergence problems. To overcome this, an interfacial damage model might offer a promising alternative. Moreover, to reasonably describe cyclic pull-out response, an interfacial damage model is also necessary since the definition of unloading stiffness in the present analysis is not very satisfactory. The development of the concrete damage models lay the foundation for developing an interfacial damage model. The main difference in the latter would be to design a damage criterion based on shear failure.

- The separation length at a fibre exit point needs to be more accurately defined. To reliably estimate its magnitude and variation during pull-out, a strength or fracture criteria may be needed.

- In order to use the pull-out method to carry out three dimensional finite element modelling, much work needs to be done. The increase in modelling complexity and meshing would be considerable, especially for defining contact pairs etc. Perhaps an interfacial damage model would have some potential in this respect as well.

- Based on the developed pull-out method, further study of FRCC can be carried out, including the effect of fibre strength, interaction among triple fibres and the pull-out behaviour of different fibre geometries, such as hooked, crimped and paddled fibres etc. During the investigation of the latter, some new pull-out mechanisms might be brought into play, which will also promote further development of the present model.

References

[1] P. Soroushian and Z. Bayasi. Fibre-type effects on the performance of steel fibre reinforced concrete. *ACI Materials Journal*, 88(2):129–134, 1991.

[2] A. E. Naaman and H. W. Reinhardt. *High performance fiber reinforced cement composite 2 (HPFRCC2).* E & FN SPON, London, 1995.

[3] V. S. Gopalaratnam and S. P. Shah. Tensile failure of steel fiber-reinforced mortar. *Journal of Engineering Mechanics*, 113(5):635–652, 1987.

[4] G. G. Nammur and A. E. Naaman. Bond stress model for fibre reinforced concrete based on bond stress-slip relationship. *ACI Materials Journal*, 86(1):45–57, 1989.

[5] I. D. Karsan and J. O. Jirsa. Behaviour of concrete under compressive loadings. *J. Struct. Div., ASCE*, 95(12):2535–2563, 1969.

[6] J. Mazars and G. Pijaudier-Cabot. Continuum damage theory – application to concrete. *Journal of Engineering Mechanics , ASCE*, 115(2):345–365, 1989.

[7] W. F. Chen and Saleeb A. F. *Constitutive Equations for Engineering*

Materials Volume 1: Elasticity and Modelling. John Wiley & Sons, New York, 1982.

[8] J. Lee and G. L. Fenves. Plastic-damage model for cyclic loading of concrete structure. *Journal of Engineering Mechanics*, 124(8):892–900, 1998.

[9] V. S. Gopalaratnam and S. P. Shah. Softening response of plain concrete in direct tension. *ACI,J.*, 82(3):310–323, 1985.

[10] H. Kupfer, H. K. Hilsdorf, and H. Rusch. Behaviour of concrete under biaxial stresses. *ACI,J.*, 66(8):656–666, 1969.

[11] K.Y. Leung and N. Shapiro. Optimal steel fiber strength for reinforcement of cementitious materials. *Journal of Materials in Civil Engineering*, 11(2):116–123, 1999.

[12] C. Ouyang, A. Pacios, and S. P. Shah. Pullout of inclined fibers from cementitious matrix. *Journal of Engineering Mechanics*, 120(12):2641–2659, 1994.

[13] A.E. Naaman and S.P. Shah. Pull-out mechanism in steel fiber-reinforced concrete. *Journal of the Structure Division*, August:1537–1548, 1976.

[14] D. V. Phillips, D. R. Green, B. Zhang, and R. H. Scott. Bond behaviour in curve bars under monotonic & cyclic loading. Department of Civil Engineering Research Report, No. CE-ST95-54, Glasgow University, 1995.

[15] J. M. Alwan and A. E. Naaman. New formulation for elastic mod-

ulus of fibre-reinforced, quasibrittle matrices. *Journal of Engineering Mechanics*, 120(11):2443–2460, 1994.

[16] A. E. Naaman, G. G. Namur, J. M. Alwan, and H. S. NAJM. Fiber pull-out and bond slip. I: Analytical study. *J. Struc. Engrg.*, 117(9):2769–2790, 1991.

[17] A. Jarzebowski. On the modeling of fibre pull-out forced in composites. In *Brittle matrix composites 1 (edited by A.M. Brandt and I.H. Marshall)*, Nov 12-15, pages 371–381, Jablonna, Poland, 1985.

[18] V. C. Li, Y. Wang, and S. Backer. Effect of inclining angle, bundling, and surface treatment on synthetic fiber pull-out from a cement matrix. *Comp.*, 21(2):132–140, 1990.

[19] A. Katz and V.C. Li. Inclination angle effect of carbon fibers in cementitious composites. *Journal of Engineering Mechanics*, 121(12):1340–1348, 1995.

[20] M. Maalej, V. C. Li, and T. Hashida. Effect of fiber rupture on tensile properties of short fiber composites. *Journal of Engineering Mechanics*, 121(8):903–913, 1995.

[21] Y. P. Geng and K. Y. Leung. Damage-based modelling of fibre pullout under variable compressive stress. *Journal of Engineering Mechanics*, 123(4):342–349, 1997.

[22] J. Kullaa. Analysis of elastic fibre bridging in the multiple crack composite. *Journal of Materials Science*, 31:61–70, 1996.

[23] J. Kullaa. Micromechanics of multiple cracking, Part I: Fibre analysis. *Journal of Materials Science*, 33:4213–4224, 1998.

[24] J. Kullaa. Micromechanics of multiple cracking, Part II: Statistical tensile behaviour. *Journal of Materials Science*, 33:4225–4234, 1998.

[25] P. Baros. Analysis of pull-out tests on fibers embedded in brittle matrices. *J. Materials Sci.*, 15:3122–3128, 1980.

[26] J. Bowling and G. W. Groves. The debonding and pull-out of ductile wire from a brittle matrix. *J. Materials Sci.*, 14:431–442, 1979.

[27] R. J. Gray. Analysis of the effect of embedded fibre length on fiber debonding and pull-out from an elastic matrix, part I: Review of theories. *J. Mat. Sci.*, 19:861–870, 1984.

[28] R. J. Gray. Analysis of the effect of embedded fibre length on fiber debonding and pull-out from an elastic matrix, part II: Application to a steel fibre-cementitious matrix composite system. *J. Materials Sci.*, 19:1680–1691, 1984.

[29] Y. Wang, S. Backer, and V. C. Li. A special technique for determination of the critical length of fibre pull-out from a cement matrix. *J. Mater. Sci. Lett.*, 7:842–844, 1988.

[30] V. C. Li and Y. W. Chan. Determination of interfacial debond mode for fibre-reinforced cementitious composites. *J. Engrg. Mech. Div. ASCE*, 120(4):707–719, 1994.

[31] V. C. Li. Postcrack scaling relations for fibre reinforced cementitious composites. *ASCE Journal of Materials in Civil Engineering*, 4(1):41–57, 1992.

[32] C. K. Y. Leung and V. C. Li. Effect of fibre inclination on crack

bridging stress in brittle fibre reinforced brittle matrix composites. *J. Mech. Phys. Solids*, 40(6):1333–1362, 1992.

[33] V. C. Li. The effect of snubbing friction on the first crack strength of flexible fiber reinforced composites. In *Proceedings of the 8th European Congress of Fracture: Fracture Behaviour and Design of Materials and Struct.*, pages 738–745. European Group of Fracture II, 1990.

[34] T. P. Tassios and P. J. Yannopoulos. Analytical studies on reinforced concrete members under cyclic loading based on bond stress-slip relationships. *ACI Journal , Proceedings*, 78(3):206–216, 1981.

[35] J. N. Kar and A. K. Pal. Strength of fiber reinforced concrete. *ASCE Proceedings*, 98(ST5):1053–1068, 1972.

[36] R. N. Swamy and P. S. Mangat. A theory for the flexural strength of steel fibre reinforced concrete. *Cement and Concrete Research*, 4(2):313–325, 1974.

[37] S. Somayali and S. P. Shah. Bond stress versus slip relationships and cracking response of tension members. *J. ACI*, 78(3):217–225, 1981.

[38] L. B. Greszczuk. Theoretical studies of the mechanics of fibre-matrix interface in composites. *ASTM ATP 452*, pages 42–58, 1968.

[39] P. Lawrence. Some theoretical considerations of fiber pullout from an elastic matrix. *J. Materials Sci.*, 7:1–6, 1972.

[40] V. Laws, A. A. Langley, and J. M. West. The glass fibre/cement bond. *J. Materials Sci.*, 21:289–296, 1986.

[41] Y. J. Wang, V. C. Li, and S. Backer. Analysis of synthetic fiber pull-out from a cement matrix. In *Bonding in Cementitious Composites*, volume 114, pages 159–165, Pittsburgh, Pa. , 1987.

[42] V. S. Gopalaratnam and J. Cheng. On the modeling of inelastic interfaces in fibrous composites. In *Symp. Proc.*, volume 114, pages 225–231, Pittsburgh, Pa. , 1987.

[43] H. Stang, Z. Li, and S. P. Shah. Pullout problem: Stress versus fracture mechanical approach. *J. Engrg. Mech.*, 116(10):2136–2150, 1990.

[44] A. E. Naaman, G. G. Namur, J. M. Alwan, and H. S. Najm. Fiber pull-out and bond slip. II: Experimental validation. *J. Struc. Engrg.*, 117(9):2791–2800, 1991.

[45] A. M. Brandt. On the optimal direction of short metal fibres in brittle matrix composites. *Journal of Materials Science*, 20(3):3831–3841, 1985.

[46] C. K. Y. Leung and J. Chi. Crack-bridging force in random ductile fiber brittle matrix composites. *J. Engrg. Mech. ASCE*, 121(12):1315–1324, 1995.

[47] G. A. Kardomateas and R. L. Carlson. A micromechanical model for the fiber bridging of macro-cracks in composite plates. *Journal of Applied Mechanics*, 63:225–233, 1996.

[48] J. Aveston, R. A. Mercer, and J. M. Sillwood. Fiber reinforced cements - scientific foundations for specifications. In *Proc. Nat. Phys. Lab. Conf. on Composites, Standards Testing and Design*, pages 93–103, Surrey, England, 1974.

[49] J. Morton and G. W. Groves. The cracking of composites consisting of discontinuous ductile fibres in a brittle matrix — effect of fibre orientation. *J. Mat. Sci.*, 9:1436–1445, 1974.

[50] J. Aveston, G. A. Cooper, and A. Kelly. Single and multiple fracture. In *The properties of fiber reinforced fiber composites*, pages 15–26, Guilford, England, 1971.

[51] V. C. Li and C. K. Y. Leung. Theory of steady state and multiple cracking of random discontinuous fiber reinforced brittle matrix composites. *ASCE J. of Engineering Mechanics*, 118(11):2246–2264, 1992.

[52] V. C. Li and H. C. Wu. Conditions for pseudo strain-hardening in fiber reinforced brittle matrix composites. *Journal of Applied Mechanics Review*, 45(8):390–398, 1992.

[53] D. B. Marshall, B. N. Cox, and A. G. Evans. The mechanics of matrix cracking in brittle matrix fiber composites. *Acta Metall.*, 33(11):2013–2021, 1985.

[54] C. Gurney and J. Hunt. Quasi-static crack propagation. In *Proc. Royal Soc.,A299*, pages 508–524, London, England, 1967.

[55] C. Atkinson, J. Avila, E. Betz, and R. E. Smelser. The rod pull-out problem, theory and experiment. *J. Mech. Phys. Solids*, 30(3):97–120, 1982.

[56] H. Stang and S. P. Shah. Fracture mechanics interpretation of the fibre/matrix debonding process in cementitious composites. In *Int. Conf. Fracture Mech. Concr.*, pages 339–349, Amsterdam, Netherlands, 1985.

[57] H. Stang and S. P. Shah. Failure of fibre reinforced composites by pull-out fracture. *J. Materials Sci.*, 21:953–957, 1986.

[58] S. Wei, J. A. Mandel, and S. Said. Study of the interface strength in steel fibre-reinforced cement-based composites. *ACI Journal*, 83(4):597–605, 1986.

[59] Y. C. Gao. Debonding along the interface of composites. *Mech. Res. Communications*, 14(2):67–72, 1987.

[60] B. Budiansky, J. W. Hutchinson, and A. G. Evans. Matrix fracture in fiber-reinforced ceramics. *J. Mech. Phys. Solids*, 34(2):167–189, 1986.

[61] J. A. Mandel, S. Wei, and S. Said. Studies of the properties of the fiber-matrix interface in steel fiber reinforced mortar. *ACI Materials Journal*, March-April(6):101–109, 1987.

[62] J. K. Morrison, S. P. Shah, and Y. S. Jenq. Analysis of fibre debonding and pullout in composites. *Journal of Engineering Mechanics*, 114(2):277–294, 1988.

[63] L. M. Zhou, J. K. Kim, and Y. W. Mai. Interfacial debonding and fibre pull-out stresses. *Journal of Material Science*, 27:3155–3166, 1992.

[64] C. K. Y. Leung. A fracture-based two-way debonding model for discontinuous fibers in an elastic matrix. *J. Engrg. Mech. , ASCE*, 118(11):2298–2318, 1992.

[65] B. Mobasher and C. Y. Li. Modelling of stiffness degradation of the interfacial zone during fiber debonding. *Composites Engineering*, 5(10-11):1349–1365, 1995.

[66] S. A. Hamoush and M. R. Salami. Interface strain energy release rate of fiber reinforced concrete based on bond stress-slip relationship. *ACI Structure Journal*, 87(6):678–686, 1990.

[67] Y. C. Gao, Y. W. May, and B. Cotterell. Fracture of fibre reinforced materials. *J. Applied Mechanics and Physics ZAMP*, 39:550–572, 1988.

[68] S. Sumitro and T. Tsubaki. Microfractural pullout model of steel fiber reinforced concrete. In *Fracture Mechanics of Concrete Structures (Edited by Mihashi H. and Rokugo K.)*, volume 1, pages 521–530, D-79104 Freiburg, German, 1998.

[69] D. Ngo and A. C. Scordelis. Finite element analysis of reinforced concrete beams. *ACI Journal*, pages 152–163, 1967.

[70] Schäfer. A contribution to the solution of contact problems with the aid of bond elements. In *Computer methods in applied mechanics and engineering*, volume 6, pages 335–354, Amsterdam, 1975.

[71] A.K. de Groot, G. M. A. Kusters, and T. Monnier. Numerical modeling of bond-slip behaviour. *Heron*, 26(1B), 1981.

[72] D. Z. Yankelevsky. New finite element for bond-slip analysis. *Journal of Structural Engineering*, 111(7):1533–1543, 1985.

[73] M. Keuser and G. Mehlhorn. Finite element models for bond problems. *Journal of Structure Engineering*, 113(10):2160–2173, 1987.

[74] A. S. Ezeldin and P. N. Balaguru. Characterization of bond between fiber, concrete and reinforcing bars using nonlinear finite element analysis. *Computers & Structures*, 37(4):569–584, 1990.

[75] J. Bolander Jr, M. Satake, and H. Hikosaka. Bond degradation near developing cracks in reinforced concrete structures. *Memoirs of the faculty of engineering, Kyushu University*, 52(4):379–395, 1992.

[76] R. J. Allwood and A. A. Bajarwan. Modeling nonlinear bond-slip behaviour for finite element analysis of reinforced concrete structures. *ACI Structure Journal*, 93(5):538–544, 1996.

[77] T. Tsubaki and S. Sumitro. Numerical simulation model for mechanical behaviour of fiber reinforced concrete. In *Fracture Mechanics of Concrete Structures (Edited by Mihashi H. and Rokugo K.)*, volume 1, pages 531–540, D-79104 Freiburg, Germany, 1998.

[78] C. Y. Li and B. Mobasher. Finite element simulations of fiber pull-out toughening in fiber reinforced cement based composites. *Advanced cement based materials*, 7(3-4):123–132, 1998.

[79] C. La Borderie, J. Mazars, and G. Pijaudier-Cabot. Response of plain and reinforced concrete structures under cyclic loadings. *ACI SIP 134*, pages 147–172, 1992.

[80] X.Y. Tao and D.V. Phillips. Numerical modeling of fibre pull-out in fibre reinforced concrete. In *Computational Mechanics in UK*, pages 33–36. ACME, 1998.

[81] X.Y. Tao and Phillips. The effect of inclinations of steel fibre on cement based composites behaviour, (submitted). *Journal of Engineering Mechanics*, 1999.

[82] A. Francavilla and O. C. Zienkiewicz. A note on numerical computation of elastic contact problem. *International Journal for Numerical methods in Engineering*, 9:913–924, 1975.

[83] T. J. R. Hughes, R. L. Taylor, J. L. Sackman, A. Curnier, and W. Kanoknukulchai. A finite element method for a class of contact-impact problems. *Comp. Methods Appl. Mech. Eng.*, 8:249–276, 1976.

[84] T. A. Laursen and J. C. Simo. On the formulation and numerical treatment of finite deformation contact problems. In *Computational Methods in Nonlinear Mechanics (Edited by P. Wriggers and W. Wagner)*, pages 716–7361, Springer-Verlag, Berlin, 1991.

[85] T. A. Laursen and J. C. Simo. A continuum-based finite element formulation for the implicit solution of multibody, large deformation frictional contact problems. *International Journal for Numerical Methods in Engineering*, 36:3451–3485, 1993.

[86] J. J. Kalker. Aspects of contact mechanics. In *Proceedings of the symposium of IUTAM 1974: the mechanics of the contact between deformable bodies (Edited by A.D. de Pater and J.J. Kalker)*, Delft University Press, 1974.

[87] J. T. Oden and J. A. C. Martins. Models and computational methods for dynamic frictional phenomena. *Comp. Methods Appl. Mech. Eng.*, 52:527–634, 1985.

[88] Z. H. Zhong and J. Mackerle. Static contact problems - A review. *Engineering Computations*, 9:3–37, 1992.

[89] M. A. Crisfield. *Non-linear finite element analysis of solids and structures, Volume 2: Advanced Topics.* John Wiley & Sons, Chichester, England, 1997.

[90] J. E. Mottershead, S. K. Pascoe, and R. G. English. A general finite

element approach for contact stress analysis. *International Journal for Numerical Methods in Engineering*, 33:765–779, 1992.

[91] R. Michalowski and Z. Mroz. Associated and non-associated sliding rules in contact friction problems. *Arch. Mech.*, 39:259–276, 1978.

[92] J. T. Oden and G. F. Carey. *Finite elements - Special problem in solid mechanics, Volume V.* Prentic-Hall, Inc., Englewood Clifs, New Jersey 07632, 1984.

[93] P. Wriggers, J. C. Simo, and R. L. Taylor. Penalty and augmented Lagrangian formulations for contact problems. In *Proc. NUMETA'85 Conf.*, pages 97–106, Swansea, 1985.

[94] A. Curnier and P. Alart. Generalisation of Newton type methods to contact problems with friction. *Journal de Mécanique Théorique et appliquée*, 7:67–82, 1988.

[95] D. Peric and D. R. J. Owen. Computational model for 3-D contact problems with friction based on the penalty method. *Int. J. for Num. Mech. in Engng.*, 35:1289–1309, 1992.

[96] P. Papadopoulos and R. L. Taylor. A mixed formulation for the finite element solution of contact problems. *Comp. Mech. in Appl. Mech. & Engng.*, 94:373–389, 1992.

[97] J. O. Hallquist, G. L. Goudreau, and D. Benson. Sliding interfaces with contact-impact in large-scale Lagrangian computations. *Comp. Mech. in Appl. Mech. & Engng.*, 51:107–137, 1985.

[98] A. B. Chaudaray and K. J. Bathe. A solution method for static and

dynamic analysis of contact problems with friction. *Comp. & Struct.*, 724:855–873, 1986.

[99] F. J. Gallego and J. J. Anza. A mixed finite element for the elastic contact problem. *Int. J. for Num. Mech. in Engng.*, 28:1249–1264, 1989.

[100] J. C. Simo and T. A. Laursen. An augmented Lagrangian treatment of contact problems involving friction. *Computers & Structures*, 42(1):97–116, 1992.

[101] T. A. Laursen and J. C. Simo. Algorithmic symmetrization of Coulomb frictional problems using augmented Lagrangians. *Comp. Mech. in Appl. Mech. & Engng.*, 108:133–146, 1993.

[102] J. H. Heegard and A. Curnier. An augmented Lagrangian formulation for discrete large slip contact problems. *Int. J. for Num. Mech. in Engng.*, 36:569–593, 1993.

[103] A. Heege, P. Alart, and E. Onate. Numerical modelling and simulation of frictional contact using a generalised Coulomb law. *Engineering Computations*, 12:641–656, 1995.

[104] F. M. Guerra and R. V. Browning. Comparison of two slideline methods using ADINA. *Comp. Struct.*, 17:819–834, 1983.

[105] M. A. Crisfield. A review of contact and friction in finite element analysis. Technical Report NAFEMS, R0022, 1994.

[106] M. R. Hestenes. Multiplier and gradient methods. *J. Optimiz. Theory Applic.*, 4:303–320, 1969.

[107] M. J. D. Powell. A method for nonlinear constraints in minimisation problems. In *Optimization (Edited by R. Fletcher)*, New York, 1969. Academic Press.

[108] W. F. Chen. *Constitutive Equations for Engineering Materials Volume 2: Plasticity and Modelling.* Elsevir Science B.V., The Netherlands, 1994.

[109] L. M. Kachanov. On the creep fracture time. *Izv. AN SSR, Otd. Tekhn. Nauk*, 8:26–31 (in Russian), 1958.

[110] J. Lubliner. On the thermodynamic foundations of non-linear solid mechanics. *Int. J. Non-Linear Mechanics*, 7:237–254, 1972.

[111] D. Krajcinovic and G. U. Fonseka. The continuous damage theory of brittle materials. part I: General theory. *Journal of Applied Mechanics, ASCE*, 48:809–815, 1981.

[112] M. Ortiz. A constitutive theory for the inelastic behavior of concrete. *Mech. Mat.*, 4(1):67–93, 1985.

[113] C.L. Chow and J. Wang. An anisotropic theory of elasticity for continuum damage mechanics. *Int. J. Frac*, 33:3–16, 1987.

[114] J. Mazars. Application de la mécanique de l'endommangement au comportement non linéaire et à la rupture du béton de structure. Technical report, L.M.T., Université Paris, France, 1984.

[115] P. Ladevèze. Sur une théorie de l'endommangement anisotrope. Technical report, L.M.T., Cachan, France, 1983.

[116] J. Mazars. A model of a unilateral elastic damageable material and its application to concrete. In *Proc. RILEM Int. Conf. Fracture Mechanics of Concrete*, pages 61–71, Lausanne, Switzerland, 1986.

[117] F. Collombet. Modélisation de l'endommangement anisotrope. application au comportement du béton sous sollicitations multiaxiales. Technical report, L.M.T., Université Paris, France, 1985.

[118] G. Pijaudier-Cabot. Caractérisation et modélisation du comportement du béton par un essai multiaxial automatique. Technical report, L.M.T., Université Paris, France, 1985.

[119] S. Yazdani and H.L. Schreyer. An anisotropic damage model with dilatation for concrete. *Mechanics of Materials*, 7:231–244, 1988.

[120] S. Fichant, G. Pijaudier-Cabot, and C. La Borderie. Continuum damage modelling with crack induced anisotropy. In *Proc. of Complas 4 (Edited by D.R.J.Owen)*, volume 1, pages 1045–1056, Pineridge Press, 1995.

[121] G. Baker and R. de Borst. A thermo-mechanical damage model for concrete at elevated temperatures. In *Proceedings FRAMCOS-2, (edited by Folker H. Wittmann)*, pages 991–1000, London, 1995.

[122] G. Baker and J. Stabler. Computational modeling of thermally induced fracture in concrete. In *Computational Modeling of Concrete Structures EURO-C, (edited by R. de Borst, N.Bicanić, H.Mang and G. Meschke)*, pages 467–480, A.A.Balkema: Potterdam, 1998.

[123] S. P. Shah and Y. S. Jenq. Fracture mechanics of interfaces. In *Symp. Proc*, volume 114, pages 205–216. Materials Research Society, 1987.

[124] J. W. Ju. On energy-based coupled elastoplastic damage theory: Constitutive modelling and computational aspects. *Int. J. Solids Structures.*, 25(7):803–833, 1989.

[125] J. Lubliner, J. Oliver, S. Oller, and E. Oñate. A plastic-damage model for concrete. *Int. J. Solids Structures*, 25(3):299–326, 1989.

[126] S. Oller, E. Oñate, J. Oliver, and J. Lubliner. Finite element nonlinear analysis of concrete structure using a plastic-damage model. *Engineering Fracture Mechanics*, 35(1/2/3):219–231, 1990.

[127] G. Z. Voyiadjis and P. I. Kattan. A plasticity-damage theory for large deformation of solids – I. theoretical formulation. *Int. J. Engrg. Sci.*, 30(9):1089–1108, 1992.

[128] B. Luccioni, S. Oller, and R. Danesi. Coupled plastic-damaged model. *Computer Methods in Applied Mechanics and Engineering*, 129:81–89, 1996.

[129] G. Pijaudier-Cabot and Bažant Z.P. Nonlocal damage theory. *Journal of Engineering Mechanics*, 113(10):1512–1533, 1988.

[130] G. Pijaudier-Cabot, J. Mazars, and J. Pulikowski. Steel-concrete bond analysis with nonlocal continuous damage. *Journal of structural engineering*, 117(3):863–882, 1991.

[131] J. Lubliner. *Plasticity Theory.* MacMillan, New York, 1990.

[132] E. Hinton, R. Wood, N. Bićanić, P. White, and T. Hellen. *NAFEMS Introduction to Nonlinear finite Element Analysis (Edited by Hinton, E.).* NAFEMS Birniehill East Kilbride, Glasgow, 1992.

[133] G. Pijaudier-Cabot. Damage based models. In *Summer Course on Mechanics of Concrete*, volume 1 of *23-27 September*, pages 1–66, Poland, 1996.

[134] J. Mazars. Damage models and modelling strategies for concrete structures under severe loadings. In *fracture Mechanics of Concrete Structures (Edited by Z.P.Bažant)*, pages 260–268, England, 1992.

[135] Karlsson Hibbitt and Sorensen. *ABAQUS: Theory Manual, Vers. 5.6.* Hibbitt, Karlsson and Sorensen Inc., 1996.

[136] C. K. Y. Leung and N. Ybanez. Pullout of inclining flexible fiber in cementitious composite. *J. Engrg. Mech. ASCE*, 123(3):239–246, 1997.

[137] S. Hota and A.E. Naaman. Bond stress-slip response of reinforcing bars embedded in FRC matrices under monotonic and cyclic loading. *ACI Structural Journal*, 94(5):525–537, 1997.

[138] G. Monti, F. C. Filippou, and E. Spacone. Finite element for anchored bars under cyclic load reversals. *Journal of Structural Engineering ASCE*, 123(5):614–623, 1997.

[139] H. G. Kwak. Improved numerical approach for the bond-slip behavior under cyclic loads. *Structural Engineering and Mechanics*, 5(5):663–667, 1997.

[140] X.Y. Tao, D.V. Phillips, and N. Bićanić. Application of damage mechanics to concrete subjected to cyclic or biaxial loading. In *Computational Mechanics in UK*, 2000.

Principal Value of Deviatoric Strain

The strain tensor ϵ_{ij} can be decomposed into two parts, a spherical component associated with a change in volume, and a deviatoric component associated with the change in shape. That is

$$\epsilon_{ij} = e_{ij} + \frac{1}{3}\epsilon_{kk}\delta_{ij}, \tag{.1}$$

where e_{ij} is a deviatoric strain tensor.

In order to derive the principal value of the deviatoric strain tensor, we need to solve for the following determinantal equation.

$$|e_{ij} - e\delta_{ij}| = 0. \tag{.2}$$

The expansion of Eq. .2 leads to a characteristic equation

$$e^3 - J_1'e^2 - J_2'e - J_3' = 0 \tag{.3}$$

where J_i' $(i = 1, 2, 3)$ are deviatoric strain invariants and

$$J_1' = e_{ii} = 0 \tag{.4}$$

$$J_2' = \frac{1}{2}e_{ij}e_{ij} \tag{.5}$$

$$J_3' = \frac{1}{3} e_{ij} e_{jk} e_{ki} \tag{.6}$$

Since $J_1' = 0$, Eq..3 becomes

$$e^3 - J_2' e - J_3' = 0. \tag{.7}$$

Taking $e = r \sin\theta$, the above equation becomes

$$\sin\theta^3 - \frac{J_2'}{r^2} \sin\theta - \frac{J_3'}{r^3} = 0. \tag{.8}$$

Comparing Eq..8 with the trigonometric identity (Eq..9),

$$\sin\theta^3 - \frac{3}{4} \sin\theta + \frac{1}{4} \sin 3\theta = 0, \tag{.9}$$

we obtain

$$r = \sqrt{\frac{4}{3} J_2'} = \frac{2\sqrt{J_2'}}{\sqrt{3}} \tag{.10}$$

$$\sin 3\theta = -\frac{4J_3'}{r^3} = -\frac{3\sqrt{3}J_3'}{2(J_2')^{\frac{3}{2}}} \tag{.11}$$

$$\theta = \frac{1}{3} \arcsin\left(-\frac{3\sqrt{3}}{2} \frac{J_3'}{(J_2')^{\frac{3}{2}}}\right) \tag{.12}$$

There are three roots of Eq..8 for $-\pi/6 \leq \theta \leq \pi/6$. The three principal values of the deviatoric strain tensor e_{ij} are

$$\begin{bmatrix} e_1 \\ e_2 \\ e_3 \end{bmatrix} = \frac{2\sqrt{J_2'}}{\sqrt{3}} \begin{bmatrix} \sin(\theta + \frac{2\pi}{3}) \\ \sin(\theta) \\ \sin(\theta + \frac{4\pi}{3}) \end{bmatrix} \tag{.13}$$

with $e_1 > e_2 > e_3$.

Derivative of Principal/Deviatoric-Principal Strain and Invariants

$$\begin{aligned}\frac{\partial \epsilon_q}{\partial \epsilon_{ij}} &= \frac{\partial}{\partial \epsilon_{ij}}(e_q + \frac{\epsilon_{rr}}{3} I_q) \\ &= \frac{\partial e_q}{\partial \epsilon_{ij}} + \frac{I_q \delta ij}{3}\end{aligned} \tag{.14}$$

$$\begin{aligned}\frac{\partial^2 \epsilon_q}{\partial \epsilon_{ij} \partial \epsilon_{kl}} &= \frac{\partial}{\partial \epsilon_{kl}}(\frac{\partial e_q}{\partial \epsilon_{ij}} + \frac{\delta_{ij} I_q}{3}) \\ &= \frac{\partial^2 e_q}{\partial \epsilon_{ij} \partial \epsilon_{kl}}\end{aligned} \tag{.15}$$

$$\begin{aligned}\frac{\partial e_q}{\partial \epsilon_{ij}} &= \frac{\partial}{\partial \epsilon_{ij}}(\frac{2\sqrt{J_2'}}{\sqrt{3}} \begin{bmatrix} \sin(\theta + \frac{2\pi}{3}) \\ \sin\theta \\ \sin(\theta + \frac{4\pi}{3}) \end{bmatrix}) \\ &= \frac{\partial}{\partial \epsilon_{ij}}(\frac{2\sqrt{J_2'}}{\sqrt{3}} \sin\Theta_q) \\ &= \frac{2\sqrt{J_2'}}{\sqrt{3}} \frac{\partial \theta}{\partial \epsilon_{ij}} \cos\Theta_q + \frac{1}{\sqrt{3J_2'}} \frac{\partial J_2'}{\partial \epsilon_{ij}} \sin\Theta_q\end{aligned} \tag{.16}$$

$$\frac{\partial^2 e_q}{\partial \epsilon_{ij} \partial \epsilon_{kl}} = \frac{\partial}{\partial \epsilon_{kl}}(\frac{2\sqrt{J_2'}}{\sqrt{3}} \frac{\partial \theta}{\partial \epsilon_{ij}} \cos\Theta_q + \frac{1}{\sqrt{3J_2'}} \frac{\partial J_2'}{\partial \epsilon_{ij}} \sin\Theta_q)$$

$$
\begin{aligned}
&= \frac{2\sqrt{J_2'}}{\sqrt{3}}\frac{\partial^2\theta}{\partial\epsilon_{ij}\partial\epsilon_{kl}}\cos\Theta_q - \frac{2\sqrt{J_2'}}{\sqrt{3}}\frac{\partial\theta}{\partial\epsilon_{ij}}\frac{\partial\theta}{\partial\epsilon_{kl}}\sin\Theta_q + \\
&+ \frac{1}{\sqrt{3J_2'}}\frac{\partial J_2'}{\partial\epsilon_{kl}}\frac{\partial\theta}{\partial\epsilon_{kl}}\cos\Theta_q + \frac{1}{\sqrt{3J_2'}}\frac{\partial^2 J_2'}{\partial\epsilon_{ij}\partial\epsilon_{kl}}\sin\Theta_q + \\
&+ \frac{1}{\sqrt{3J_2'}}\frac{\partial J_2'}{\partial\epsilon_{ij}}\frac{\partial\theta}{\partial\epsilon_{kl}}\cos\Theta_q - \frac{1}{2\sqrt{3}(J_2')^{\frac{3}{2}}}\frac{\partial J_2'}{\partial\epsilon_{ij}}\frac{\partial J_2'}{\partial\epsilon_{kl}}\sin\Theta_q \\
&= \frac{\sqrt{J_2'}}{\sqrt{3}}(2\frac{\partial^2\theta}{\partial\epsilon_{ij}\partial\epsilon_{kl}} + \frac{1}{J_2'}\frac{\partial\theta}{\partial\epsilon_{ij}}\frac{\partial J_2'}{\partial\epsilon_{kl}} + \frac{1}{J_2'}\frac{\partial J_2'}{\partial\epsilon_{ij}}\frac{\partial\theta}{\partial\epsilon_{kl}})\cos\Theta_q + \\
&+ \frac{\sqrt{J_2'}}{\sqrt{3}}(\frac{1}{J_2'}\frac{\partial^2 J_2'}{\partial\epsilon_{ij}\partial\epsilon_{kl}} - 2\frac{\partial\theta}{\partial\epsilon_{ij}}\frac{\partial\theta}{\partial\epsilon_{kl}} - \\
&- \frac{1}{2(J_2')^2}\frac{\partial J_2'}{\partial\epsilon_{ij}}\frac{\partial J_2'}{\partial\epsilon_{kl}})\sin\Theta_q
\end{aligned}
\tag{.17}
$$

$$
\begin{aligned}
\frac{\partial\theta}{\partial\epsilon_{ij}} &= \frac{1}{3}\frac{\partial}{\partial\epsilon_{ij}}[\arcsin(-\frac{3\sqrt{3}}{2}\frac{J_3'}{(J_2')^{\frac{3}{2}}})] \\
&= \frac{1}{3\sqrt{1-\sin^2 3\theta}}[-\frac{3\sqrt{3}}{2}(-\frac{3}{2}\frac{J_3'}{(J_2')^{\frac{5}{2}}}\frac{\partial J_2'}{\partial\epsilon_{ij}} + \frac{1}{(J_2')^{\frac{3}{2}}}\frac{\partial J_3'}{\partial\epsilon_{ij}})] \\
&= \frac{\sqrt{3}}{2\cos 3\theta(J_2')^{\frac{3}{2}}}(\frac{3}{2}\frac{J_3'}{J_2'}\frac{\partial J_2'}{\partial\epsilon_{ij}} - \frac{\partial J_3'}{\partial\epsilon_{ij}})
\end{aligned}
\tag{.18}
$$

$$
\begin{aligned}
\frac{\partial^2\theta}{\partial\epsilon_{ij}\partial\epsilon_{kl}} &= \frac{\partial}{\partial\epsilon_{kl}}[\frac{\sqrt{3}}{2\cos 3\theta(J_2')^{\frac{3}{2}}}(\frac{3}{2}\frac{J_3'}{J_2'}\frac{\partial J_2'}{\partial\epsilon_{ij}} - \frac{\partial J_3'}{\partial\epsilon_{ij}})] \\
&= \frac{\sqrt{3}}{2}[\frac{3\sin 3\theta}{\cos^2 3\theta(J_2')^{\frac{3}{2}}}\frac{\partial\theta}{\partial\epsilon_{kl}} - \frac{3}{2}\frac{1}{\cos 3\theta(J_2')^{\frac{5}{2}}}\frac{\partial J_2'}{\partial\epsilon_{kl}}(\frac{3}{2}\frac{J_3'}{J_2'}\frac{\partial J_2'}{\partial\epsilon_{ij}} - \frac{\partial J_3'}{\partial\epsilon_{ij}}) + \\
&+ \frac{1}{\cos 3\theta(J_2')^{\frac{3}{2}}}(\frac{3}{2}\frac{J_3'}{J_2'}\frac{\partial^2 J_2'}{\partial\epsilon_{ij}\partial\epsilon_{kl}} + \frac{3}{2J_2'}\frac{\partial J_2'}{\partial\epsilon_{ij}}\frac{\partial J_3'}{\partial\epsilon_{kl}} - \\
&- \frac{3}{2}\frac{J_3'}{(J_2')^2}\frac{\partial J_2'}{\partial\epsilon_{ij}}\frac{\partial J_2'}{\partial\epsilon_{kl}} - \frac{\partial^2 J_3'}{\partial\epsilon_{ij}\partial\epsilon_{kl}})] \\
&= \frac{3\sqrt{3}\sin 3\theta}{2\cos^2 3\theta(J_2')^{\frac{3}{2}}}(\frac{3}{2}\frac{J_3'}{J_2'}\frac{\partial J_2'}{\partial\epsilon_{ij}} - \frac{\partial J_3'}{\partial\epsilon_{ij}})\frac{\partial\theta}{\partial\epsilon_{kl}} + \\
&+ \frac{3\sqrt{3}}{4\cos 3\theta(J_2')^{\frac{3}{2}}}(\frac{1}{J_2'}\frac{\partial J_2'}{\partial\epsilon_{kl}}\frac{\partial J_3'}{\partial\epsilon_{ij}} - \frac{3}{2}\frac{J_3'}{(J_2')^2}\frac{\partial J_2'}{\partial\epsilon_{ij}}\frac{\partial J_2'}{\partial\epsilon_{kl}} + \\
&+ \frac{J_3'}{J_2'}\frac{\partial^2 J_2'}{\partial\epsilon_{ij}\partial\epsilon_{kl}} + \frac{1}{J_2'}\frac{\partial J_2'}{\partial\epsilon_{ij}}\frac{\partial J_3'}{\partial\epsilon_{kl}} - \frac{J_3'}{(J_2')^2}\frac{\partial J_2'}{\partial\epsilon_{ij}}\frac{\partial J_2'}{\partial\epsilon_{kl}} - \frac{2}{3}\frac{\partial^2 J_3'}{\partial\epsilon_{ij}\partial\epsilon_{kl}})
\end{aligned}
$$

$$= \frac{3\sin 3\theta}{\cos 3\theta}\frac{\partial\theta}{\partial\epsilon_{ij}}\frac{\partial\theta}{\partial\epsilon_{kl}} + \frac{3\sqrt{3}}{4\cos 3\theta (J_2')^{\frac{5}{2}}}(J_3'\frac{\partial^2 J_2'}{\partial\epsilon_{ij}\partial\epsilon_{kl}} - \frac{2J_2'}{3}\frac{\partial^2 J_3'}{\partial\epsilon_{ij}\partial\epsilon_{kl}} -$$
$$- \frac{5}{2}\frac{J_3'}{J_2'}\frac{\partial J_2'}{\partial\epsilon_{ij}}\frac{\partial J_2'}{\partial\epsilon_{kl}} + \frac{\partial J_2'}{\partial\epsilon_{kl}}\frac{\partial J_3'}{\partial\epsilon_{ij}} + \frac{\partial J_2'}{\partial\epsilon_{ij}}\frac{\partial J_3'}{\partial\epsilon kl}) \qquad (.19)$$

$$\begin{aligned}\frac{\partial J_2'}{\partial\epsilon_{ij}} &= \frac{\partial}{\partial\epsilon_{ij}}(\frac{1}{2}e_{st}e_{st}) \\ &= e_{st}\frac{\partial e_{st}}{\partial\epsilon_{ij}} \\ &= e_{st}\frac{\partial}{\partial\epsilon_{ij}}(\epsilon_{st} - \frac{\epsilon_{rr}}{3}\delta_{st}) \\ &= e_{st}(\delta_{si}\delta_{tj} - \frac{\delta_{ij}\delta_{st}}{3}) \\ &= e_{ij} - \frac{\delta_{ij}e_{ss}}{3} \\ &= e_{ij}\end{aligned} \qquad (.20)$$

$$\begin{aligned}\frac{\partial^2 J_2'}{\partial\epsilon_{ij}\partial\epsilon_{kl}} &= \frac{\partial e_{ij}}{\partial\epsilon_{kl}} \\ &= \delta_{ik}\delta_{jl} - \frac{\delta_{ij}\delta_{kl}}{3}\end{aligned} \qquad (.21)$$

$$\begin{aligned}\frac{\partial J_3'}{\partial\epsilon_{ij}} &= \frac{\partial}{\partial\epsilon_{ij}}(\frac{1}{3}e_{rs}e_{st}e_{tr}) \\ &= \frac{1}{3}[e_{rs}e_{st}(\delta_{ti}\delta_{rj} - \frac{\delta_{ij}\delta_{tr}}{3}) + e_{rs}e_{tr}(\delta_{si}\delta_{tj} - \\ &\quad - \frac{\delta_{ij}\delta_{st}}{3}) + e_{st}e_{tr}(\delta_{ri}\delta sj - \frac{\delta_{ij}\delta rs}{3})] \\ &= \frac{1}{3}[e_{is}e_{sj} - \frac{e_{rs}^2}{3}\delta_{ij} + e_{ir}e_{rj} - \frac{e_{rs}^2\delta_{ij}}{3} + e_{it}e_{tj} - \frac{e_{tr}^2\delta_{ij}}{3}] \\ &= e_{is}e_{sj} - \frac{e_{rs}^2\delta_{ij}}{3} \\ &= e_{is}e_{sj} - \frac{2J_2'}{3}\delta_{ij}\end{aligned} \qquad (.22)$$

$$\frac{\partial^2 J_3'}{\partial\epsilon_{ij}\partial\epsilon_{kl}} = \frac{\partial}{\partial\epsilon_{kl}}(e_{is}e_{sj} - \frac{2J_2'}{3}\delta_{ij})$$

$$
\begin{aligned}
&= e_{is}\frac{\partial e_{sj}}{\partial \epsilon_{kl}} + e_{sj}\frac{\partial e_{is}}{\partial \epsilon_{kl}} - \frac{2\delta_{ij}}{3}\frac{\partial J_2'}{\partial \epsilon_{kl}} \\
&= e_{is}(\delta_{sk}\delta_{jl} - \frac{\delta_{sj}\delta_{kl}}{3}) + e_{sj}(\delta_{ik}\delta_{sl} - \frac{\delta_{is}\delta_{kl}}{3}) - \\
&\quad - \frac{2}{3}\delta_{ij}e_{kl} \\
&= e_{ik}\delta_{jl} - \frac{e_{ij}\delta_{kl}}{3} + e_{jl}\delta_{ik} - \frac{e_{ij}\delta_{kl}}{3} - \frac{2}{3}\delta_{ij}e_{kl} \\
&= e_{ik}\delta_{jl} + e_{jl}\delta_{ik} - \frac{2}{3}(e_{ij}\delta_{kl} + e_{kl}\delta_{ij}) \qquad (.23)
\end{aligned}
$$